Magnetic coupling of the solar photosphere and chromosphere

DISSERTATION

zur

Erlangung des Doktorgrades

der

Fakultät für Mathematik und Physik

der

Albert Ludwigs Universität Freiburg

vorgelegt von

Reza Rezaei

aus

Sari, Iran

Oktober 2008

Dissertation zur Erlangung des Doktorgrades
der Fakultät für Mathematik und Physik
der Albert-Ludwigs-Universität Freiburg im Breisgau

Dekan:	Prof. Dr. K. Königsmann
Betreuer:	PD Dr. W. Schmidt
Referent:	Prof. Dr. A. Blumen
Korreferent:	Prof. Dr. H. Helm
Datum der mündlichen Prüfung:	Oktober 08, 2008

Reza Rezaei
Kiepenheuer–Institut für Sonnenphysik (KIS), Schöneckstr. 6, 79104 Freiburg, Germany

In the context of this thesis the following articles have been published:

Refereed Journals

- "Reversal-free Ca II H profiles: a challenge for solar chromosphere modeling in quiet inter-network", R. Rezaei, J.H.M.J. Bruls, W. Schmidt, C. Beck, , W. Kalkofen, and R. Schlichenmaier 2008, **Astronomy & Astrophysics** 484, pp. 503–509

- "The horizontal internetwork magnetic field: numerical simulations in comparison to observations with Hinode", O. Steiner, R. Rezaei, W. Schaffenberger, and S. Wedemeyer-Böhm 2008, **Astrophysical Journal Letters**, 680, pp. L85-L88

- "The signature of chromospheric heating in Ca II H spectra", C. Beck, W. Schmidt, R. Rezaei, and W. Rammacher 2007, **Astronomy & Astrophysics** 479, pp. 213–227

- "Hinode observations reveal boundary layers of magnetic elements in the solar photosphere", R. Rezaei, O. Steiner, S. Wedemeyer-Böhm, R. Schlichenmaier, W. Schmidt, and B.W. Lites 2007, **Astronomy & Astrophysics Letters** 476, pp. L33–L36

- "Opposite magnetic polarity of two photospheric lines in single spectrum of the quiet Sun", R. Rezaei, R. Schlichenmaier, W. Schmidt, and O. Steiner 2007, **Astronomy & Astrophysics Letters** 469, pp. L9–L12

- "Relation between photospheric magnetic field and chromospheric emission", R. Rezaei, R. Schlichenmaier, C. Beck, J.H.M.J. Bruls, and W. Schmidt 2007, **Astronomy & Astrophysics** 466, pp. 1131–1144

- "The flow field in the sunspot canopy", R. Rezaei, R. Schlichenmaier, C. Beck, and L.R. Bellot Rubio 2006, **Astronomy & Astrophysics** 454, pp. 975–982

Conference Proceedings

- "Single lobe Stokes-V profiles in the solar atmosphere", R. Rezaei, W. Schmidt, and R. Schlichenmaier, DPG meeting, 3-7 March 2008, Freiburg

- "Variation of the Stokes-V area asymmetry across magnetic elements", R. Rezaei, O. Steiner, S. Wedemeyer-Böhm, R. Schlichenmaier, and B.W. Lites 2007, AN 328, Issue 7, p. 706

- "Temporal evolution of magnetic elements", R. Rezaei, R. Schlichenmaier, W. Schmidt and C. Beck, in Solar Polarization Workshop (SPW5) 2007, Eds. S. Berdyugina, K.N. Nagendra, and R. Ramelli, ASPC, in press (Arxiv:0712.0234)

♣ "Freeware solutions for spectropolarimetric data reduction", F. Paletou, R. Rezaei, and L. Léger, in Solar Polarization Workshop (SPW5) 2007, Eds. S. Berdyugina, K.N. Nagendra, and R. Ramelli, ASPC, in press (Arxiv:0712.1522)

♣ "Photospheric magnetic field and chromospheric emission", R. Rezaei, R. Schlichenmaier, C. Beck, and W. Schmidt, in "Modern Solar Facilities: Advanced Solar Sciences", Eds. F. Kneer, K.G. Puschmann, A.D. Wittmann, Sep. 2006, pp. 169–173

Abstract

The solar surface outside sunspots and active regions, i.e., the quiet Sun, shows the ubiquitous pattern of granulation in the photosphere. The quiet solar photosphere harbors small-scale magnetic structures inside and between granules. This thesis presents thermodynamic properties of the small-scale magnetic flux concentrations in the quiet Sun using high spatial and temporal resolution observations along with numerical simulations. Spectral line profiles of the Fe I 630 nm pair and Ca II H were used to trace the photospheric and chromospheric layers of the magnetic elements.

In the presence of magnetic field spectral lines split and are polarized via the Zeeman effect. The difference of a spectral line profile, measured in left and right circular polarized light, is a Stokes-V profile with two lobes. In the absence of any gradients of velocity or magnetic field along the line of sight, Stokes-V profiles are anti-symmetric. The different area of the two lobes, the Stokes-V area asymmetry, provides information about the gradients of the magnetic and velocity fields along the line of sight. Comparing high resolution spectropolarimetric data with synthetic maps of a 3D MHD simulation, we found several magnetic elements in the photosphere showing a central region of negative Stokes-V area asymmetry surrounded by a peripheral region with larger positive asymmetry. This finding was the first observational confirmation of the existence of a sharp boundary layer between magnetic elements and their immediate surroundings. Such boundary layers had been theoretically predicted ten years ago. Furthermore, we found for the first time two Stokes-V profiles of the Fe I 630 nm line pair in a single spectrum showing opposite magnetic polarities. These two lines form in slightly different layers, so they trace the magnetic field in different geometrical heights. The temporal evolution of these profiles showed a magnetic flux cancellation, suggesting a magnetic reconnection in the photosphere. A 1D numerical model that reproduced the observed profiles was interpreted as an indication for the magnetic reconnection. To verify the existence of vigorous gradients in the magnetic and thermal properties of the atmosphere as suggested by the cancellation event, extreme cases of asymmetry in Stokes-V profiles, i.e., profiles with only one lobe instead of two, were found in a large sample of data. We find strong evidence for concentrated magnetic flux structures with sharp boundaries sustaining a strong gradient or a discontinuity in thermodynamic parameters. In other words, we find current sheets in boundary layers which separate magnetic from non-magnetic plasma. This supports the existence of structured magnetic entities like flux tubes.

The second part of this thesis was devoted to study the thermal structure of the chromosphere and its relation to underlying photospheric magnetic flux concentrations. The Ca II H line is one of the strongest absorption lines in the visible solar spectrum. Generally, there are two emission peaks (H_{2V} and H_{2R}) on either side of the line core which form in the chromosphere. The existence of the emission peaks implies a temperature rise in the chromosphere. Parts of the line outside these two emission peaks mainly form in the photosphere. The integrated intensity in a 0.1 nm band around the core which contains the two emission peaks is a measure for the chromospheric emission. The minimum chromospheric emission is as large as half of the average emission. We found that the

chromospheric emission in excess to the minimum emission scales with the magnetic flux density. To establish a relation between the chromospheric emission and temperature, we looked for the Ca II H line profiles without any emission peak at H_{2V} and H_{2R} wavelengths. A quarter of the observed calcium profiles did not show any emission peak. A comparison of these profiles with synthesized calcium profiles of one-dimensional time-independent models provides strong indication for chromospheric temperatures cooler than that of the spatially and temporally averaged quiet Sun. Our results suggest that a large fraction of the solar chromosphere consists of hot plasma, $T \gtrsim 10\,000\,\mathrm{K}$. Beside this, there is a smaller fraction which is cooler than the underlying photosphere, $T \lesssim 5\,000\,\mathrm{K}$, but cannot be much cooler than, e.g., 2000 K.

Zusammenfassung

Die Sonnenoberfläche weist außerhalb von Sonnenflecken und aktiven Regionen das allgegenwärtige Muster der Granulation auf. Die ruhige Photosphäre beherbergt kleine magnetische Strukturen zwischen und innerhalb von Granulen. Diese Doktorarbeit präsentiert die thermodynamischen Eigenschaften dieser kleinen magnetischen Fluss konzentrationen der ruhigen Sonne anhand von Beobachtungen mit hoher räumlicher und zeitlicher Auflösung und mit Hilfe numerischer Simulationen.

Dazu wurden Spektren eine Absorptionslinienpaares bei 630 nm und von Ca II H verwendet, um die magnetischen Elemente sowohl in der Photosphäre als auch in der Chromosphäre untersuchen zu können. In Gegenwart eines Magnetfeldes sind die Spektrallinien durch den Zeeman-Effekt aufgespalten und polarisiert. Die Differenz der Spektrallinienprofile von links- und rechtszirkular polarisiertem Licht ergibt ein sogenanntes Stokes-V-Profil mit zwei Scheitelpunkten. Die Stokes-V-Profile sind antisymmetrisch, solange es keine Geschwindigkeits- oder Magnetfeldgradienten entlang der Sichtlinie gibt. Die gemessene Stokes-V-Asymmetrie ist ein Indikator für die Gradienten der magnetischen Felder und der Geschwindigkeiten entlang der Sichtlinie. Bei unserer Untersuchung fanden wir mehrere magnetische Elemente in der Photosphäre mit einer negativen Stokes-V-Asymmetrie, umgeben von einem Randgebiet mit größerer positiver Asymmetrie. Dazu wurden hochaufgelöste Spektropolarimetriedaten mit synthetischen Karten einer 3D-MHD-Simulation verglichen.

Diese Entdeckung ist die erste experimentelle Bestätigung der Existenz einer scharfen Grenzschicht zwischen den magnetischen Elementen und ihrer direkten Umgebung, die bereits zehn Jahre zuvor von der Theorie vorhergesagt wurde. Außerdem wurden zum ersten Mal zwei Stokes-V-Profile des Fe I 630 nm-Linienpaares gefunden, die unterschiedliche magnetische Polaritäten innerhalb eines Spektrums aufweisen. Die beiden Linien entstehen in unterschiedlichen Schichten und lassen daher Aussagen über magnetische Polaritäten in verschiedenen Höhen zu. Eine Untersuchung der zeitlichen Entwicklung dieser Profile förderte eine Auslöschung des magnetischen Flusses zutage, ein starker Hinweis auf magnetische Rekonnektion in der Photosphäre. Ein eindimensionales numerisches Modell konnte unter Berücksichtigung dieses Effektes die beobachteten Profile reproduzieren, was die Annahme der magnetischen Rekonnektion weiter untermauert. Um die Existenz starker magnetischer und thermaler Gradienten in der Atmosphäre zu verifizieren, wurden Profile mit extrem ausgeprägter Asymmetrie untersucht, beispielsweise Profile mit nur einem statt zwei Scheitelpunkten. Wir fanden dabei überzeugende Anhaltspunkte für konzentrierte magnetische Flussstrukturen mit scharfen Grenzen, die einen starken Gradienten oder eine Diskontinuität der thermodynamischen Parameter aufweisen. Mit anderen Worten: Es wurden Stromschichten entdeckt, die magnetisches Plasma von nicht-magnetischem trennen.

Der zweite Teil dieser Doktorarbeit widmet sich der thermischen Struktur der Chromosphäre und ihrer Beziehung zu magnetischen Flusskonzentrationen in der darunterliegenden Photosphäre. Dabei fand die Ca II H-Spektrallinie Verwendung, die eine der stärksten Absorptionslinien im sichtbaren Spektrum der Sonne darstellt. Sie weist im Normalfall

zwei Emissionspeaks zu beiden Seiten des Linienkerns auf, die beide in der Chromosphäre entstehen. Die außerhalb dieser Emissionspeaks liegenden Teile des Spektrums stammen hauptsächlich aus der Photosphäre. Die Gesamtintensität in einem Intervall von 0,1 nm um den Linienkern ist daher ein Maß für die Emission der Chromosphäre. Die minimale chromosphärische Emission beträgt etwa die Hälfte der durchschnittlichen Emission. Wir fanden heraus, dass die über diesem Minimalwert liegende chromosphärische Emission proportional zur magnetischen Flussdichte ist. Um eine Beziehung zwischen der Temperatur und der chromosphärischen Emission herzustellen, untersuchten wir Ca II H-Profile ohne jeglichen Emissionspeak, was in etwa für ein Viertel der Profile der Fall war. Ein Vergleich mit synthetischen Calcium-Profilen aus eindimensionalen und zeitunabhängigen Simulationen ergab, dass die chromosphärischen Temperaturen unterhalb derer der zeitlich und räumlich gemittelten ruhigen Sonne liegen. Unsere Ergebnisse legen nahe, dass ein großer Anteil der solaren Chromosphäre aus heißem Plasma besteht ($T \gtrsim 10\,000\,\mathrm{K}$). Daneben gibt es Bereiche, die kühler sind ($T \lesssim 5\,000\,\mathrm{K}$) als die darunterliegende Photosphäre, jedoch keinesfalls im Bereich von 2000 K.

Acknowledgement

Working as a PhD student at the Kiepenheuer–Institut für Sonnenphysik was a magnificent as well as challenging experience to me. In all these years, many people were instrumental directly or indirectly in shaping up my academic career. It was hardly possible for me to thrive in my doctoral work without the precious support of these personalities. Here is a small tribute to all those people.

First of all, I wish to thank my supervisors, Dr. Wolfgang Schmidt and Dr. Rolf Schlichenmaier, for introducing me to the realm of high-resolution spectropolarimetry. It was only due to their valuable guidance, cheerful enthusiasm and ever-friendly nature that I was able to complete my research work in a respectable manner.

I wish to express gratitude to Deutsche Forschungsgemeinschaft (DFG) for providing the financial support for this work. I would also like to convey my deep regards to the director of the KIS, Prof. O. von der Lühe, for facilitating financial support in the first year of the work.

My special thanks to Dr. Jo Bruls for performing NLTE radiative transfer calculations. I also take this opportunity to express my special gratitude towards Dr. Oskar Steiner for helping me out in all aspects during my work on the COBOLD numerical simulations.

On the observational side, I have learnt everything from Dr. Rolf Schlichenmaier and Dr. Christian Beck. I have to appreciate their patient during our observing campaigns.

I express thanks to Dr. Thomas Kentischer, Dr. Peter Caligari, Michael Weissschädel, Oliver Wiloth, and Thomas Keller for providing technical support during the observing campaigns at the VTT.

I am privileged for having Dr. Christian Beck, Christian Bethge, Sven Bingert, Dirk Schmidt, and Hans-Peter Doerr as my colleges who have provided great company during all those years at the KIS. Especially, the assistance of Dirk Schmidt and Christian Bethge in setting up Linux prorams 24 hours a day & seven days a week provided me a solid support for all the computer problems I could ever face. The German language summary of this thesis is also the outcome of Christian Bethge's efforts. Numerous IDL routines from Dr. Christian Beck accelerated my progress significantly.

I am thankful to Dr. Jo Bruls and Dr. Christian Beck who read parts of thesis and provided helpful comments. I have used also the amazing opportunity to work with Dr. Luis Bellot Rubio (IAA, Granada, Spain) and discuss a variety of issues concerning the SIR code.

I thank Dr. Frederic Paletou (LATT, Toulouse, France) who introduced the concepts of spectropolarimetry and Python programing to me.

My interest in astronomy was initiated in elementary school and led me to study physics. I have worked with Prof. Mansouri and Prof. Samimi at Sharif University of Technology during my bachelor studies. Prof. Sobouti, Dr. Jahan Miri and Dr. Khajeh Pour kindly supported me during my master program. My motivation in astronomy increased drastically during BSc and MSc such that I finally decided to do a PhD in this field. I have to express my special thanks to my firends at the astronomy group of the Sharif University of Technology.

I wish to thank my parents for their constant support and encouragement in all my professional endeavors. Finally, I wish to express my gratitude to my wife Souri for her love, and patience. I was not only abroad, far from my parents, but also far from my wife. Without their encouragement and understanding it would have been impossible for me to finish this work. For this, I dedicate this thesis to my own Sun, Souri.

Reza Rezaei, October 2008

Contents

List of Tables

List of Figures

Chapter 1

Introduction

Historical background: Among billions of stars in our galaxy, the Sun is the closest one. This is why from dawn of history, it was an important celestial object among heavens. There is evidence of historic records of the solar observations, especially from solar eclipses, as early as 2000 BC (Guillermier & Koutchmy 1999). With the invention of the telescope, details of the solar surface (e.g., large sunspots) were revealed. Soon after that, scientists detected a periodicity in the number of sunspots: the solar cycle. Fraunhofer used spectroscopic techniques and found absorption lines in the solar spectrum in 1815. By the mid of the nineteenth century, photographic techniques assisted astronomers in recording the solar activities. Spectroscopy played a major role afterward and led to the discovery of helium. In 1892, George Ellery Hale constructed a spectroheliograph and recorded coronal lines during an eclipse. Hale also discovered the magnetic field of sunspots in 1908. Table 1.1 lists some historic moments in investigating the Sun.

1.1 The solar atmosphere

The solar and stellar structure is approximated by a set of spherical shells. The central part of the solar interior, the *nucleus*, is where nuclear fusion generates the energy flux by converting hydrogen into helium. The nucleus is surrounded by a *radiative interior*, which transmits the energy flux as electromagnetic radiation. The *convective envelope* (convection zone) is a shell in which the opacity is so high that the energy flux is not transmitted as electromagnetic radiation; there, virtually the entire energy flux is carried by convection (Böhm-Vitense 1989). The solar *atmosphere* is defined as the part where photons can escape into interstellar space. It is situated immediately on top of the convection zone. The atmosphere consists of three layers: photosphere, chromosphere, and corona. Different structures are observed at each layer (see Fig. 1.1).

1.1.1 The photosphere

The photosphere is the layer from which the bulk of the electromagnetic radiation escapes from the Sun. It is the deepest layer in the solar atmosphere that is visible in contin-

Table 1.1: Milestones in solar physics.

year	finding	who	reference
1223 BC	the oldest eclipse record	the Babylonians	Zirker (1995)
250 BC	the distance to the Sun	Aristarchus	Hirschfeld (2001)
1543	the Sun moves to center stage	Nicholas Copernicus	Gingerich (1993)
1610	observations of sunspots	Galileo Galilei	Drake (1978)
1687	the solar mass	Isaac Newton	Wilson (1989)
1817	solar spectroscopy	Joseph von Fraunhofer	Meadows (1970)
1838	the solar constant	Claude Pouillet	Young (1897)
1843	the sunspot cycle	Samuel H. Schwabe	Stix (2004)
1908	magnetic nature of sunspots	George Ellery Hale	Hale (1908)
1953	the magnetograph	Karl Otto Kiepenheuer	Kiepenheuer (1953)

uum windows. It is optically thin in visible, UV, and near-IR continua, but optically thick in spectral lines (Stix 2004). It spans only about 0.1 % of the solar radius with a thickness of about 500 km (see Fig. 1.2). Since the temperature decreases outward in this layer, the visible spectrum of the Sun which primarily emerges from the photosphere is an *absorption-line spectrum*. When we observe at the frequency of a spectral line, the higher optical depth causes us to look less deeply into the object than at neighboring frequencies (Shu 1981). Thus, at a resonance frequency, we see less hot layers than in the continuum, leading to dark spectral lines superimposed on a brighter continuum (Fig. 1.3). Applied to the continuum, the same type of reasoning explains the phenomena of *limb-darkening* (Fig. 1.4). When we look at the solar limb, we see less hot layers than we do when we look toward the center. Limb-darkening is a wavelength-dependent phenomenon (Pierce & Slaughter 1977). As seen in the left panel of Fig. 1.2, the temperature decreases outward up to a temperature minimum and then increases outward. If the solar atmosphere were in radiative equilibrium, i.e., if the energy were carried by electromagnetic radiation alone, the temperature had to decrease outward monotonically (Holweger & Müller 1974). Radiative equilibrium models predict that the temperature decreases steadily with height until it flattens out where the medium becomes optically thin to the bulk of the passing radiation. However, the solar chromosphere and corona have temperatures far above $T_{min} \approx 4200\,K$ found at the top of the photosphere (Bruls & Solanki 1993). Hence, some nonthermal energy flux must heat up the outer solar atmosphere. The chromospheric radiative loss is about $4\,kW\,m^{-2}$, Table 1.2 (Withbroe & Noyes 1977; Vernazza et al. 1981). Note that the nonthermal heating flux required to compensate the radiative loss of the chromosphere and corona is four orders of magnitude smaller than the electromagnetic radiation leaving the photosphere (Table 1.2).

The dominant pattern covering the entire solar surface, except sunspots, is granulation, the top of small-scale overturning convection cells with diameters of 1-2 Mm. Viewing along the local vertical, we observe an upflow in the center of granules and a downflow in intergranular lanes (Fig. 1.1, left panel). Velocities of this flow pattern amount to a few $km\,s^{-1}$. On a larger scale of ~ 20 Mm, *supergranules* are observed which show the same

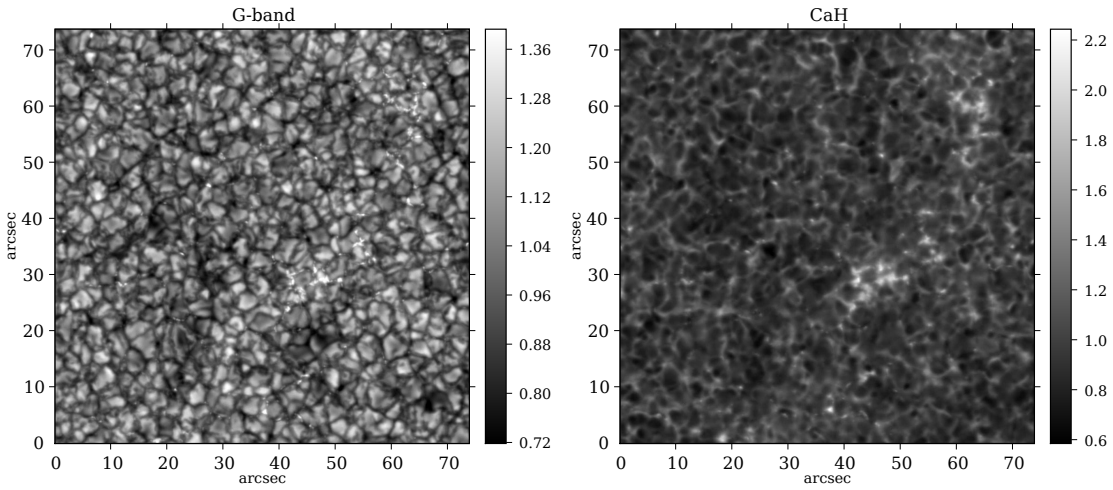

Figure 1.1: These two frames show an identical area on the solar surface observed in the photosphere (left) and chromosphere (right). The left panel is a filtergram in G-band, a collection of CH lines which form in higher photosphere (e.g., Steiner et al. 2001, also see Sect. 1.5), while the right panel is a filtergram in Ca II H whose line center forms in the chromosphere. The bright area in the right panel corresponds to the magnetic network which can be seen with less contrast in the left panel as well. Note the different shape of structures and also different range of variation of intensities, indicated by a grayscale bar at the right. Each map was normalized to its mean value.

pattern as granulation: a horizontal flow from the center towards the boundary of the cell with a typical observed flow speed of $0.5\,\mathrm{km\,s^{-1}}$. These large-scale convection cells have a mean lifetime of 20 h, much longer than the granular time-scale (some 10 minutes). The *chromospheric network* forms at the boundary of the supergranular cells (Fig. 1.1, right panel). The network is presumably formed by the long-time advection of magnetic flux to the boundaries of the supergranules (Priest et al. 2002; Cattaneo et al. 2003). The interior of the network cells, the *inter-network*, has much less magnetic field than the network (e.g., Keller et al. 1994). The magnetic and thermodynamic properties of the network and inter-network are different (e.g., Lites 2002). Additionally, small-scale magnetic structures also exist in the inter-network with dynamic properties different from network, both in simulations and observations (Steiner 2007). A prominent phenomenon near the solar limb are the faculae. Faculae appear close to the solar limb as bright small-scale features that are related to magnetic fields (Keller et al. 2004; Lites et al. 2004). Faculae influences the solar irradiance variation (Fligge & Solanki 2001).

While the granulation is a convective phenomenon, other structures in the photosphere usually have a magnetic nature. Large magnetic structures including sunspots and pores can appear within the activity belts, between $\pm 35^\circ$ latitudes. These large-scale magnetic structures are called active regions. A large active region includes a group of sunspots, pores, and plages, i.e. cluster of faculae. In many young active regions, the two magnetic

Table 1.2: Radiative losses in different layers of the solar atmosphere (Schatzman et al. 1993; Vernazza et al. 1981). Note the important contribution of Ca II and Mg II ions in the chromospheric radiative loss.

domain	energy flux ($\mathrm{W\,m^{-2}}$)
photosphere	6.4×10^7
chromosphere	$2 - 6 \times 10^3$
Balmer series	500
H^-	400
Lyα	300
Metal lines (Ca II, Mg II)	3400
Ca II H	490
Ca II K	640
Ca II 866.2 nm	460
Ca II 849.8 nm	550
Ca II 854.2 nm	680
Mg II h	430
Mg II k	520
transition region	$400 - 600$
corona	600
coronal holes	10

polarities are found in nearly E-W bipolar arrangement (one sunspot follows the other). At the end of each solar cycle, the polarity reversal happens. It changes the polarity of the leading sunspot in active regions, leading to a 22 yr cycle for the magnetic pattern.

1.1.2 The chromosphere

The chromosphere is a structured layer on top of the photosphere. It is optically thin in UV, visible, and near-IR continua, but optically thick in strong spectral lines (Judge & Peter 1998). It is the source of the red crescent around the solar disk at the beginning and end of a total solar eclipse. Chromospheric structures can be seen on the solar disk using monochromatic filters operating in the core of strong lines (Fig. 1.5). In particular, filtergrams recorded in the Balmer line Hα display a lot of structures (Fig. 1.4). The vertical extension of the chromosphere spans a few Mm. Figure 1.1 shows two frames: the left panel shows the dominant photospheric structures, the granulation, along with a few bright points. The pattern on the right panel is a mesh-like structure, far different from the photospheric pattern. This is the chromospheric network, which covers the Sun everywhere outside active regions (Tritschler et al. 2007). The network has mixed magnetic polarity. During the minimum phase of the solar cycle (during which this thesis has been prepared), the magnetic field of the network is the primary magnetic

configuration seen on the solar disk. The areas between the network patches were thought to be free of strong flux concentrations, hence called inter-network. However, recent spectropolarimetric observations by means of Hinode revealed a wealth of mixed polarity magnetic signals in the inter-network (Lites et al. 2008). Comparing the two colorbars in Fig. 1.1, it is evident that the range of intensity variations in the chromospheric pattern is much wider than the photospheric one. There are also dark filaments in the full disk Hα image (Fig. 1.4). Many filaments are found at borders of active regions but there are also filaments outside the activity belts (Zirin 1988). Large filaments are visible outside the solar limb as prominences that are bright against the dark (background) sky (Paletou et al. 2001).

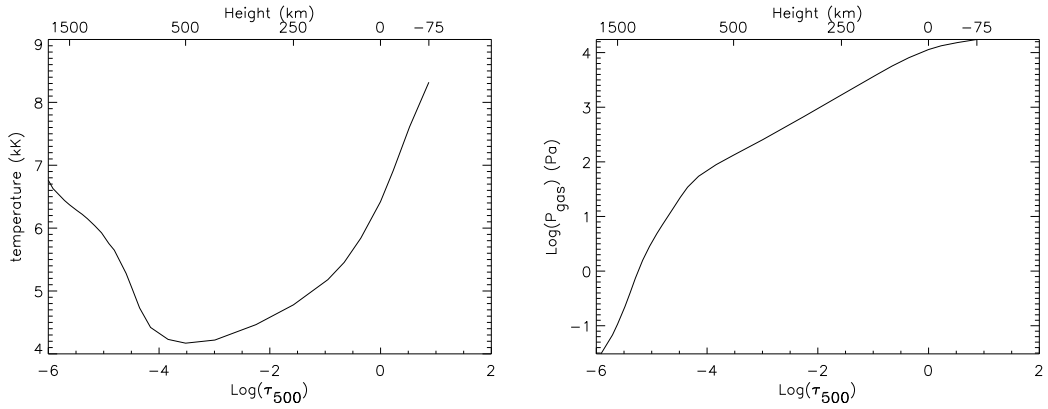

Figure 1.2: Stratification of the temperature (left) and gas pressure (right) in VALC model atmosphere (Vernazza et al. 1981). It shows that going outward from the solar surface, the temperature decreases up to a temperature minimum ($\log \tau \approx -4$). This part is the photosphere. There is a temperature reversal at the temperature minimum, and above it the temperature increases rapidly. The gas pressure decreases exponentially with a scale height of about 150 km.

Cut-off frequency: The turbulent flows in the upper solar convection zone generate waves that travel upward and contribute to the dynamics and heating of the atmosphere. In a homogeneous gas, sound waves of any frequency can propagate without restriction. In a gravitationally and thermally stratified atmosphere (like the solar atmosphere) where the density and pressure decrease exponentially with height, there exists a cut-off frequency that limits propagation of waves with a frequency smaller than that (e.g., Hammer et al. 2007). In the simplest case of purely acoustic waves in a nonmagnetic medium, it has long been known (Lamb 1908, 1911) that a density stratification alone leads already to the existence of a cut-off frequency $\omega_c = \gamma g/2c$, where γ is the ratio of specific heats, g the gravitational acceleration, and c the sound speed. A stratified atmosphere permits propagation of waves with wavelengths small compared to the density scale height. Such waves travel through a nearly homogeneous, slowly varying gas and can thus propagate virtually without restrictions. If the frequency of waves approaches the cut-off frequency,

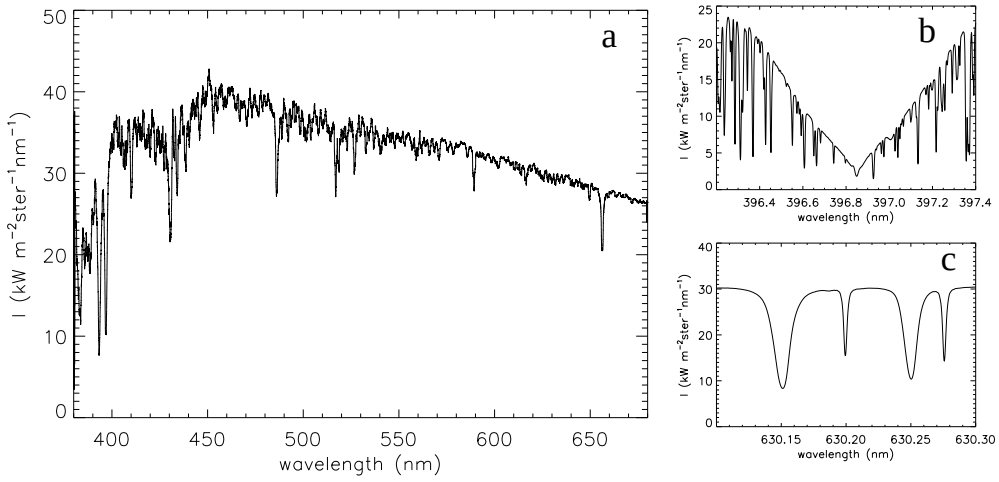

Figure 1.3: *(a)*: The visible solar spectrum expressed in absolute intensity units (Neckel 1999; Kurucz et al. 1984) and spectrally averaged over 1 nm. Strong solar lines like Ca II H & K at about 395 nm and Hα at 656 nm are visible. *(b)*: A small part of the spectrum around the Ca II H spectral line which shows its broad wing. *(c)*: A small part of the spectrum, which shows two neutral iron lines at 630.2±0.05 nm. Note that since the spectrum in (a) was smoothed, the depth of the spectral lines decreased w.r.t. the full resolution spectra in panels (b) and (c).

ω_c, the wavelength becomes so large that the waves see essentially a density jump, which reflects them. In the temperature minimum region of the solar atmosphere, ω_c corresponds to a period of roughly 3 min, so that longer-period waves should not be able to transport energy into the overlying chromosphere and corona. Nevertheless, signatures of waves with longer periods have been observed in the upper atmosphere, for example as oscillations in coronal loops (e.g., De Moortel et al. 2002).

The chromospheric heating mechanism is one of the main challenges of solar physics (Narain & Ulmschneider 1996; Ulmschneider & Musielak 2003, and references therein). The estimates of the total radiative losses from the solar chromosphere (and thus the required heating) are model dependent. The total radiative loss in the chromosphere is calculated from the summation of the radiated energy in strong chromospheric spectral lines (Table 1.2). However, the true amount of the chromospheric radiative losses is not clear. On the one hand, semi-empirical models predict a rate of 2–4 kW m^{-2} (Vernazza et al. 1981). On the other hand, a more recent model that includes all iron blends in the wings of chromospheric lines predicts a value of 14 kW m^{-2} (Anderson & Athay 1989).

There are two categories of mechanisms proposed to be responsible for the chromospheric heating. In the *mechanical heating theory*, the sound waves are the main suspects which transform into shock waves with steep pressure and density gradients in the upper atmosphere (right panel of Fig. 1.2). It is also called the field-free or hydrodynamic

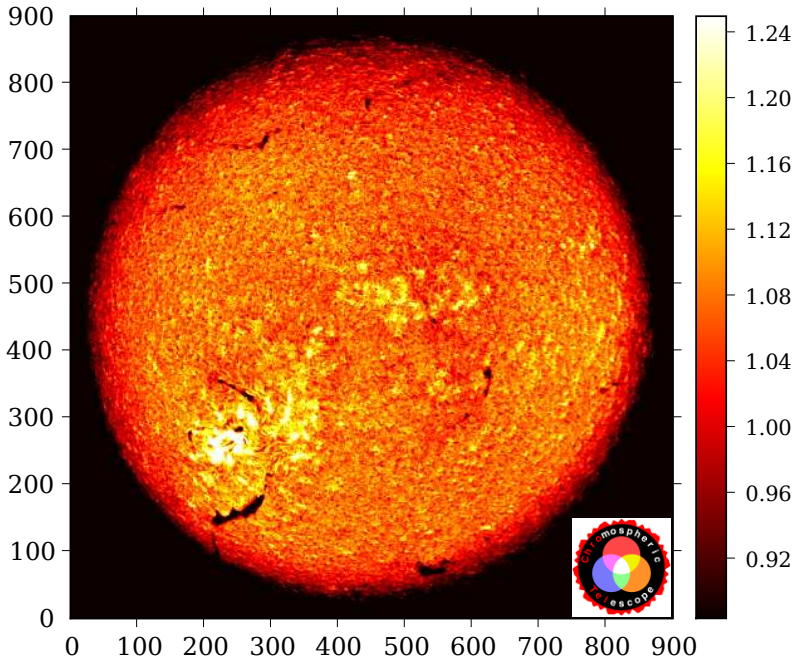

Figure 1.4: Limb-darkening in the solar full-disk image, recorded in Hα line-center with a 0.3 Å filter using the Chromospheric Telescope (ChroTel) of the KIS at Observatorio del Teide on Tenerife. Plage areas seen as bright structures. A small active region is seen in the lower left part of the image. Elongated dark filaments appear to be directed along the magnetic field lines. Tick-marks on both axes indicate arcsec. Courtesy Christian Bethge, KIS.

mechanism. A second class of theory exists in which the magnetic field plays the dominant role. These *magnetic heating theories* can also be divided into two classes: i) direct magnetic heating where a conversion of magnetic energy to kinetic energy happens via Joule heating or magnetic reconnection, and ii) indirect magnetic heating in which the magnetic field lines play the role of a *catalyst* without being destroyed. Carlsson & Stein (1997) presented a semi-empirical hydrodynamic model where enhanced chromospheric emission is due to outward propagating acoustic waves. This model was criticized in subsequent investigations (Carlsson et al. 1997; Kalkofen et al. 1999; Fossum & Carlsson 2005), which was partly due to disagreements on the temperature stratification in higher layers (e.g., Ayres 2002; Wedemeyer-Böhm et al. 2005). In addition, it is not clear whether high- or low-frequency acoustic waves play the dominant role in the energy transport to higher layers (Fawzy et al. 2002a; Jefferies et al. 2006). While there are theoretical indications that the magnetic filling factor discriminates between different regimes of heating (Solanki & Steiner 1990), there is no canonical model reproducing thermal, dynamical and magnetic properties of the solar chromosphere (Judge & Peter 1998; Rutten 1999). Realistic three-dimensional time-dependent simulations including non-local thermodynamic equilibrium (NLTE) radiative transfer are way beyond of present day computer resources (Hammer & Ulmschneider 2007).

Since the plasma density and pressure decrease with a pressure scale height of only ≈150 km, the magnetic flux elements in turn widen their horizontal cross section to keep the pressure balance with the surrounding plasma in the chromosphere (Hammer 1987). Some observations yield evidence for a particularly rapid expansion of the magnetic field in the lower chromosphere leading to the formation of a nearly horizontal field canopy at

a height of roughly 800 km above $\tau = 1$ (Bianda et al. 1999).

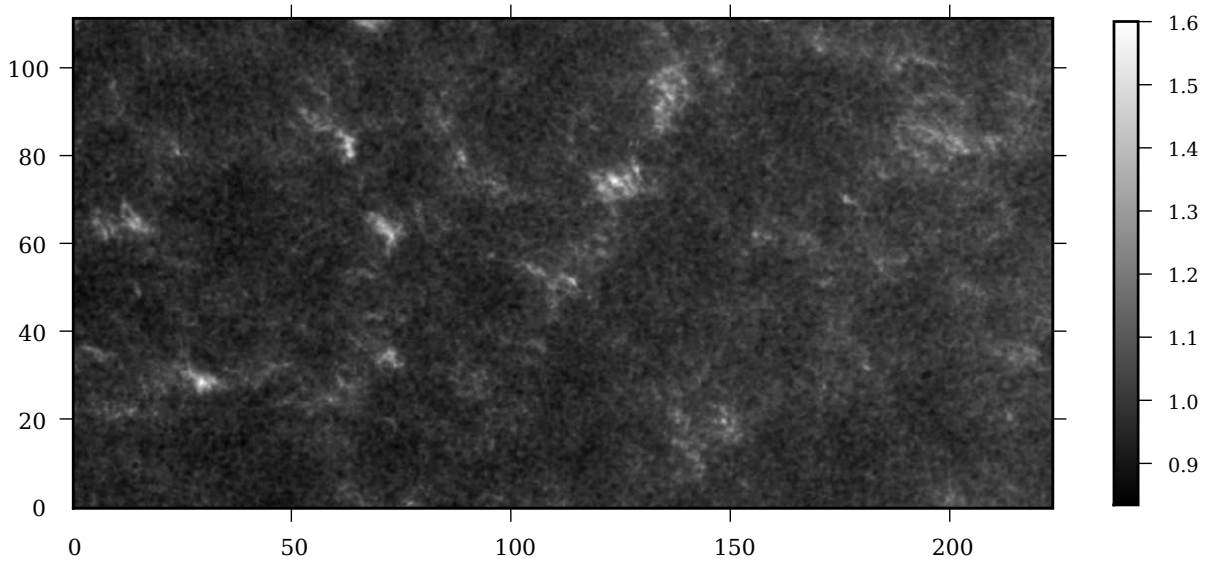

Figure 1.5: Sample of chromospheric network in Ca II H filtergrams. It is an average of a one hour time series of filtergrams. Fine details have been washed out in averaging. The images have been recorded with Hinode on March 10, 2007. Tickmarks show spatial scales in arcsec (1 arcsec $\approx$ 720 km on the Sun).

Ca II resonance lines: Two of the deepest and broadest absorption lines in the visible solar spectrum are the resonance doublet lines of singly-ionized calcium at 393.3 and 396.8 nm. These lines were first observed by Fraunhofer in 1814, designated as K and H lines, respectively (Linsky & Avrett 1970). Similar lines which probe lower chromospheric layers are the Mg II H and K lines at 280.2 and 279.5 nm. In the visible part of the spectrum, Na I D at 589.0 and 589.6 nm, Mg I b at 516.7, 517.2 and 518.3 nm are formed just above the temperature minimum while the core of Hα line at 656.3 nm tends to be formed above the temperature minimum. On the disk, bright features in the core of Ca II H & K lines appear usually in large regions around sunspots and plage regions which form the chromospheric network (Fig. 1.5). First, Hale in 1892 noted the double reversal in the core of the H and K lines. In the umbra and above the limb, they show only a single emission peak. The violet emission feature (H_{2V}) is usually stronger than the corresponding red emission (H_{2R}) and the central absorption feature is usually displaced to the red of the true line center (H_3). Such behavior is typical but occasionally the reverse occurs. Hale & Ellerman (1903) introduced the designations H_3 and K_3 for the central absorption features, H_2 and K_2 for the emission features on either sides of the central absorption, and H_1 and K_1 for the minima in the inner wings beyond the emission. K_1 and K_3 include a contribution of the wing of K_2 and thereby fluctuate in phase with it. The time scale of the intensity

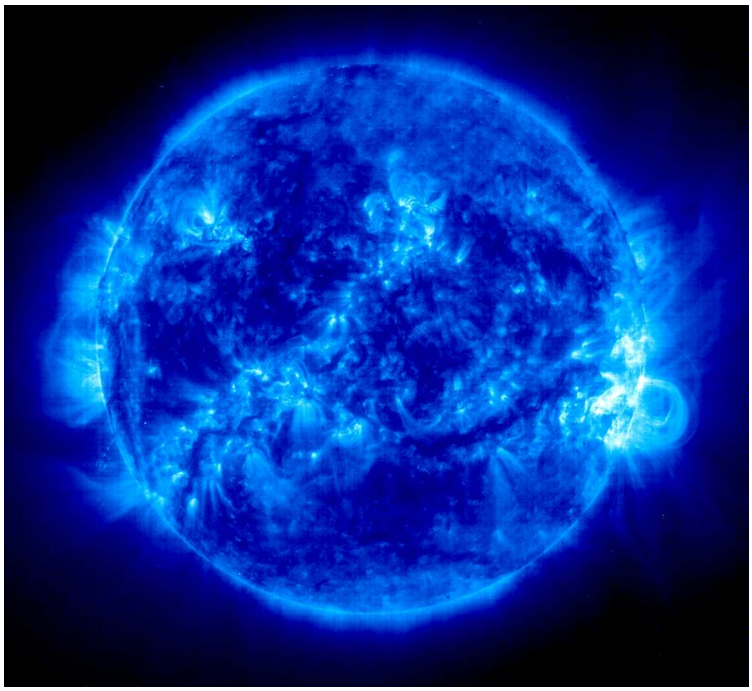

Figure 1.6: The solar corona observed at extreme ultraviolet wavelength on February 22, 2002. A large magnetic loop was recorded by EIT in the Fe IX/X 17.1 nm line. The large loop on the right arches over an active region. The temperature of this material is about 1 million K in the lower corona. The extreme ultraviolet image enables us to see tight, loop-like magnetic fields that extend above the Sun's surface around which charged particles are spinning (Fleck et al. 1995).

fluctuation for the K_2 features is 250 s while it is 170 s for K_3 (Linsky & Avrett 1970). The detailed formation of these two lines is complicated, and its modeling requires the inclusion of NLTE effects and partial frequency redistribution [1], which radiatively couples different wavelengths within the line profile (e.g., Uitenbroek 1989).

The significance of these lines lies in the fact that they are the only resonance lines in the visible solar spectrum from the dominant stage of ionization in the upper photosphere and lower chromosphere of an abundant element. Consequently, the lines are very opaque with a line-center optical depth of 10^7 in the photosphere and 10^4 in the chromosphere. The main components that contribute to these lines are the quiet and active network, bright points, and plages. The strong doublet of H and K lines is one of the standard measures of solar and stellar magnetic activity, because the lines are strong and easily accessible to ground-based observations. A large database of stellar Ca II H+K measurements has been collected at Mt. Wilson observatory (Vaughan et al. 1978; Schrijver et al. 1989). There is evidence of chromospheric and coronal activity on other late-type stars as well. Some of these stars show magnetic activity that is a few order of magnitude stronger than that of the Sun (Schrijver & Zwaan 2000).

1.1.3 The corona

The layer between the chromosphere (10^4 K) and the corona (10^6 K) is called the transition region. The temperature gradient is so large that there is virtually a discontinuity in the

[1] See Sect. 3.1.5.

temperature (and density). The corona is optically very thin in the entire electromagnetic spectrum except at radio wavelengths. It is enormously different from the chromosphere and photosphere (Fig. 1.6) since the density is very low in the corona. The temperature in the corona reaches to $\approx 2{\times}10^6\,\mathrm{K}$, far beyond the underlying temperature of the radiation field. Trivially, it cannot be heated up radiatively which is in apparent contrast to the second law of thermodynamics. Non-radiative processes, either mechanical or magnetic, are responsible for coronal heating (Aschwanden 2004). The corona extends to several solar radii. The radiation of the white-light corona is due to scattering of photospheric photons by free electrons in the corona and interplanetary dust particles. The intensity of the white-light corona is about 10^6 times smaller than the photospheric intensity. Coronal structures in front of the disk can be observed at extreme ultraviolet (EUV) and X-ray wavelengths. The corona is particularly bright in coronal condensations above active regions and is rather dark in coronal holes. They have been identified as close and open magnetic field line structures, respectively. Large coronal holes are observed over the polar caps.

Solar wind: The Sun continually looses mass through the solar wind ($\sim 10^9\,\mathrm{kg\,s^{-1}}$), despite the fact that the coronal plasma is gravitationally bound to the Sun. Since the thermal conductivity is high in the corona, the temperature stays high out to some $10\,\mathrm{R}_\odot$, so the thermal energy exceeds the binding energy. The outer corona therefore evaporates, and matter from below streams up to replace the lost matter (Parker 1958). The solar wind exhibits a quiescent outflow that is frequently interrupted by transient disturbances. It consists of a high-speed flow and a low-speed flow. The high-speed flow, which originates from coronal holes, has velocities of 700–900 $\mathrm{km\,s^{-1}}$ and a particle density of $\sim 3\,\mathrm{cm^{-3}}$. The low-speed flows has a velocity of 300–400 $\mathrm{km\,s^{-1}}$ and a particle density three times higher than the high-speed wind. The magnetic field introduces the possibility of carrying away more angular momentum than associated with the outflowing matter itself, resulting in a magnetic breaking of the Sun's rotation (Weber & Davis 1967).

1.2 Radiative transfer

Model atmosphere: The medium where a part of the solar spectrum formed, is usually specified by a number of physical parameters as a function of geometrical height. This allows one to calculate local values of the optical depth, the propagating matrix (absorption and dispersion profiles, see Sect. 1.3.5), and the source function. In astrophysics, we call a set of such parameters a model atmosphere. A vertically stratified (plan-parallel) atmosphere is a medium whose properties vary along a ray but are constant in planes perpendicular to the ray. A typical model atmosphere contains temperature, gas and electron pressure, the microturbulence velocity, the line-of-sight (LOS) velocity, and the three components of the magnetic field vector. Usually, a macro-turbulence velocity is also considered to account for the bulk motion of matter on scales larger than the mean free path of photons (Mihalas 1978; Rutten 2003).

Solar model atmospheres are built to reproduce the observed intensity spectrum of the Sun in continuum windows and selected lines (e.g., the series of models initiated by Vernazza et al. 1981). These models rely on temporally and spatially averaged spectra. Hence, they provide information about the average properties of the physical parameters in the solar atmosphere (Linsky & Avrett 1970). Examples of model atmospheres for the quiet Sun that have been studied in this thesis are Harvard Smithsonian Reference Atmosphere (HSRA, Gingerich et al. 1971), VAL (Vernazza et al. 1981), and FAL (Fontenla et al. 1993). The temperature and pressure stratification of the VALC model atmosphere in the photosphere and lower chromosphere are shown in Fig. 1.2.

1.2.1 Local thermodynamic equilibrium (LTE)

We have to clarify our assumptions about the thermodynamic state of the solar atmosphere. *Thermodynamic equilibrium* prevails when a single temperature, T, is sufficient to describe the thermodynamic state everywhere. The particles then have the Maxwellian velocity distribution corresponding to that T. The states of ionization and excitation of the atoms are distributed according to the Saha and Boltzmann equations for that same T. And the radiation field has the homogeneous and isotropic black-body form given by the Planck function, for the same T:

$$B_\nu(T) = \frac{2\,h\,\nu^3}{c^2}\frac{1}{\exp(h\,\nu/k\,T)-1} \tag{1.1}$$

No temperature gradient exists in thermodynamic equilibrium, and it is obvious that this situation is realized virtually nowhere. Very often, however, the condition of *local thermodynamic equilibrium (LTE)* is very closely satisfied. That is, at a certain place, a single temperature T does suffice to describe the statistical particle velocities, the population of atomic states, and the local ratio of emission to absorption of radiation (Stix 2004).

Whether or not LTE can be assumed depends on the *thermalization length*. This is the distance over which a particle or photon emitted in a certain collision or transition has undergone sufficient further collisions or absorption/emission processes so that it can no longer be distinguished within the respective distribution. In LTE the thermalization length must be shorter than the distance over which the temperature of the gas changes markedly.

The preceding definition of the local thermodynamic equilibrium makes clear that, at the same place in the atmosphere, LTE may be a good assumption for one particular process or pieces, but may be completely wrong for another. A crude rule of thumb is that the continuum in visible and infrared, the wings of most spectral lines, and the entire profile of weak lines are formed in LTE, while possible departures from LTE must be considered for the line cores and strong lines (Stix 2004).

The assumption of LTE constitutes a good approximation if collisional processes among particles dominate competing photoprocesses. For rarefied mater in stellar atmospheres and interstellar space, non-LTE effects come into play (Shu 1991). Departures from LTE occur in particular when collisional interactions are too rare to establish the

distributions discussed above. The thermalization length is large, and the distributions are influenced by photons coming from great distances, where different conditions (e.g., velocity or atomic state distributions) may prevail. Thus the state is "non-local" and often called "non-LTE (NLTE)". There may still be an equilibrium everywhere. However, the equilibrium is no longer characterized by a single temperature. In the solar atmosphere a characteristic situation is that the electrons satisfy a Maxwell distribution, with an *electron temperature* T_e, because collisions are still frequent. On the other hand, the population of atomic levels depends on radiative processes, which become rare in a rarefied gas.

1.2.2 The transfer equation

We want to study the propagation of light through a medium whose refractive indices may vary along the ray path, leading to a differential treatment. Along a ray, we can have emission and extinction. The emission contribution is proportional to the emissivity per unit volume, $j_\nu\,[\mathrm{W\,m^{-3}\,Hz^{-1}\,ster^{-1}}]$,

$$\mathrm{d}I_\nu(s) = j_\nu(s)\,\mathrm{d}s \tag{1.2}$$

where s measures the spatial coordinate along the ray (from the source toward the observer). Note that the intensity, I, is in $[\mathrm{W\,m^{-2}\,Hz^{-1}\,ster^{-1}}]$. The extinction contribution is proportional to the intensity itself,

$$\mathrm{d}I_\nu = -\sigma_\nu\, n\, I_\nu \mathrm{d}s \tag{1.3}$$

where σ_ν is the extinction coefficient or cross-section per particle in m^2, and n is the absorber number density $[m^{-3}]$. Using $\alpha_\nu = \sigma_\nu\, n$, the linear extinction coefficient $[m^{-1}]$, we have

$$\mathrm{d}I_\nu = -\alpha_\nu\, I_\nu \mathrm{d}s.$$

Therefore, we can write:

$$\mathrm{d}I_\nu(s) = j_\nu(s)\,\mathrm{d}s - \alpha_\nu\, I_\nu \mathrm{d}s. \tag{1.4}$$

The source function is defined as $S_\nu \equiv j_\nu(s)/\alpha_\nu$ and has the same units as intensity. In LTE, the most important simplification of the radiative transfer problem is the relation of $S_\nu = B_\nu(T)$ (Foukal 1990; Rutten 2003). Hence, we can write:

$$\frac{\mathrm{d}I_\nu}{\alpha_\nu\,\mathrm{d}s} = S_\nu - I_\nu.$$

The optical depth at frequency ν can be used as independent variable instead of s,

$$\mathrm{d}\tau_\nu = -\kappa_\nu\,\rho\,\mathrm{d}s = -\alpha_\nu\,\mathrm{d}s, \tag{1.5}$$

where κ_ν is the absorption coefficient (cross section per unit mass; $\mathrm{cm}^2\,\mathrm{g}^{-1}$) also called opacity (Eq. A.3), and ρ is the density. The transfer equation is then written as

$$\frac{\mathrm{d}I_\nu}{\mathrm{d}\tau_\nu} = I_\nu - S_\nu.$$

If the LOS is not along the local vertical of the atmosphere, we have to use the radial definition of the optical depth and introduce a factor μ (Rutten 2003),

$$\mu\,\frac{\mathrm{d}I_\nu}{\mathrm{d}\tau_\nu} = I_\nu - S_\nu. \tag{1.6}$$

Equation 1.6 describes the variation of intensity with optical depth; S_ν is the source function, i.e., the ratio between the emission and absorption coefficient, and $\mu = \cos\theta$ where θ is the heliocentric angle: the angle between the LOS and the vertical (outward) direction in the atmosphere. In the above transfer equation, two implicit assumptions are hidden:

1) The absorptive, dispersive, and emission properties of the medium are independent of the light beam entering into the medium. It is a justified assumption in many astrophysical aspects like stellar atmospheres (Landi Deglinnocenti & Landi Deglinnocenti 1981).

2) We have a steady-state radiation field so we can neglect the time-dependent terms, e.g., $\partial\, I/\partial\, t$ (del Toro Iniesta 2003).

Formal solution: It is possible to convert the transfer equation (Eq. 1.6) to evaluate an integral. Multiply both sides by $\mu^{-1}\exp(-\tau_\nu/\mu)$ and integrate; the result is

$$I_\nu(\tau_\nu,\,\mu) = I_\nu(\tau_{0\nu},\,\mu)\,\exp[-(\tau_{0\nu}-\tau_\nu)/\mu] + \mu^{-1}\int_{\tau_{obs}}^{\tau_{star}} S(\tau'_\nu)\exp(-\tau'_\nu/\mu)\mathrm{d}\tau'_\nu. \tag{1.7}$$

Assuming $\tau_{obs} = 0$ and $\tau_{star} = \infty$, i.e., deep into the star, then we have the total emergent intensity

$$I_\nu(0,\,\mu) = \frac{1}{\mu}\int_0^\infty S(\tau_\nu)\exp(-\tau_\nu/\mu)\mathrm{d}\tau_\nu. \tag{1.8}$$

If one knows the source function, it is possible to predict the emergent intensity. The more important application of this equation is to obtain the source function from the emergent intensity as a function of ν and μ.

1.3 Spectropolarimetry

Direct measurements of the Stokes profiles[2] became available with the invention of the magnetograph by Kiepenheuer (1953) and Babcock (1953). Nowadays, we measure Stokes

[2]By Stokes spectra or Stokes profiles we mean the dependence of I, Q, U and V on wavelength.

profiles with high spectral resolution using spectropolarimetry. A spectro-polarimeter is in principle a spectrograph with additional optical elements to modulate different Stokes parameters to intensity (which is directly measurable). The vector polarimeters which have been used in this thesis are the POlarimetric LIttrow Spectrograph (POLIS, Schmidt et al. 2003; Beck et al. 2005c) and the Hinode spectro-polarimeter (Ichimoto et al. 2008).

1.3.1 Thermal broadening and the Voigt function

The intensity profile of an absorption line has a finite width, usually much more than the natural broadening due to the uncertainty principle. One of the main broadening mechanisms in the solar atmosphere is the thermal broadening. In this part, we study this effect in order to derive a general mathematical form of an absorption profile which is the convolution of all broadening effects.

The random velocity of atoms shows a Maxwellian distribution (Reif 1965),

$$w_x(v_x) \sim \exp(-m_A\, v_x^2/2\, k\, T).$$

So, the most probable thermal velocity is $v_{th} = \sqrt{2\, k\, T/m_A} = 12.85\, \sqrt{T/10^4}\ \mathrm{km\,s^{-1}}$. Therefore, at $T = 6000\, K$, for iron ($A = 56$), $v_{th} = 1.33\, \mathrm{km\,s^{-1}}$. The normalized velocity distribution is

$$w_x(v_x) = \frac{1}{\sqrt{\pi}\, v_{th}} e^{-v_x^2/v_{th}^2}. \tag{1.9}$$

Due to Doppler effect, the velocity distribution will have a width of $\frac{\Delta\nu_{th}}{\nu_0} = \frac{v_{th}}{c}$ and the resulting profile will be a *Gaussian profile*:

$$\varphi(\nu) = \frac{1}{\sqrt{\pi}\, \Delta\nu_{th}} e^{-(\nu-\nu_0)^2/\Delta\nu_{th}^2}. \tag{1.10}$$

The Gaussian profile is symmetric about ν_0, has a maximum of $1/\sqrt{\pi}\, \Delta\nu_{th}$, and a full width at half maximum (FWHM) of $\Delta\nu_{\mathrm{FWHM}} = 2\sqrt{\ln 2}\, \Delta\nu_{th} = 1.67\, \Delta\nu_{th}$. The profile width shows a temperature dependency of $\Delta\nu_{th} \sim \sqrt{T}$. The numerical line width at $\lambda = 500\,\mathrm{nm}$, $T = 6000\,\mathrm{K}$, and for iron lines ($A = 56$) is $\Delta\lambda = 2\,\mathrm{pm}$, much larger than radiation damping (Appendix A). However, the decline of the Gaussian profile (e^{-x^2}) is much steeper than that of the Lorentz profile, the characteristic profile of the radiation damping, (x^{-2}). Therefore, in the line wing, the Lorentz profile is dominant. Fig. 1.3 (b) is an example of a strong scattering line profile that has wide Lorentz wings (Linsky & Avrett 1970). In a scattering line, a photon which was originally along our LOS was absorbed by an atom. This atom may deexcite radiatively, with the emission of a line photon in a different direction. No net effect would arise if every microscopic process was in balance with its reverse process. However, there exists an asymmetry on the solar surface: one side is the Sun and the other side is the cold dark space. Because of this asymmetry, there is a greater statistical tendency for photons originally travelled along our LOS to be scattered out of our LOS than there is for photons not originally along our LOS to be scattered into our LOS. Therefore, the net loss of line photons along our LOS comparing to nearby continuum leads to a scattering line.

Microturbulence: Chaotic motion (turbulence) with the length scales smaller than photon mean free path exist in the solar photosphere (Rutten 2003). In analogy to thermal broadening, we can attribute a Gaussian profile to the microturbulence broadening, $\zeta_{\rm mic}$ instead of $v_{\rm th}$ in Eq. 1.9. In the solar photosphere, $\zeta_{\rm mic} \approx 1.3\,{\rm km\,s^{-1}}$.

The Voigt function: There are a variety of broadening mechanisms in the solar atmosphere. Some of them have a Gaussian profile (e.g., thermal broadening) and some others a Lorentz profile (e.g., damping profile, see Appendix A). The two fundamental profiles that must be convolved to reach to an absorption line profile are the damping profile and the thermal broadening. The damping profile is the reaction of oscillators (atoms) to the external radiation field and the thermal broadening is due to random motion of atoms in the solar plasma. While the first one has a Lorentz profile, the second one has a Gaussian profile. To obtain the joint effect of these two broadening mechanisms, we have to convolve

$$G(\nu) = \frac{1}{\sqrt{\pi}\Delta\nu_D}\, e^{-(\nu-\nu_0)^2/\Delta\nu_D^2} \quad \text{with} \qquad L(\nu) = \frac{\gamma/4\pi^2}{(\nu-\nu_0)^2 + (\gamma/4\pi)^2},$$

where $\Delta\nu_D$ is the Doppler width and γ is the damping constant (see Appendix A). We define $V = G * L$ which depends on $\nu, \Delta\nu, \gamma$ and $\Delta\,\nu_D$,

$$V(\nu) = \int_{-\infty}^{+\infty} G(\nu')\, L(\nu-\nu')\, {\rm d}\nu'.$$

Using the following transformations, $v = (\nu-\nu_0)/\Delta\nu_D$, $a = \gamma/(4\,\pi\Delta\nu_D)$, and $y = (\nu'-\nu_0)/\Delta\nu_D$, we obtain

$$G(y) = \frac{1}{\Delta\nu_D\,\sqrt{\pi}}\, e^{-y^2}, \quad L(y) = \frac{a/\Delta\nu_D\,\pi}{y^2\,+\,a^2}, \quad \text{and } V = \frac{1}{\Delta\nu_D\,\sqrt{\pi}}\,\frac{a}{\pi}\int_{-\infty}^{+\infty}\frac{e^{-y^2}}{(v-y)^2+a^2}\,{\rm d}y.$$

The Voigt function is defined as $\mathcal{H}(a,\,v) = \Delta\nu_D\,\sqrt{\pi}\,V$,

$$\mathcal{H}(a,\,v) = \frac{a}{\pi}\int_{-\infty}^{\infty}\frac{\exp(-y^2)}{(v-y)^2+a^2}{\rm d}y, \quad \text{Normalization}: \int_{-\infty}^{+\infty}\mathcal{H}(a,\,v){\rm d}v = \sqrt{\pi}. \quad (1.11)$$

The Voigt function was first derived by Voigt (1913) and has no analytical representation. We can also define v as a function of wavelength,

$$v = (\lambda-\lambda_0)/\Delta\lambda_D, \quad (1.12)$$

where v is the dimensionless distance from the line center wavelength, λ_0. $\Delta\lambda_D$ is the Doppler width, which for a stellar atmosphere can be written as

$$\Delta\lambda_D = \frac{\lambda_0}{c}\sqrt{\zeta_{\rm mic}^2 + \frac{2\,k\,T}{M_{\rm a}}}. \quad (1.13)$$

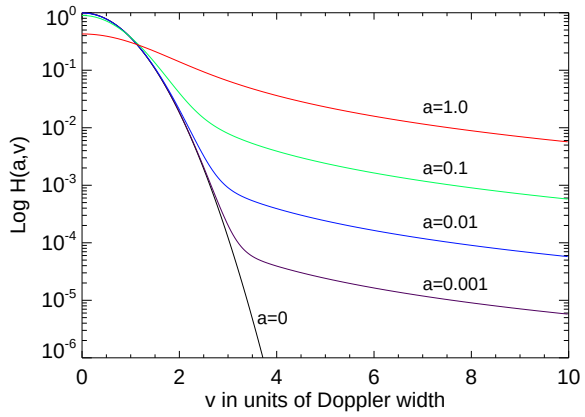

Figure 1.7: The Voigt function, $\mathcal{H}(a,\, v)$, for different a values, typical in the solar atmosphere. Note that $a = 0$ corresponds to a pure Gaussian profile (pure Doppler broadening). Each profile is normalized such that its integral is equal to unity.

Here $k = 1.38 \times 10^{23}\,\mathrm{J\,K^{-1}}$ is the Boltzmann constant, M_a is the mass of the atom, T is the temperature, ζ_mic is the microturbulence velocity (assuming that the microturbulence distribution is also Gaussian), and $c = 3\times10^8\,\mathrm{m\,s^{-1}}$ is the speed of light. Similarly, we can write a in Eq. 1.11 as a function of wavelength,

$$a = \frac{\gamma\lambda_0^2}{4\,\pi\,c\,\Delta\lambda_D} = \frac{\gamma}{4\,\pi\,\Delta\nu_D}, \tag{1.14}$$

where γ is the damping constant. For more details on the physical background of the Voigt function, see Mihalas (1978). $\mathcal{H}(a,\, v)$ is symmetric with respect to v,

$$\mathcal{H}(a,\, -v) = \mathcal{H}(a,\, v). \tag{1.15}$$

Figure 1.7 shows the Voigt function for different values of a.

1.3.2 Zeeman effect for an atomic energy level

In 1886, Pieter Zeeman (1865-1943) discovered the splitting of spectral lines in the presence of a magnetic field (Zeeman 1897). In the presence of a magnetic field, the energy of the atomic levels splits to a few sublevels. The new energy levels depend on the component of the total angular momentum along the magnetic field vector. The main observational consequence of this splitting of the atomic levels is a splitting of the spectral lines formed between two such levels into three groups of lines (Zeeman 1897). The unshifted component is called the π-component, while the shifted components are referred to as the $\sigma^{\pm}$-components.

We assumes that the magnetic field strength is weak enough that the LS-coupling is valid and the magnetic moment of the nucleus can be neglected, which is at least three orders of magnitude smaller than the electronic part, according to Sakurai (1985), and that the coupling of the atom to the external field is small compared to the spin-orbit interaction (as is the case for the magnetic field strength found on the Sun). In this

case, L, S, J, and M are quantum numbers that define the state of an atom. L, S, and J characterize the orbital angular momentum of electron, the spin angular momentum, and the total angular momentum, respectively. M is the magnetic quantum number and determines the component of the J along the magnetic field and can take values from $-J, -J+1, ..., J$. The Hamiltonian of an atom in an external magnetic field is to first order in $\mathbf{B}$ given by (Sakurai 1985):

$$\mathrm{H} = \mathrm{H}_0 + \mathrm{H}_1 = \mathrm{H}_0 + \frac{\mathrm{e}}{2\,\mathrm{m}\,\mathrm{c}}\,(\mathbf{L} + 2\,\mathbf{S})\,\mathbf{B} \tag{1.16}$$

where H_0 is the Hamiltonian of the atom without any external field, e is the (positive) charge of an electron, m is its mass, c is the speed of light, and $\mathbf{B}$ is the magnetic field vector. First order time-independent perturbation theory can then be applied. It is found that the (2J+1)-fold degeneracy in the energy of each level disappears (here $\hbar^2\,J(J+1)$ with $J = 0, \frac{1}{2}, 1, \frac{3}{2}, 2, ...$ is the eigenvalue of the squared total angular momentum operator $\mathbf{J^2}$, with $\mathbf{J} = \mathbf{L} + \mathbf{S}$), due to its splitting into magnetic sublevels whose energy is given by

$$E_{J,M} = E_J + \mu_0\,g\,M\,B. \tag{1.17}$$

In Eq. 1.17, E_J is the energy of the atomic level in the absence of a magnetic field (i.e., E_J is an eigenvalue of H_0), $\hbar\,M$ (with $M = -J, -J+1, ..., J$) is an eigenvalue of J_z, which is the component of the total angular momentum operator in the direction of the magnetic field, μ_0 is the Bohr magneton, $\mu_0 = e\,\hbar\,/\,(2\,m)$, B is the absolute value of $\mathbf{B}$, and g is the Landé factor. In LS-coupling the Landé factor can be written as

$$g = 1 + \frac{J\,(J+1) + S\,(S+1) - L\,(L+1)}{2\,J\,(J+1)}. \tag{1.18}$$

A first version of this equation was given by Landé in 1923 but the correct physical meaning of the different quantum numbers, especially of the spin, was not realized until 1925. In general, there are Zeeman multiplets (instead of triplet) where single components are usually not resolved. In this case, an effective g-factor is usually calculated based on the contributing components. Beckers (1969) and Harvey (1973) presented g_{eff} for a large number of spectral lines with large Zeeman splitting. If $S = 0$ (i.e., no spin) then $g = 1$, while if $L = 0$ (i.e., only spin) then $g = 2$. For some levels (e.g., $^4D_{1/2}$,$^5F_1$) the Landé factor is zero and these levels do not split in the first order perturbation theory.

1.3.3 Description of polarized light: Stokes parameters

Polarization is an important property of the electromagnetic waves and any kind of waves with a transverse character. Historically, Erasmus Bartholinus in 17th century studied the propagation of light in double-refraction crystals. Following him, Huygens and Newton studied this effect in the framework of their own optical theories. The word *polarization* was first introduced by E. L. Malous in 1809 (Landi degl'Innocenti 1999). He proved that the polarization is an intrinsic property of light and is not induced by the medium. There are a variety of examples in which we can study polarization: from reflection and

refraction of a beam of light at the separation surface between two dielectric media to a variety of radiation and scattering processes. The most obvious example of polarization in everyday life is the polarization of blue sky which is due to scattering of sunlight by the air molecules (Rayleigh scattering).

Four parameters are required for a complete and consistent description of polarized radiation (including partial polarization), and since the work of Chandrasekhar (1947, 1950) the system of four Stokes parameters has established itself as the standard representation in optical solar physics and stellar astronomy. This system has the advantage that it only contains real numbers which are directly measureable, all have the same physical dimension, a direct relationship to the physical processes of the studied object, and they allow the radiative transfer equation to be written in a straightforward manner.

In Cartesian coordinates, the oscillation of the electric field vector (E_x, E_y) of light propagating in the z-direction can be written as

$$\begin{aligned} E_x &= \xi_x \cos(\omega\, t - \varepsilon_x) \\ E_y &= \xi_y \cos(\omega\, t - \varepsilon_y) \end{aligned} \tag{1.19}$$

where ω is the angular frequency of the vibration, ξ_x and ξ_y are the constant amplitudes of the electric vector in the x and y directions, and ε_x and ε_y are its respective phases. Alternatively, one can use $\{\, I,\, Q,\, U,\, V\}$ instead of $\{\, \xi_x,\, \xi_y\, \varepsilon_x,\, \varepsilon_y\}$:

$$\begin{aligned} I &= < \xi_x^2 > + < \xi_y^2 >, \\ Q &= < \xi_x^2 > - < \xi_y^2 >, \\ U &= 2\ < \xi_x\, \xi_y \cos(\varepsilon_x - \varepsilon_y) >, \\ V &= 2\ < \xi_x\, \xi_y \sin(\varepsilon_x - \varepsilon_y) > . \end{aligned} \tag{1.20}$$

In Eqs. 1.20, I, Q, U and V are the Stokes parameters named after Sir George Gabriel Stokes (1819-1903), who first introduced them[3]. According to his principle of optical equivalence, beams of light which have the same Stokes parameters are indistinguishable as regards intensity and degree of polarization. For totally polarized light, the average over time is not necessary. It then follows directly from Eqs.1.20 that

$$I^2 = Q^2 + U^2 + V^2. \tag{1.21}$$

Figure 1.8 shows a definition of the Stokes parameters. The degree of the linear and circular polarization is defined as $L(\lambda)/I(\lambda)$ and $V(\lambda)/I(\lambda)$, where $L(\lambda) = \sqrt{Q(\lambda)^2 + U(\lambda)^2}$.

Let $S_{\rm n}(M,\, \gamma)$ be the unnormalized relative strengths of the different Zeeman components, when viewed at the angle γ to the field direction, in an optically thin medium, under the assumption that all Zeeman sublevels are equally populated, $n = \Delta\, M = 0, \pm 1$ and $-J \ \leq\ M \ \leq\ J$ where $\hbar\, M$ is the eigenvalue of the J_z. However, the exact limits to the value of M depend on $\Delta\, M$ and $\Delta\, J$. Both J and M refer to the initial state of

[3]The brackets <> denote averaging over time to account for finite bandwidth of the light.

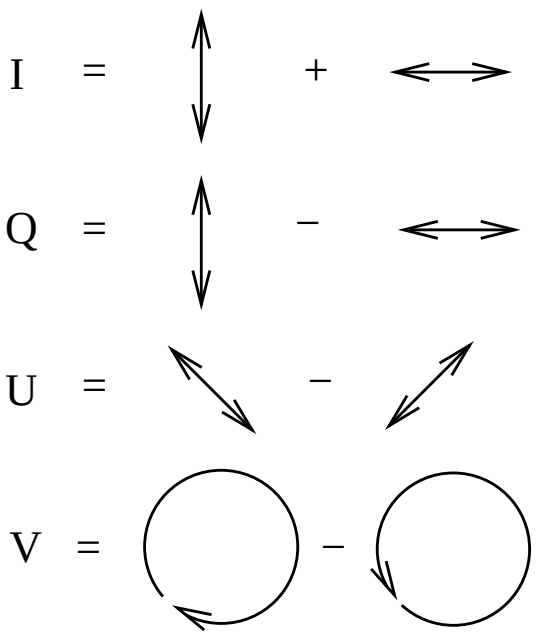

Figure 1.8: Pictorial representation of the Stokes parameters. The observer is supposed to look at the radiation source. Note that Stokes-I, the polarized intensity, can also be defined as $I = I^{45}_{Lin} + I^{135}_{Lin} = I^{L}_{Cir} + I^{R}_{Cir}$, where I^{L}_{Cir} and I^{R}_{Cir} denote the left and right circular polarizations, respectively.

the atom. $S_{\rm n}(M,\, \gamma = \pi/2)$ values for a dipole radiation are given in Condon & Shortley (1964). For use in radiative transfer calculations, these strengths have to be normalized such that

$$\sum_{M} S_{\rm n}(M,\, \gamma = \pi/2) = 1 \quad (n = 0, \pm 1). \tag{1.22}$$

The strengths of individual Zeeman components for an arbitrary angle γ can be determined from the strengths at $\gamma = \pi/2$ via the Seares formula (Seares 1913):

$$\begin{aligned} S_0(M,\, \gamma) &= S_0(M,\, \gamma = \pi/2)\sin^2\gamma, \\ S_{+1}(M,\, \gamma) &= S_{+1}(M,\, \gamma = \pi/2)(1 \pm \cos\gamma)^2, \\ S_{-1}(M,\, \gamma) &= S_{+1}(M,\, \gamma = \pi/2)(1 \mp \cos\gamma)^2, \end{aligned} \tag{1.23}$$

where upper and lower signs in the right-hand-side of Eq. 1.23 are applicable for right- and left-handed circular analyzers respectively. For the three groups of Zeeman components ($\Delta M = 0,\, \pm 1$) the profiles in a stationary optically thin medium are

$$\begin{aligned} \Phi_0 &= \sum_{M} S_0(M,\, \pi/2) \;\; \mathcal{H}(a,\, v - v_0(M)), \\ \Phi_{+1} &= \sum_{M} S_{+1}(M,\, \pi/2) \;\; \mathcal{H}(a,\, v - v_{+1}(M)), \\ \Phi_{-1} &= \sum_{M} S_{+1}(M,\, \pi/2) \;\; \mathcal{H}(a,\, v - v_{-1}(M)), \end{aligned} \tag{1.24}$$

when viewed perpendicularly to the magnetic field. In Eq. 1.24, $\mathcal{H}(a,\, v)$ is the Voigt

function (Sect. 1.3.1), and,

$$v_n(M) = \frac{e\,\lambda_0^2\,B}{4\,\pi\,m\,c^2\,\Delta\lambda_D}\,g_n(M) = 4.67\,\times\,10^{-18}\,\frac{\lambda_0^2\,B}{\Delta\lambda_D}\,g_n(M) \qquad (n\,=\,0,\,\pm1) \qquad (1.25)$$

is the dimensionless wavelength shift of the Zeeman component (λ_0 and $\Delta\lambda_D$ are in nm and B is in Tesla).

In the presence of a strong magnetic field, when the two lobes of Stokes-V are completely separated, we can use the distance between the σ component and the profile center as a measure of the magnetic field strength by (Stix 2004; Landi degl'Innocenti & Landolfi 2004):

$$\Delta\lambda = 4.67 \times 10^{-18}\lambda^2 B g_{\rm eff}, \qquad (1.26)$$

where $g_{\rm eff}$ is the effective Landé factor, $\Delta\lambda$ and λ are in nm, and B is in Tesla[4]. This condition is usually fulfilled in near-IR spectral lines (e.g., Rezaei et al. 2006a). It is because the Doppler width is linear with λ (Eq. 1.13) while the Zeeman splitting is quadratic (Eq. 1.26).

1.3.4 The Faraday-Voigt function

In the previous sections, we saw that the general profile of an absorption line is a Voigt function. To find the profiles of Stokes-$Q/U/V$, we have to know the dispersion profile also. The complex refractive index of light in a conducting medium is (del Toro Iniesta 2003; Landi degl'Innocenti & Landolfi 2004),

$$n_\alpha = 1 + \delta_\alpha + i\kappa_\alpha,$$

where both δ_α and κ_α are much smaller than unity. $(1\,+\,\delta)$ is the real refractive index and κ is the extinction coefficient. This assumption is valid in stellar atmospheres where the densities are so low that the real refractive index is not far from unity and at the same time conductivity is not negligible. The coefficient

$$\chi_\alpha = \frac{2\,\omega}{c}\,\kappa_\alpha \qquad (1.27)$$

is known as the absorption coefficient for light polarized in direction α and

$$\xi_\alpha = \frac{2\,\omega}{c}\,\delta_\alpha \qquad (1.28)$$

is known as the dispersion coefficient for light polarized in direction α. Using Lorentz electron theory of a classically damped oscillator (Appendix A), one can derive absorption and dispersion profiles. This is due to the Kramers-Kronig (dispersion) relations for $(n-1)$ which create a mutual interaction between δ and κ, i.e., between the phase velocity of light in the medium and its absorption (Kronig 1925). When the absorption profile has

[4] $1\,\text{Tesla} = 10^4\,\text{G}$.

the shape of a Voigt function, the corresponding dispersion profile is proportional to the Faraday-Voigt function or dispersion profile:

$$\mathcal{F}(a,\, v) = \frac{1}{2\,\pi} \int_{-\infty}^{\infty} \frac{(v-y)\, \exp(-y^2)}{(v-y)^2 + a^2} \mathrm{d}y, \tag{1.29}$$

where a and v are given in Sect. 1.3.1. In contrast to the Voigt function, $\mathcal{F}(a,\, v)$ is antisymmetric in v, i.e.,

$$\mathcal{F}(a,\, -v) = -\mathcal{F}(a,\, v). \tag{1.30}$$

Now consider the case of radiation passing through a medium with a magnetic field. Then, a spectral line will split into its individual Zeeman components, i.e. $\kappa(\nu) \longrightarrow \kappa_0 \sim \Phi_0$, $\kappa_{-1} \sim \Phi_{-1}$, $\kappa_{+1} \sim \Phi_{+1}$ where $\Phi_{0,\pm1}$ are given in Eq. 1.24. This means that $n(\nu)$ *will also split into Zeeman components*, which we call in analogy n_0, n_{-1}, n_{+1}. The normalized dispersion profiles $\Psi_0 \sim n_0 - 1$, $\Psi_{+1} \sim n_{+1} - 1$, $\Psi_{-1} \sim n_{-1} - 1$ of the line, when viewing perpendicularly to the magnetic field, can then be written as

$$\begin{aligned}
\Phi_0 &= 2 \sum_M S_0(M, \pi/2)\, \mathcal{F}(a,\, v - v_0(M)), \\
\Phi_{+1} &= 2 \sum_M S_{+1}(M, \pi/2)\, \mathcal{F}(a,\, v - v_{+1}(M)), \\
\Phi_{-1} &= 2 \sum_M S_{-1}(M, \pi/2)\, \mathcal{F}(a,\, v - v_{-1}(M)).
\end{aligned} \tag{1.31}$$

Note that the absorption and dispersion profiles (Eqs.1.24 and 1.31) explained in this section are results of the semi-classical theory. The random motion of atoms which broadens the absorption and dispertion profiles, has been taken into account in the Voigt and Faraday-Voigt functions. Quantum mechanical corrections are explained in the next section.

1.3.5 The transfer equation for polarized light

The radiative transfer equation (RTE) for polarized light in the presence of a magnetic field and in a plan-parallel atmosphere was first solved by Unno (1956). Rachkovsky (1962) expanded it to include magneto-optical effects. Domke (1971) self-consistently took into account departures from LTE in a two level atom. The transfer equation in this case reads (Wittman 1974; del Toro Iniesta 2003):

$$\mu \frac{\mathrm{d}}{\mathrm{d}\tau} \begin{pmatrix} I \\ Q \\ U \\ V \end{pmatrix} = \begin{pmatrix} \eta_\mathrm{I} & \eta_\mathrm{Q} & \eta_\mathrm{U} & \eta_\mathrm{V} \\ \eta_\mathrm{Q} & \eta_\mathrm{I} & \rho_\mathrm{V} & -\rho_\mathrm{Q} \\ \eta_\mathrm{U} & -\rho_\mathrm{V} & \eta_\mathrm{I} & \rho_\mathrm{Q} \\ \eta_\mathrm{V} & \rho_\mathrm{U} & -\rho_\mathrm{Q} & \eta_\mathrm{I} \end{pmatrix} \begin{pmatrix} I \\ Q \\ U \\ V \end{pmatrix} - \mathbf{S}_\nu \begin{pmatrix} \eta_\mathrm{I} \\ \eta_\mathrm{Q} \\ \eta_\mathrm{U} \\ \eta_\mathrm{V} \end{pmatrix}. \tag{1.32}$$

In the above equation, η and ρ are made of absorption and dispersion profiles. They are a function of the characteristics of the medium and the geometry of the problem:

$$\eta_{\rm I} = \frac{1}{2}\left\{\xi_0 \sin^2\theta + \frac{1}{2}\left[\xi_{+1}+\xi_{-1}\right]\left(1+\cos^2\theta\right)\right\} \tag{1.33}$$
$$\eta_{\rm Q} = \frac{1}{2}\left\{\xi_0 - \frac{1}{2}\left[\xi_{+1}+\xi_{-1}\right]\right\}\sin^2\theta\,\cos 2\phi$$
$$\eta_{\rm U} = \frac{1}{2}\left\{\xi_0 - \frac{1}{2}\left[\xi_{+1}+\xi_{-1}\right]\right\}\sin^2\theta\,\sin 2\phi$$
$$\eta_{\rm V} = \frac{1}{2}\left[\xi_{+1}-\xi_{-1}\right]\cos\phi$$
$$\rho_{\rm Q} = \frac{1}{2}\left\{\chi_0 - \frac{1}{2}\left[\chi_{+1}+\chi_{-1}\right]\right\}\sin^2\theta\,\cos 2\phi$$
$$\rho_{\rm U} = \frac{1}{2}\left\{\chi_0 - \frac{1}{2}\left[\chi_{+1}+\chi_{-1}\right]\right\}\sin^2\theta\,\sin 2\phi$$
$$\rho_{\rm V} = \frac{1}{2}\left[\chi_{+1}-\chi_{-1}\right]\cos\phi$$

where $\xi_{0,\pm1}$ are absorption profiles and $\chi_{0,\pm1}$ are dispersion profiles:

$$\xi_{0,\pm1} = \frac{\kappa_L(\lambda_0)}{\kappa_c}\Phi_{0,\pm1}, \tag{1.34}$$

where $\Phi_{0,\pm1}$ is given by Eq. 1.24, κ_c is the continuum opacity, and $\kappa_L(\lambda_0)$ is the line center absorption coefficient in absence of magnetic field (Mihalas 1978). The absorption profiles, $\Phi_{0,\pm1}$, are symmetric w.r.t. the line center wavelength. θ is the inclination and ϕ is the azimuth angle of the magnetic field vector w.r.t. LOS. In the magneto-optical terms ($\rho_{\rm Q}$, $\rho_{\rm U}$, and $\rho_{\rm V}$) in the transfer equations (Eqs. 1.32 and 1.33),

$$\chi_{0,\pm1} = \frac{\kappa_L(\lambda_0)}{\kappa_c}\Psi_{0,\pm1}, \tag{1.35}$$

where $\Psi_{0,\pm1}$ are given in Eq. 1.31. Eqs. 1.33 provide absorption and dispersion profiles for the electric dipole radiation. The dispersion profiles, $\Psi_{0,\pm1}$, are antisymmetric w.r.t. the line center wavelength. For electric quadrupole and magnetic dipole see Beckers (1969). In both Eqs. 1.34 and 1.35 the $\frac{\kappa_L(\lambda_0)}{\kappa_c}$ term accounts for the quantum mechanical effects, e.g. the oscillator strength[5].

Symmetry properties of Stokes profiles: Considering the symmetry properties of the absorption and dispersion profiles (Eqs. 1.33), and the transfer equation (Eq. 1.32), it is clear that under transformation of $\Delta\lambda \rightarrow -\Delta\lambda$, $I(\lambda)$, $Q(\lambda)$, and $U(\lambda)$ remain the same while $V(\lambda)$ changes sign. It means that the $V(\lambda)$ profile is antisymmetric w.r.t. the line center wavelength while the other Stokes profiles are symmetric (in absence of velocity and magnetic field gradients, Illing et al. 1975).

[5]The oscillator strength is a quantity that was historically introduced to correct harmonic oscillator line strength predictions for unknown quantum-mechanical effects (see Appendix A).

Magneto-optical effect: Anomalous dispersion or magneto-optical effect is a phenomenon that is due to the dephasing of the two components of the electric field vector inside an anisotropic medium. Since Michael Faraday discovered this phenomenon in the light travelling through a magnetized medium (magnetic field along the direction of propagation), it is also known as Faraday rotation. The sole reason for the Faraday rotation is that in presence of magnetic field, not only the absorption coefficients split into their Zeeman components, but also the refractive indices split into their Zeeman components. It is due to mutual effects of refractive index and absorption coefficients in the dispersion relation. Hence, the medium becomes birefringent and acts similarly to certain crystals which are naturally birefringent, e.g., calcite or quartz. Therefore, waves with different polarization states travel at different velocities in these media. The magneto-optical terms in the transfer equation (Eq.1.32), $\rho_{\rm Q}$, $\rho_{\rm U}$, $\rho_{\rm V}$ to some extent couple different polarization states.

1.4 Synthesis and inversion of spectral lines

Spectral lines sample a height range in the stratified solar atmosphere. Hence, they carry information on the average properties of the atmosphere along the LOS. Therefore, observed Stokes profiles provide limited information about the physical condition under which they are formed. We measure a set of parameters like the line-core position of Stokes-I or the Stokes-V peak distance and use them as a measure of the line-of-sight velocity and the magnetic field strength. All these parameters are single values whereas the corresponding physical quantities are a function of optical depth. Therefore, we have to understand the intrinsic limitation of the information a spectral line carries. Using response functions (del Toro Iniesta 2003), one can show that the measured parameters are averages of the actual stratification weighted by the corresponding contribution or response functions. In a theoretical approach, it is possible to calculate synthetic profiles that emerge from a model atmosphere uniquely. Observationally, we measure the emerged Stokes profiles, which can be used to *estimate* the physical conditions.

SIR (Stokes Inversion based on Response functions) is a package for the synthesis and inversion of spectral lines formed in the presence of magnetic fields (Ruiz Cobo & del Toro Iniesta 1992; Bellot Rubio 2003). We used the SIR code in this thesis. The code takes into account the Zeeman-induced polarization of light and deals with all four Stokes parameters (I, Q, U, V) of any electric dipole transition and atomic species. SIR was developed for the automated analysis of solar spectra under LTE conditions. Lites et al. (2007a) presented a list of other inversion codes comparable to SIR. All such codes have the same limitations, namely the LTE assumption.

In synthesis mode, the program calculates the Stokes spectra emerging from any specified model atmosphere which may consist of up to two different components (either magnetized or nonmagnetized). This is done by numerically solving the radiative transfer equation (Eq.1.32) for polarized light. Figure 1.9 shows the synthetic Stokes-V profiles for different magnetic field strengths calculated with the SIR code. In inversion mode,

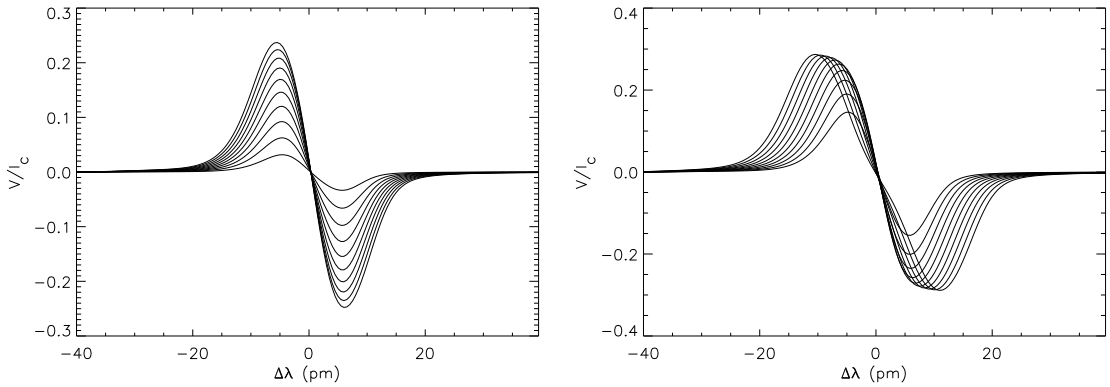

Figure 1.9: Synthetic Stokes-V profiles of Fe I 630.25 nm line for different values of the magnetic field strength. *Left:* $\mathbf{B} = 100 - 1000$ with steps of 100 G. *Right:* $\mathbf{B} = 500 - 2300$ with steps of 200 G. For small magnetic field strength, the amplitude increases while at about 1 kG, the amplitude saturates and the distance between the two lobes increases. The inclination and azimuth were set to zero. Other parameters are similar to the HSRA model atmosphere (Gingerich et al. 1971).

SIR fits any combination of observed Stokes parameters for any arbitrary number of spectral lines and provides estimates for the uncertainties in the calculated parameters. To this end, an initial model atmosphere is iteratively modified until the synthetic Stokes profiles match the observed ones. This process yields estimates for the thermal, dynamic and magnetic structure of the atmosphere in which the observed profiles are formed. The inversion process is based on the minimization of a merit function, χ^2, which is the sum of the squared differences between observed and synthetic data weighted by the uncertainties of the observations:

$$\chi^2 \equiv \sum_{k=1}^{4} \sum_{i=1}^{M} \left[I_k^{\rm obs}(\lambda_i) - I_k^{\rm syn}(\lambda_i) \right]^2 \frac{w_k^2}{\sigma^2}, \tag{1.36}$$

where index $k = 1, \ldots, 4$ samples the 4-component vectors containing the observed (obs) and synthetic (syn) Stokes profiles, $i = 1, \ldots, M$ sample the wavelengths at which the spectrum has been measured, σ is the uncertainty of the observations, and w_k denotes the importance of each Stokes parameter.

The inversion module of SIR implements a Marquardt[6] nonlinear least-squares algorithm (Press et al. 1986) for the minimization of the differences between the observed and synthetic Stokes spectra. Knowledge of the partial derivatives of the Stokes parameters with respect to the various atmospheric parameters, the so-called *response functions* (RFs), is crucial for the success of the inversion. Thus, the synthesis module of SIR calculates all the necessary RFs (Ruiz Cobo & del Toro Iniesta 1994). SIR has been suc-

[6]Marquardt's method translates the nonlinear problem into a linear one, the solution of which is carried out by means of a modified singular value decomposition (SVD) algorithm (Press et al. 1986).

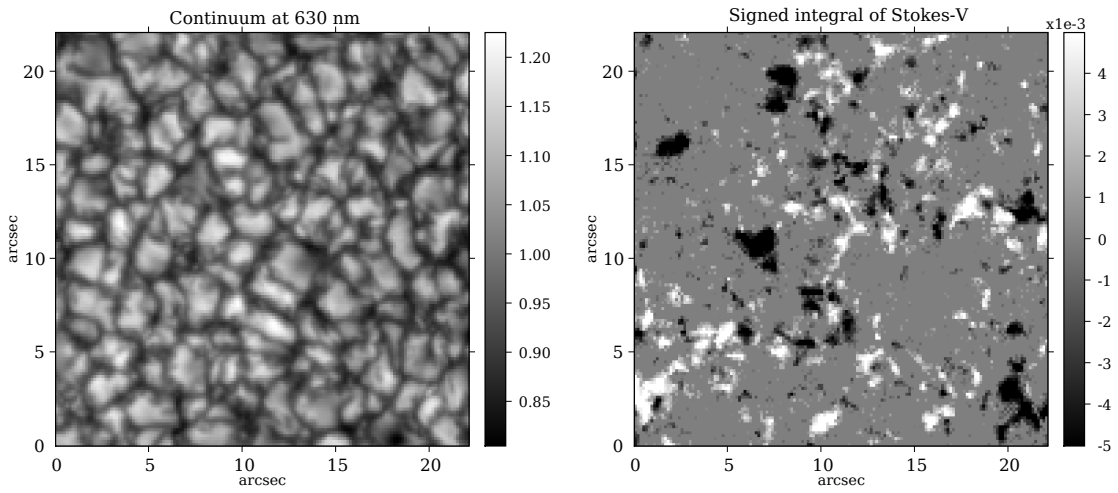

Figure 1.10: Sample of magnetic elements in continuum intensity (left) and polarized light (right). The observations were carried out using the spectropolarimeter on-board Hinode. Note the many small-scale opposite-polarity magnetic signals that leave almost no signature in the continuum intensity map.

cessfully applied to the study of different solar structures observed in polarized light, such as sunspots (Collados et al. 1994; Westendorp Plaza et al. 1998) and unresolved magnetic elements (Bellot Rubio et al. 1997). In these analyses, model atmospheres were retrieved from the observed Stokes spectra.

1.5 Magnetic elements: small-scale solar magnetism

Magnetic features are best studied in polarized light, since the Zeeman effect gives a very definite spectro-polarimetric signature which allows to identify them. Although it is enough to consider only the intensity profile of a Zeeman-split line in order to derive the field strength, in practice the splitting in solar magnetic features is often smaller than the thermal and Doppler width of a spectral line. So it is not possible to clearly separate the effects of a magnetic field from other line broadening agents. However, the effect of the magnetic field can be identified due to the distinctive polarization signature. For a longitudinal field ($\mathbf{B} \parallel$ LOS) in an absorption line spectrum, no π-component is visible ($\gamma = 0$ in Eq. 1.23) and the two σ-components are oppositely circularly polarized. For a transverse field ($\mathbf{B} \perp$ LOS) in an absorption line spectrum, the π-component is linearly polarized parallel to $\mathbf{B}$, while the σ-components are linearly polarized perpendicular to $\mathbf{B}$ (see Eqs.1.33). The situation is reversed in an emission line spectrum.

Source of the magnetic field: A dynamo mechanism is believed to be the source of the solar magnetic field. There is a layer placed in-between the convection zone and the

radiative core which plays the role of a flux storage. Systematic features such as the solar cycle, Hale's polarity law, and the butterfly diagram point at the existence of a deep root of the large-scale magnetic field (Ossendrijver 2003).

Magnetic elements: The magnetic field in the photospheric layer is concentrated in active regions and in the network. In active regions (outside sunspots), the magnetic field is concentrated into more or less discrete features that together form faculae or plage regions. In the quiet Sun (i.e., outside active regions) the magnetic flux elements form a network outlining the borders of supergranular cells with a length scale of 20–40 Mm. Another type of magnetic feature in the quiet Sun is the inter-network element, which is located in the interior of supergranular cells. On a more localized scale, the magnetic elements forming faculae and the network, and very likely also those in the inter-network, are located in the downflow lanes between granules.

Magnetic elements are bright structures with diameters smaller than a few hundred kilometres (Steiner et al. 2001). High-resolution observations show magnetic features with sizes down to the achievable spatial resolution of $\sim$70 km. Observations indicate that most of the longitudinal magnetic flux passing through the photosphere is concentrated in *magnetic elements*, i.e., patches of high field strength that are embedded in relatively field-free plasma (Solanki 1993). The magnetic axes of the elements are nearly vertical because of the buoyancy of the top of the expanded flux tubes. In the hierarchy of the magnetic elements, the magnetic knots take the position between dark and bright structures, i.e., between pores and network bright points. While the magnetic knots are not visible in continuum or line wings, they appear as bright features in the core of Ca II H and K lines. The magnetic elements expand with height so that the intensity contrast in higher layers is larger. Moreover, magnetic features are partially evacuated, so one sees deeper layers (*Wilson depression*). The resulting *hot walls* are best seen away from the disk center. This leads to an enhancement of photospheric emission from the faculae near the limb of the Sun (Steiner 2005a; Hirzberger & Wiehr 2005; De Pontieu et al. 2006).

Magnetic flux tubes: Flux tubes are considered as building blocks of the solar magnetic field. Magnetic flux often appears in the form of intense, isolated elements surrounded by flux-free, or nearly flux-free plasma. This observation, together with the fact that the solar plasma has high electrical conductivity ($\sim$10-100 $\Omega^{-1}\,\mathrm{m}^{-1}$ Kubat & Karlicky 1986) and therefore the magnetic field is nearly frozen into the ambient fluid, has led to the development of the flux tube as a useful idealization of magnetic behavior (Parker 1979). Because of its simple geometrical structure and conceptual appeal, it is often easier to describe magnetic phenomena in terms of a flux tube or a collection of such objects than in terms of a continuous magnetofluid. An isolated flux tube can be imagined like a bright point in a G-band image (Fig. 1.1). It is, however, not clear what is the diameter of a thin flux tube (Steiner 1999; Cattaneo et al. 2006; Steiner 2007).

The magnetic and kinetic energies: In a magnetic element (cf. Fig. 1.10) or a flux tube, the plasma β ($= 2\,\mu_0\,\mathrm{P}/\mathrm{B}^2$) in the solar photosphere is about 0.2–0.4 (for $B = 0.1$ T

and a gas pressure of about 100 Pa). Thus, locally the magnetic energy density can exceed the thermal energy density, although, because of the small area coverage by strong fields, most of the energy is in the form of the thermal energy of the gas (Solanki et al. 2006). The situation changes rapidly as one moves higher in the atmosphere. Since the gas pressure and the magnetic field strength decrease exponentially with height, the plasma β remains approximately constant, but above a certain height, which typically lies in the chromosphere, the expanding magnetic flux tube fills the whole volume.

When $\beta \ll 1$, the plasma motion is governed by the magnetic field lines, while $\beta \gg 1$ implies that the field lines move along with the flow field. In the photosphere, β is usually larger than unity, except inside magnetic structures. Using typical values for the bulk velocity and density of the matter in granulation and the field strength of a flux tube, one finds that the ratio of the magnetic to kinetic energy density, $B^2/\mu_0\,\rho\,v^2$, is larger than unity inside flux concentrations and smaller than unity outside.

Contrast: The continuum contrast of magnetic structures differs significantly between the largest and the smallest ones. The umbrae of the largest sunspots are the darkest structures observed in the solar photosphere. In pores (naked umbrae) the intensity is larger than in umbrae of large sunspots, whereas in magnetic knots and azimuth centers, there is no trace in the continuum intensity, i.e., they show the same intensity as non-magnetic structures (Keppens & Martinez Pillet 1996). The trend of increasing intensity with decreasing size/flux of magnetic structures ends with small-scale magnetic elements like facular or G-band bright points which are some 15 % brighter than nearby continuum (depending on the wavelength, Schüssler et al. 2003; Steiner et al. 2003). The continuum contrast reaches 40 % for solar limb faculae (Blanco Rodríguez et al. 2007).

If a facular or G-band bright point represents a thin flux tube, and a pore represents a thick flux tube, then we have to explain why the former appears as bright feature, while the latter is dark (and why magnetic knots are entirely invisible in the continuum, Stix 2004). The strong magnetic field inhibits the convective transport of the energy, as was first recognized by Biermann (1948) in the context of sunspots. The reason is that the field is frozen into the plasma but too strong to suffer the kinetic effects: it prevents the overturn motion. A consequence is a reduced energy input from below and hence a reduced temperature at any given level, both in the thin and thick tubes. The difference in thin and thick tubes is that the lateral influx of heat, which is only by radiative transport and therefore inefficient, cannot heat the thick tube (except a thin outer layer) but does suffice to heat the thin tube up to a temperature that is above the photospheric temperature (at the same optical depth). Now, because the opacity decreases with decreasing temperature and density (the density is reduced in the tube), we can see deeper into the tube than in the surrounding photosphere. The result is that in the thin tube, we see material that is hotter, and thus brighter, than the photospheric material, while the opposite is true for the thick tube. Spruit (1976), who first presented this argument, found that the transition from thin bright tubes to thick dark tubes should occur at a tube diameter of about 600 km. In this intermediate region the magnetic knots should then be found.

Table 1.3: Comparison between magnetic structures on the solar surface (Solanki 1999; Zwaan 1987). BPs stands for bright points and ACs for azimuth centers (Martínez Pillet et al. 1997).

parameter	BPs	Mag knots	ACs	pores	sunspots
magnetic flux (10^{18} Mx)	∼0.1	∼10	<40–50	50 – 250	$500 - 3 \times 10^4$
dimension (Mm)	<0.2	0.6	≤3.0	0.1 – 7	4 – 60
continuum intensity	> 1.1	1.0	1.0	0.2 – 0.7	0.05 – 0.3

The magnetic flux of a typical magnetic knot is about 10^{19} Mx[7], an order of magnitude less than in pores. For comparison, the magnetic flux of an isolated bright point, with a dimension of about 100 km and a magnetic field strength of about 1 kG is $\approx 10^{17}$ Mx (Table 1.3).

Formation: The current physical picture of the formation of magnetic elements involves a two-stage process. In a first step, the convection (i.e. the granular flow) expels the initially weak and relatively homogeneously distributed magnetic flux into the intergranular downflow lanes (Weiss 1966). This process is called *flux expulsion* (Schüssler 1990) and can concentrate the field until it is roughly in equipartition with the flow, i.e. the magnetic energy density equals the kinetic energy density, $B \sim \sqrt{\mu_0 \rho}\, v$, where ρ is the gas density and v is the average horizontal convective flow speed. For the solar photosphere, values of 100–400 G are thus obtained, depending on the height to which they refer and on the value of the convective velocity assumed. Of considerable importance for the further concentration of the magnetic flux is an instability, the so-called *convective collapse*, which is driven by the cooling, through radiative losses at the solar surface, of the gas trapped between the field lines (Grossmann-Doerth et al. 1998). During the gas cooling process, its density increases, so that it sinks and settles in deeper layers, leading to low pressure in the upper layers of the flux concentration. The pressure of the surrounding gas pushes the field lines together, thus strengthening the field to about kilogauss values at the solar surface. A field of this strength quenches convection and stops the instability from growing further. Radiative heating (mainly through the side walls of the flux concentration) keeps the gas from cooling further and thus allows the magnetic element to approach a stable magneto-static state (Spruit 1976, 1979). Since the lateral influx of heat is more efficient for more slender flux tubes (which have a larger ratio of wall area to volume and which are less optically thick), the less flux in a small-scale magnetic feature, the lower the final field strength. Although there were observational attempts to record the convective collapse, few confirmations have been reported so far (Solanki et al. 1996; Bellot Rubio et al. 2001; Beck et al. 2006; Nagata et al. 2008)

Evolution: New magnetic flux emerges into the solar atmosphere in the form of bipolar magnetic regions (Hagenaar 2001, and references therein). The emergence sites are bright

[7] $1\,\mathrm{Mx} = 10^{-8}\,\mathrm{Wb}$.

in chromospheric lines like Ca II H (Li et al. 2007). During emergence, the field initially is relatively weak (being a few hundred Gauss) and predominantly horizontal (Lites et al. 2008). At this point we are seeing the top of the emerging loop. As the loop continues to rise, its two photospheric footpoints move apart and the field gets stronger and nearly vertical (Lites et al. 1998). Right from the beginning, the field interacts with convection. At the location of flux emergence, the granulation is heavily disrupted. This interaction continues throughout the lifetime of the magnetic flux, although the field and convection segregate early (such that the magnetic flux then lies in the intergranular convective downflow lanes). As the granules evolve and move, the flux located between them is forced to move along, wandering with the intergranular lanes. Finally, it is probably the turbulence associated with convection which buffets and twists the field on a small-scale, bringing opposite polarities together and thus allowing for the dissipation of magnetic energy.

We know little about the dynamics of small magnetic elements. High-resolution filtergraphs exhibit their random walk in the solar photosphere (Rouppe van der Voort et al. 2005). Polarimetric observations have so far provided only limited information on the evolution of individual magnetic elements. It is because polarimetric data with high temporal resolution is not available due to the relatively long integration time required for spectropolarimetric measurements. This long integration time also degrades the spatial resolution in polarimetric measurements. Since each flux tube is thought to be the footpoint of a bundle of field lines reaching up into the corona, such a random walk leads to the twisting of field lines at greater heights. This in turn produces a build-up of magnetic energy and the formation of spontaneous current sheets and tangential discontinuities (Parker 1994). Part of this excess energy can be released through magnetic reconnection (Steiner 2005b).

1.6 Overview of the thesis

In this thesis, we focus on the magnetic flux concentrations in the quiet Sun. To this end, we observed magnetic elements, bright points, and magnetic network far from active regions. Spectropolarimetric observations of the neutral iron lines at 630 nm and the Ca II H intensity line profile are the main ingredients we have used. Inversion and synthesis of the Stokes spectra were utilized using the SIR code to infer information about the atmospheric parameters. Since SIR cannot handle NLTE problems, a NLTE radiative transfer code was also used to synthesize Ca II H line profiles. Besides this, speckle image reconstruction were performed to study the temporal evolution of the magnetic elements. The body of this thesis is presented in the next two chapters and organized as follows:

Chapter 2 : the small-scale photospheric magnetic structures,

Chapter 3 : the emission of the chromosphere and its temperature stratification.

In Chapter 2, magnetic properties of the network and inter-network are presented. Magnetic flux density, magnetic field strength, and the filling factors were derived from

the inversion of Stokes profiles (Rezaei et al. 2006b, 2007a). We tried to clarify whether the dominant magnetic field strength of the inter-network is about kilogauss or a few hundred Gauss. This was one of the first studies in which inversion of inter-network Stokes profiles of visible lines led to weak magnetic field strengths, far before the launch of the Hinode mission (**Sect. 2.1**).

An opposite polarity (OP) Stokes-V profile is a set of two Stokes-V profiles of two different spectral lines, recorded in a strictly co-temporal and co-spatial observation that shows opposite polarities for the two lines. Sánchez Almeida et al. (2003a) report such profiles but this work was later questioned by Khomenko et al. (2005b), who showed that different seeing[8] conditions for the two data sets can spuriously produce OP profiles. Rezaei et al. (2007c) presented co-temporal and co-spatial Stokes-V profiles of the Fe I 630 nm line pair, where the two lines show opposite polarities in a *single spectrum*. We computed synthetic line profiles and reproduced these spectra with a two-component model atmosphere: a magnetic and a non-magnetic component. This observation can be understood as a magnetic reconnection event in the solar photosphere (**Sect. 2.2**). Later on, we provide independent evidence for photospheric reconnection at the site of this observation (Sect. 2.4).

The areas of the two lobes of Stokes-V profiles are identical when formed in a static atmosphere but become asymmetric in the presence of gradients in velocity and magnetic field strength (Illing et al. 1975). Hence, the variation in Stokes-V area asymmetry across magnetic elements bears information on their magnetic field and plasma flow properties. Observations had shown a positive area asymmetry in and around magnetic elements (Sigwarth et al. 1999a). Theoretical models predicted a canopy-like magnetopause in which the central part and the surrounding have negative and positive area symmetries, respectively (Steiner et al. 1998). This prediction has been confirmed by Rezaei et al. (2007d,e) for the first time. Using the empirical rule of Solanki & Pahlke (1988), we were able to discriminate between different regimes of the magnetic and flow fields. Hence, we provided strong evidence for the existence of current sheets at the boundary of magnetic elements, where a magnetopause separates a field-free volume from a magnetic structure (Ampère's law). In this work, we compared Hinode spectro-polarimetric data with synthetic profiles of a 3 D magnetohydrodymanics (MHD) simulation (**Sect. 2.3**).

Polarimetric observations have so far provided only limited information on the evolution of individual magnetic elements (Sect. 1.5). Rezaei et al. (2007b) studied the structure and evolution of the magnetic field of the quiet Sun by investigating weak spectropolarimetric signals. To this end, a quiet region close to the disk center was observed. There are two examples of magnetic flux cancellation of small-scale opposite-polarity patches, followed by an enhanced chromospheric emission. In each case, the two opposite-polarity patches gradually became smaller and, within a few minutes, the smaller one completely disappeared. We provide evidence for a cancellation scenario in the photosphere which leaves minor traces at the chromospheric level (**Sect. 2.4**).

[8]Seeing is the degradation of the image quality (blurring, image motion, and image distortion) by fluctuations of the refractive index of the Earth's atmosphere in the light path (Stix 2004).

As explained above, a large fraction of Stokes-V profiles is found to be asymmetric, especially in the inter-network area. An extreme case of this asymmetry is when one lobe is absent. These single-lobe Stokes-V profiles challenged theoretical models of the solar atmosphere. Rezaei et al. (2008b) presented a statistical analysis of some six million profiles and looked for single-lobe profiles. We found that the fraction of single-lobe profiles in the Hinode data is much larger than in ground-based observations. Separating blue-lobe-only from red-lobe-only profiles, we discriminated between different formation scenarios. We found that blue-lobe-only profiles show brighter continuum and line-core intensity in Fe I 630 nm line pair, unlike red-only profiles. Blue-lobe-only profiles also show blue-shifted line-cores which is not the case for red-only profiles. In other words, blue-lobe-only profiles are observed inside granular upflows. Our findings are consistent with one of the mechanisms proposed by Steiner (2000) (**Sect. 2.5**).

In Chapter 3, we present the thermal structure of the chromosphere. Rezaei et al. (2007a) observed the Stokes parameters of the photospheric iron line pair at 630 nm and the intensity profile of the chromospheric Ca II H line at 396.8 nm in a quiet Sun region at a heliocentric angle of 53°. Various line parameters were deduced from the Ca II H line profile. The photospheric magnetic field vector was reconstructed from an inversion of the measured Stokes profiles. A statistical analysis of network and inter-network properties was performed. The H-index is the integrated emission in a 0.1 nm band around the Ca core. We separated a magnetically, H_{mag}, and a non-magnetically, H_{non}, heated component from a non-heated component, H_{re}, in the H-index. Considering the effect of straylight, the contribution from an atmosphere without temperature rise above the photosphere to the H-index ($H_{co} \approx 6$ pm) is about half of the observed H-index in the inter-network (**Sect. 3.1**).

Rezaei et al. (2008a) challenged static chromospheric model atmospheres with observations of the reversal-free calcium profiles: profiles that do not show a measurable emission peak in the H_{2v} and H_{2r} wavelength bands. In this study, more than 10^5 line profiles from inter-network regions were analyzed. For comparison with the observed profiles we synthesized spectra for a variety of model atmospheres with a NLTE radiative transfer code. A quarter of the observed Ca II H line profiles was found to be reversal-free. All of the chosen model atmospheres with a temperature rise fail to reproduce such profiles. On the other hand, the synthetic calcium profile of a model atmosphere that has a monotonic decline of the temperature with height shows a reversal-free profile that has much lower intensities than any observed line profile. The observed reversal-free profiles indicate the existence of cool patches in the interior of chromospheric network cells, at least for short time intervals (**Sect. 3.2**).

Chapter 2

The small-scale photospheric magnetic structures

In this chapter, we studied the structure of magnetic elements in the solar photosphere from different points of views: statistical analysis, case study, temporal evolution, and comparison of observations with three dimensional MHD simulations. The data sets which have been used here were recorded at the German Vacuum Tower Telescope (VTT) and Hinode satellite observatory. In all cases, results of the observed quantities were compared with theoretical models and other observational interpretations. To this end, profile synthesis and inversion of the observed profiles have been performed.

2.1 The magnetic field strength in the solar inter-network

As explained in Sect. 1.1.1, the dominant pattern covering the entire solar surface, except sunspots, is granulation, with a spatial scale of 1-2 Mm. On a larger scale, supergranules show the same pattern. Boundaries of supergranules host the chromospheric network. Observations showed that the inter-network (network cell interior) has much less magnetic field than the network (Keller et al. 1994; Lites 2002).

Traditional magnetic field strength distributions for the quiet Sun inter-network based on visible lines have a broad peak centered around 1 kG (Sánchez Almeida et al. 2003a; Domínguez Cerdeña et al. 2006). On the other hand, observations in the infrared lines show a clear peak at lower field strengths and an almost exponentially decreasing probability for higher field strengths (Collados 2001; Bellot Rubio & Collados 2003; Khomenko et al. 2003). This discrepancy between the retrieved parameters from the visible and infrared lines has not been solved so far (Steiner 2003b; Martínez González et al. 2006). We investigated the magnetic field strength distribution of the inter-network to check whether it consists of weak fields (e.g., Faurobert et al. 2001; Collados 2001) or kilogauss fields (e.g., Sánchez Almeida et al. 2003a,b).

Table 2.1: Properties of spectral lines in POLIS red channel (Beck et al. 2005c). Δh indicates the approximate formation height of the line core.

Spectral line	λ (nm)	Transition ($^{2S+1}L_J$)	g_{eff}	Δh (km)
Fe I	630.151	$^5P_2 - ^5D_2$	1.67	300 – 500
Fe I	630.250	$^5P_1 - ^5D_0$	2.50	200 – 460
Telluric absorption lines				
O_2	630.200	–	–	–
O_2	630.276	–	–	–

2.1.1 Observations and data reduction

We observed a network area close to the active region NOAA 10675 on September 27, 2004, with the POLIS instrument at the German VTT in Tenerife. POLIS was designed to provide co-temporal and co-spatial measurements of the magnetic field in the photosphere and the Ca II H intensity profile (Schmidt et al. 2003; Beck et al. 2005b). It records simultaneously a spectral band about 630.2 nm (red channel, Table 2.1) and another spectral band about 396.8 nm (blue channel, Table 2.2). Both channels have the capability to record full-Stokes spectropolarimetric data. In practice, however, the light level in the blue channel is so low that with an integration time of about 5 s, there is no clear signal in polarimetric mode of the blue channel. Hence, it only records the intensity profile.

Table 2.2: Solar spectral lines in the calcium channel of POLIS (Beck et al. 2005c).

Spectral line	λ (nm)	Transition ($^{2S+1}L_J$)	g_{eff}	Δh (km)
Fe I	396.452	$^3P_1 - ^5P_2$	2.0	110 – 320
Fe I	396.551	$^5D_3 - ^5D_4$		
Fe I	396.607	$^3F_2 - ^3D_3$	2.0	350 – 520
Fe I	396.665	$^5D_0 - ^5F_1$		370
Fe I	396.681	$^3D_2 - ^5F_1$		250
Fe I	396.745	$^3H_4 - ^1G_3$	0.75	270 – 450
Fe I	396.792	$^5D_3 - ^3G_4$	1.0	280 – 510
Ca II H	396.849	$^2S_{0.5} - ^2P_{0.5}$	1.33	1000
Fe I	396.918	$^3F_4 - ^3F_3$	1.50	510 – 630
Fe I	396.963	$^3D_3 - ^3H_4$		

The observations were part of a coordinated observation campaign in the International Time Program, where also the Swedish Solar Telescope (SST), Dutch Open Telescope (DOT) and the Télescope Héliographique pour l'Étude du Magnétisme et des Instabilités Solaires (THÉMIS) participated. Here we analyzed a series of thirteen maps of the same

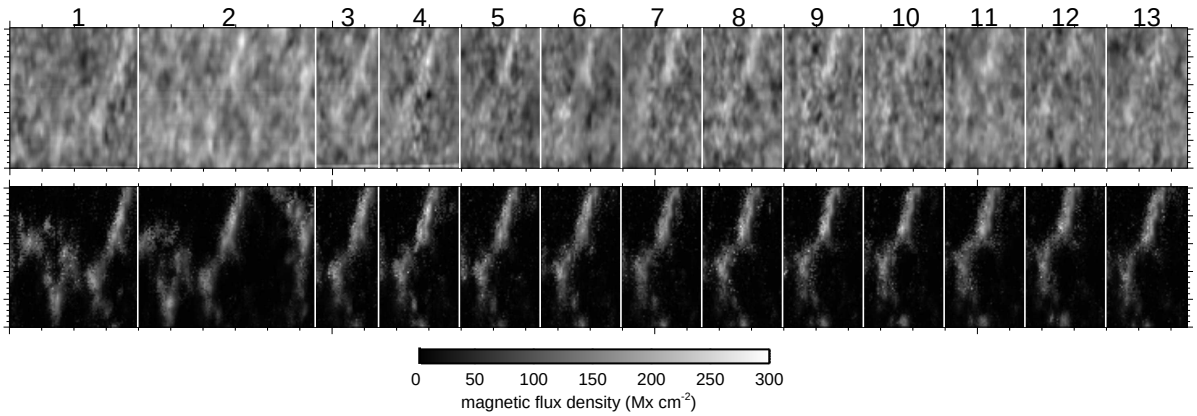

Figure 2.1: *Top:* the continuum intensity at 630 nm. *Bottom:* the magnetic flux density obtained from the inversion. Each small tickmark in x (y) direction is 10 (1) arcsec. Note that sampling in x and y directions are different.

network region at a heliocentric angle of 53°, taken during several hours. We achieved a spatial resolution of around 1 arcsec, estimated from the spatial power spectrum of the intensity maps. All maps were recorded with a slit width of 0.5 arcsec, a slit height of 47.5 arcsec, and an exposure time per slit position of 4.92 s. The scan extension for the first three maps was 40.5, 55.5, and 20.5 arcsec, while it was 25.5 arcsec for the remaining ten maps.

The Ca II H line and the visible neutral iron lines at 630.15 nm, 630.25 nm were observed with the blue and red channels of POLIS. The spatial sampling along the slit (y-axis in Fig. 2.1) was 0.29 arcsec. The scanning step was 0.5 arcsec for all maps. The spectral sampling of 1.92 pm for the blue channel and 1.49 pm for the red channel led to a velocity dispersion of 1.45 and 0.7 $\mathrm{km\,s^{-1}}$ per pixel, respectively. The spectropolarimetric data of the red channel were corrected for instrumental effects and telescope polarization with the procedures described by Beck et al. (2005b,c). Figure 2.1 displays an overview of the thirteen maps after spatial alignment. The top map shows the Fe I 630 nm continuum intensity normalized to the average quiet Sun intensity. The bottom map shows the magnetic flux density obtained from the spectropolarimetric data. Here, we discuss characteristic parameters of the Fe I 630 nm line pair and briefly explain the inversion method that was used to infer the vector magnetic field.

Definition of network and inter-network For each map, we created a mask to distinguish between the network and inter-network regions. This was done manually on the basis of the magnetic flux (and the H-index, see Chapter 3).

Analysis of Fe I 630 nm line profiles

The data of the red channel of POLIS were treated with the standard polarimetric calibration procedures described in Beck et al. (2005b,c). The spectral line curvature was

removed using the telluric O_2 line at 630.20 nm (Table 2.1) with a routine described in Rezaei et al. (2006a). The polarization signal in $Q(\lambda)$, $U(\lambda)$, and $V(\lambda)$ was normalized to the local continuum intensity, I_c, for each pixel. The RMS noise level of the Stokes parameters in the continuum was $\sigma = 8.0 \times 10^{-4} I_c$. Only pixels with Stokes-V signals greater than $3\,\sigma$ were included in the profile analysis. For regular Stokes-V signals above the threshold, we derived positions and amplitudes of the profile extrema in all Stokes parameters by fitting a parabola to each lobe. The amplitude and area asymmetry are two well-defined parameters for a Stokes-V profile which provide information about the gradients in the magnetic field strength and velocity along the LOS (Illing et al. 1975; Solanki & Pahlke 1988). Figure 2.2 shows the definition of parameters for the asymmetries. The amplitude asymmetry is given by (Solanki & Stenflo 1984; Martinez Pillet et al. 1997):

$$\delta a = \frac{a_\mathrm{b} - a_\mathrm{r}}{a_\mathrm{b} + a_\mathrm{r}}. \tag{2.1}$$

Similarly, the area asymmetry is defined as

$$\delta A = \frac{A_\mathrm{b} - A_\mathrm{r}}{A_\mathrm{b} + A_\mathrm{r}}. \tag{2.2}$$

The polarity of an antisymmetric Stokes-V profile is the sign of its blue-lobe. For example in Fig. 2.2, the polarity is negative.

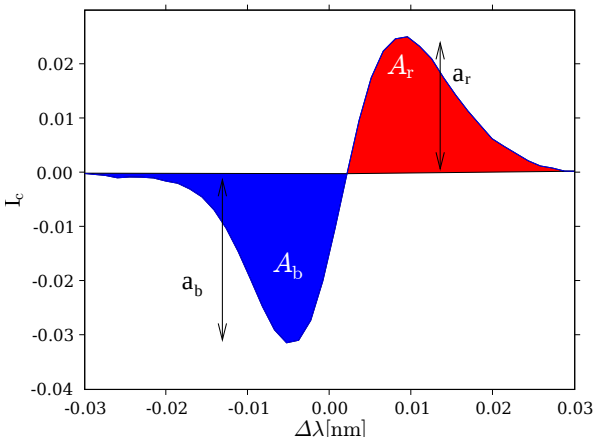

Figure 2.2: Parameters of a Stokes-V profile: amplitudes $(a_\mathrm{b}, a_\mathrm{r})$ and areas $(A_\mathrm{b}, A_\mathrm{r})$ of each lobe are indicated. The definitions of the asymmetries are given in Eqs. 2.1 and 2.2, respectively.

An inversion was performed using the SIR code (Ruiz Cobo & del Toro Iniesta 1992). We used the same setup as in Bellot Rubio & Beck (2005) and Beck et al. (2007): a two-component solar atmosphere model with one magnetic and one field-free component. Additionally, a variable amount of straylight was allowed for. This inversion setup accounts for unresolved magnetic fields inside each pixel. We did not consider any gradient for the atmospheric parameters except for the temperature. The inversion yields the magnetic field vector and an estimate for the magnetic filling fraction. The flux density map (magnetic flux per pixel, bottom panel in Fig. 2.1) is based on the inversion results.

2.1.2 Histograms of the magnetic field parameters

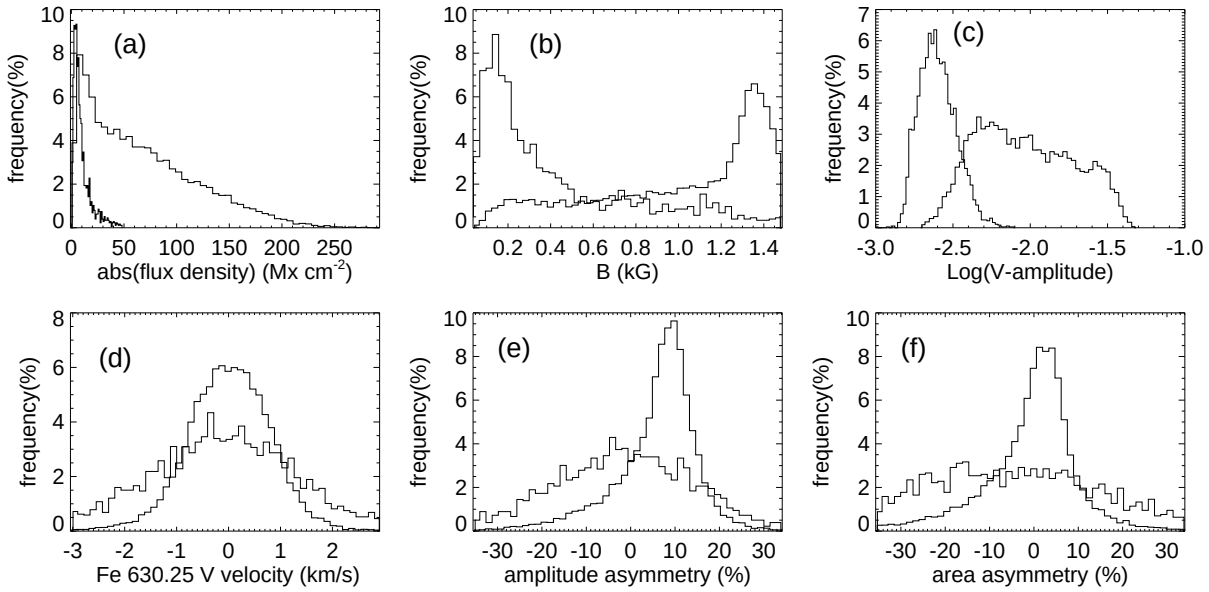

Figure 2.3: Histograms of the magnetic field parameters for the network (thick) and inter-network (thin): *a)* the absolute magnetic flux density, *b)* the field strength, *c)* Stokes-V amplitude, *d)* Fe I 630.25 nm V velocity, *e)* the amplitude asymmetry, and *f)* the area asymmetry.

From the inversion, we obtain the magnetic field strength and the magnetic flux in the photosphere. The statistics of these quantities in the network and inter-network are discussed here; the relation with the chromospheric parameters is discussed in the next chapter. We restricted the analysis to those profiles with a regular Stokes-V and a double emission calcium profile, although there are only 1712 profiles in the inter-network. The histogram of the absolute magnetic flux density, $\Phi = f\,\mathbf{B}\cos\alpha$, is shown in the top-left panel of Fig. 2.3a, where f is the magnetic filling factor, $\mathbf{B}$ is the field strength, and α is the angle between the magnetic field orientation and the LOS. The histogram for the inter-network has a narrow distribution, which peaks at $\sim 4\,\mathrm{Mx\,cm^{-2}}$ whereas there is a long tail up to $\sim 250\,\mathrm{Mx\,cm^{-2}}$ for the network. The distribution function of the magnetic field strength (Fig. 2.3b) has a peak around $\sim 1.3\,\mathrm{kG}$ for the network elements and increases with decreasing field strength for the inter-network. The peak at 200 G is due to the detection limit of the polarization signal (see Sect. 2.1.4). The histogram of the Stokes-V amplitude (Fig. 2.3c) shows weak inter-network signals with a Stokes-V amplitude far less than $1\%\,I_c$. The distribution of the inter-network V amplitude[1] peaks at $\sim\ 2\ \times\ 10^{-3}\,I_c$ whereas the network shows a broad distribution up to $\sim\ 0.03\,I_c$.

The Stokes-V velocity, also known as zero-crossing velocity, is defined as the relative

[1]The histogram of the Stokes-V amplitude of the inter-network (Fig. 2.3c) includes all data points with a clear Stokes-V signal.

shift between the zero-crossing wavelength of the profile (Fig. 2.2) and the solar rest wavelength of the Stokes-I profile. The distribution of the Stokes-V velocities is shown in Fig. 2.3d. Although it has a peak around zero both for the network and inter-network, the inter-network shows a larger fraction of high-velocity V profiles. The amplitude and area asymmetries (Eqs. 2.1 and 2.2) in the network peak at small positive values of 10 % and 3 %, respectively (Fig. 2.3e and f). In contrast, there is no tendency to positive or negative values for the inter-network asymmetries. This is in agreement with previous studies of the quiet Sun magnetic fields (Sigwarth et al. 1999a; Sigwarth 2001; Khomenko et al. 2003). There are models, e.g., by Solanki & Pahlke (1988), to explain why we see mostly a positive area asymmetry in network. We compare this model with observations and discuss the results in Sect. 2.3.

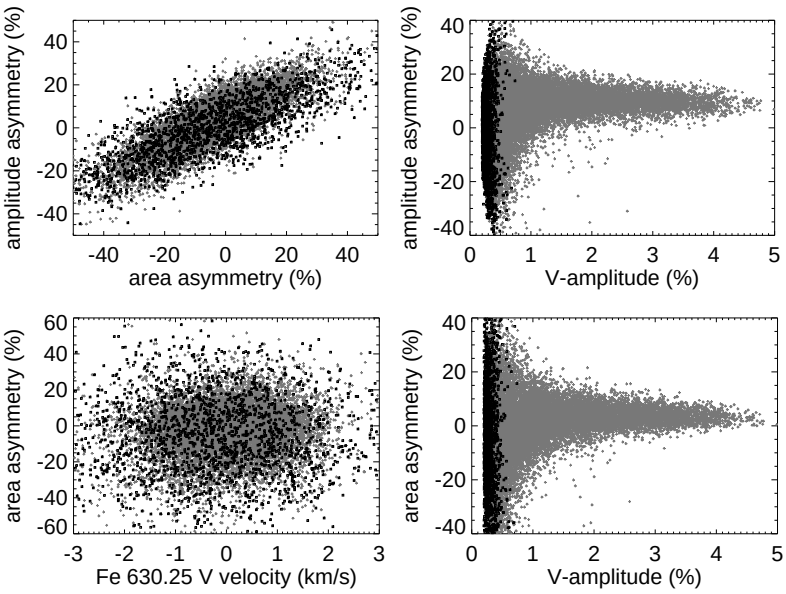

Figure 2.4: *Top left*: scatter plot of the amplitude vs. area asymmetries. *Bottom left*: scatter plot of the area asymmetry vs. the Stokes-V velocity. *Right panels*: scatter plots of the amplitude and area asymmetries vs. the Fe I 630.25 nm Stokes-V amplitude. Gray and black show the network and inter-network, respectively.

2.1.3 Correlations between photospheric quantities

There is a strong correlation between the amplitude and area asymmetries, both in the network and inter-network (Fig. 2.4, top left panel). In contrast, there is no correlation between either amplitude or area asymmetries and the Stokes-V velocity (bottom left panel, Fig. 2.4). In other words, the sign of the amplitude or area asymmetry does not depend on the sign of the Stokes-V velocity. These are typical properties of the quiet Sun magnetic field as reported by Grossmann-Doerth et al. (1996a), Sigwarth et al. (1999a), and Khomenko et al. (2003). The right panels of Fig. 2.4 show scatter plots of the Stokes-V asymmetries versus V amplitude. There is a tendency for high amplitude Stokes-V signals to have small asymmetries. As suggested by Sigwarth (2000), this is partly due to the dynamic nature of the inter-network magnetic structures and partly due to worse signal-to-noise ratio in comparison to network profiles. On the other hand, histograms

of the asymmetries peak at a positive value. Implications of these two findings will be discussed in Sect. 3.1.

2.1.4 The magnetic field strength distribution

We measured a magnetic field distribution for the inter-network using the Fe I 630 nm pair that is similar to the magnetic field distribution from fully split infrared lines (Fig. 2.3b). We elaborated on the effects of spatial resolution and signal-to-noise ratio on this finding. We used the Kiepenheuer Adaptive Optics System (KAOS) to improve spatial resolution and image stability (von der Lühe et al. 2003). It provided stable sharp images in a certain field of view, and therefore allowed us to increase the exposure time to have better signal-to-noise ratio.

Figure 2.5 is a close-up view of the inter-network magnetic flux distribution. The lowest flux detected is $\sim 0.05\,\mathrm{Mx\,cm^{-2}}$. The distribution of the flux decreases sharply for fluxes below $\Phi \leq 4\,\mathrm{Mx\,cm^{-2}}$, which is due to the detection limit of the polarization signal. The small fluxes still detected give us, however, confidence that the magnetic field strength distribution of Fig. 2.3b is reliable as a consequence of the combination of high spatial resolution and good signal-to-noise ratio.

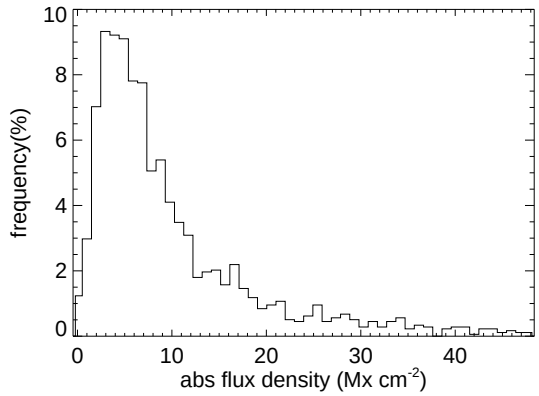

Figure 2.5: Close up view of the flux density distribution for the inter-network. At a value of $\sim 4.0\,\mathrm{Mx\,cm^{-2}}$, the histogram shows a peak. Statistics of the inter-network sample was 1712 profiles.

To investigate the influence of noise, we compared inversion results of the original data sets with and without adding noise. For all these noisy data sets, the RMS noise value was increased to $\sigma = 15.0 \times 10^{-4}\, I_c$, two times larger than the original RMS noise level. The spatial sampling was identical to the original data. We emphasize that the inversion was performed with exactly the same assumptions and initial model atmosphere. Figure 2.6 compares two sets of full Stokes profiles (black) and the inversion fit (red). The left four panels are the original profiles and the right four panels are the same profiles with noise. The fit quality is satisfactory in both cases but the retrieved model atmospheres differ significantly. Especially important is the fact that the *noisy* inversion leads to a stronger field of 1.5 kG.

To compare the field strength obtained from the original and noisy data sets, their histograms are shown in Fig. 2.7. The distribution of the original field strength peaks at

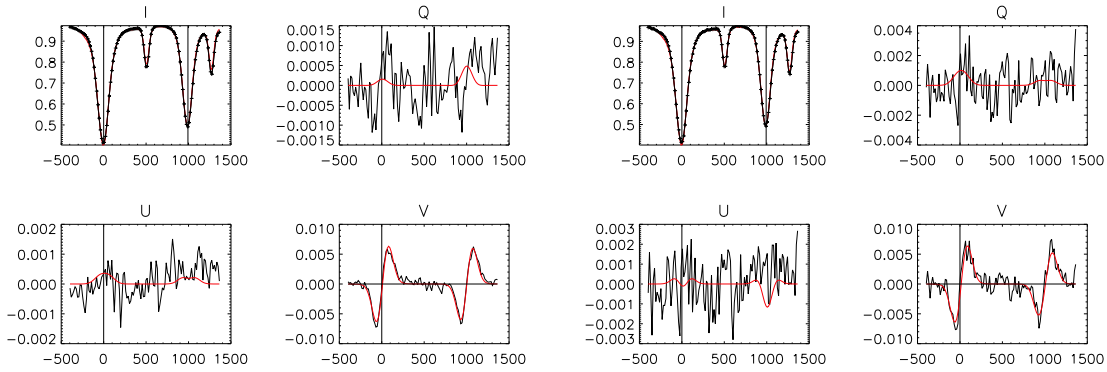

Figure 2.6: The left four plots show the original Stokes profiles (black) and the inversion fits (red). The right four figures show the same profile with a RMS noise value two times larger and corresponding fits. The magnetic field strength, magnetic filling factor, macro turbulence velocity and the inclination for the original and noisy profiles are (842, 1543) G, (7.6, 5.3)%, (2.95, 2.77) $\mathrm{km\,s^{-1}}$, and (161, 153) degree respectively. The x-axis shows the spectral pixels in mÅ. The y-axis shows the normalized intensity in I_c.

around $\sim 200\,\mathrm{G}$ (black histogram), while for the noisy data, it has a clear shift toward higher values with a peak at 0.8 kG (red histogram). This emphasizes the role of the noise in the existing discrepancy between visible and infrared measurements (Bellot Rubio & Collados 2003).

In brief, we find that high spatial resolution of these observations along with low noise data is one step toward resolving disagreements between the visible and infrared polarimetric measurements. The visible Fe I 630 nm pair shows higher Stokes amplitudes for small magnetic fields than the (fully split) infrared lines, like Fe I 1.56 μm (Stix 2004). Hence, with an equal amount of noise in observational data, the visible lines provide higher signal-to-noise than infrared lines. Therefore, in contrast to Martínez González et al. (2006) and López Ariste et al. (2007), we find the visible Fe I 630 nm pair to be a proper tool to investigate the inter-network magnetic field. We ascribe the present disagreements to the low spatial resolution of observations and different signal-to-noise ratios. This was confirmed later by Hinode spectropolarimetric observations of Orozco Suárez et al. (2007, 2008).

Conclusion: We obtain distributions of the field strength for network and inter-network regions. For the inter-network fields, for the first time an inversion of visible spectral lines in the weak field limit led to the same distribution as results from the more sensitive infrared lines (Collados 2001). Thus, we find that the inter-network magnetic field is dominated by field strengths of the weak field regime which ranges up to some 600 G. This rules out the argument that the inter-network is dominated by a magnetic field with a strength of more than a kilogauss (e.g., Sánchez Almeida et al. 2003a). In other words, we find a magnetic field strength distribution in the inter-network using visible lines which is similar to results inferred from infrared lines with larger Zeeman splitting.

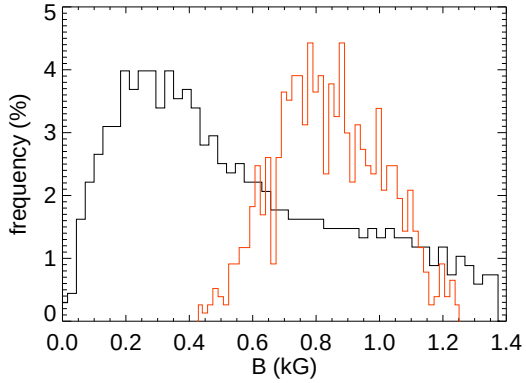

Figure 2.7: Histograms of the inter-network field strengths of one of the maps based on the inversion of original data (black) and noisy data (red). The noisy data had an RMS noise level of $\sigma = 15.0 \times 10^{-4}\, I_c$, two times larger than the original data.

The distribution function increases with decreasing field strength. The peak at 200 G is due to the detection limit of the polarization signal. The average and distribution peak of the absolute flux density (of magnetic profiles) in the inter-network are ~ 11 and 4 Mx cm^{-2}, respectively. The observed absolute magnetic flux density with the Hinode data confirm our results (Lites et al. 2008). We conclude that the combination of high spatial resolution and polarimetric accuracy is sufficient to reconcile the different results on field strength found from infrared and visible lines. A thorough study of this issue by Orozco Suárez et al. (2007, 2008) confirms this result.

2.2 Opposite magnetic polarity of two photospheric lines in single spectrum

Stokes polarimetry provides detailed information about the magnetic field and its interaction with the plasma in the solar photosphere and chromosphere (Stenflo 1994; Landi degl'Innocenti & Landolfi 2004). While most of the observed Stokes-V profiles in active regions and the network are close to antisymmetric with low degree of asymmetry, abnormal and strongly asymmetric V profiles are common in the inter-network (Sigwarth 2001; Lites 2002). The classification of Sigwarth et al. (1999b) presents abnormal V profiles with a single-lobe, two lobes with identical polarities (two humped), Q-like, or pathological profiles with four or more lobes. There are indications from observations and 3D simulations that the degree of asymmetry and the fraction of abnormal V profiles increase with decreasing magnetic flux (Sigwarth et al. 1999b; Khomenko et al. 2005b). While most of the pathological profiles can be reconstructed with models consisting of two or more magnetic components, Steiner (2000) has shown that one-component models can also account for a large variety of V profiles provided that magnetic, velocity, and temperature gradients are large enough.

An opposite-polarity (OP) Stokes-V profile is a set of two V profiles of two different spectral lines, recorded in a strictly co-temporal and co-spatial observation, that shows

different polarities. Sánchez Almeida et al. (2003a) report opposite-polarity V profiles between the visible (630 nm) and the infrared (1.56 μm) neutral iron lines observed at the French-Italian solar telescope THÉMIS and the German Vacuum Tower Telescope (VTT), respectively. This work was questioned later by Khomenko et al. (2005b), who showed that different seeing conditions for the two data sets can spuriously produce OP profiles.

In this section, we present observations of a quiet Sun region close to the disk center with POLIS that show a few OP Stokes-V profiles. Each set of OP profiles consists of the two neutral iron lines at 630.15 and 630.25 nm that are part of a *single spectrum* recorded strictly simultaneously. The formation heights of these two lines span different layers in the photosphere (Cabrera Solana et al. 2005; Khomenko & Collados 2007, and references therein). We studied one set of these profiles in detail and argue that it hints at a magnetic reconnection event in the solar photosphere.

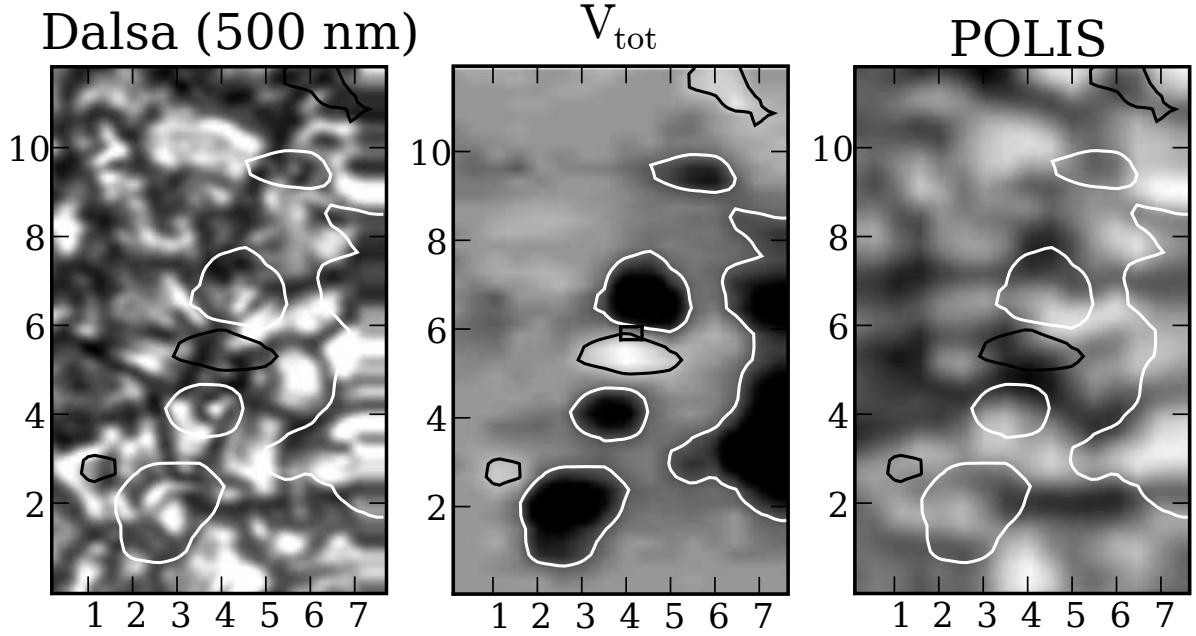

Figure 2.8: Co-spatial and co-temporal data of the speckle reconstructed continuum image at 500 nm (left), $V_{\rm tot}$ map (middle), and Stokes-I continuum map (right). Contours of the $V_{\rm tot}$ map are overplotted on all panels. The position of the opposite-polarity profile is marked with a rectangle in the middle panel, which also shows the POLIS pixel size. The horizontal axis is the scan direction and the vertical is the slit direction. In the $V_{\rm tot}$ map, white and black indicate negative and positive polarities, respectively (for definition of positive/negative polarity, see Fig. 2.9). Tickmarks indicate arcsec.

2.2.1 Observations and data reduction

A sequence of spectra was taken in a quiet Sun region close to the disk center ($\cos\theta = 0.99$), with the VTT in Tenerife, July 07, 2006. The seeing was good and stable during the observation. The KAOS was used for maximum spatial resolution and image stability (von der Lühe et al. 2003). Each of the 40 scans consists of a $8 \times 70\,\mathrm{arcsec}^2$ area. The scanning step size and spatial sampling along the slit were 0.48 and 0.29 arcsec, respectively. The scanning cadence was about 97 s. The slit height of the blue (396.8 nm) and red (630 nm) channels was 70 and 95 arcsec, respectively.

Full Stokes profiles of the neutral iron lines at 630.15 and 630.25 nm and the Stokes-I profile of the Ca II H line were observed strictly simultaneously with POLIS. The average continuum contrast (rms) of the POLIS Stokes-I maps is $\approx$ 3.4 % of I_c. An absolute velocity calibration was performed using the telluric O_2 line at 630.20 nm (Rezaei et al. 2006a). The spectropolarimetric data of the red channel were corrected for instrumental effects and telescope polarization with the procedures described by Beck et al. (2005b,c). The RMS noise level of the Stokes parameters in the continuum is $\sigma = 6.0 \times 10^{-4}\, I_\mathrm{c}$.

Simultaneously, a continuum speckle channel in POLIS recorded a larger field of view at 500 nm. Each speckle burst consists of some 100 frames recorded within about 15 s. A speckle code was used to retrieve atmospheric abberation (seeing) and remove them using a statistical approach (Wöger 2006). The speckle reconstruction was performed using the Kiepenheuer-Institut Speckle Imaging Package (Mikurda & von der Lühe 2006; Wöger 2006). The spatial resolution of the reconstructed image is about 0.3 arcsec (cf. Fig. 2.8, left panel). We used the POLIS intensity map and the reconstructed image to align the data. The continuum speckle image and the POLIS Stokes-I map are shown in the left and right panels of Fig. 2.8, respectively.

We define the signed integral of Stokes-V profile, V_tot, as follows:

$$V_\mathrm{tot} = \frac{\int_{\lambda_\mathrm{b}}^{\lambda_0} V(\lambda)\,\mathrm{d}\,\lambda - \int_{\lambda_0}^{\lambda_\mathrm{r}} V(\lambda)\,\mathrm{d}\,\lambda}{I_\mathrm{c}}, \tag{2.3}$$

where λ_0 is the zero-crossing wavelength of the Stokes-V profile and λ_r and λ_b denote fixed wavelengths in the red and blue continuum of the lines (Lites et al. 1999, 2008). The dimension of V_tot is wavelength, like the equivalent width (Shu 1981). The middle panel of Fig. 2.8 shows the V_tot map in which the position of the OP profile is marked with a rectangle that also shows the POLIS pixel size. It is located between two patches of opposite polarities. The OP profile (exposure time 5 s) was recorded within the time window of 15 s used for the speckle burst (left panel, Fig. 2.8). This image and the continuum map (right panel, Fig. 2.8) indicate that the lower patch was co-spatial with an intergranular vertex (white patch in the V_tot map). Therefore, the V profiles in the lower patch show a redshift, which is also the case for the 630.25 nm OP profile.

Figure 2.9 shows the OP profile. The positive (negative) magnetic polarity in this figure corresponds to black (white) color in the V_tot map. Both lines have positive amplitude and area asymmetries. The 630.15 nm line of the OP profile has a blueshifted zero-crossing of $v_\mathrm{zc} \approx -1\,\mathrm{km\,s^{-1}}$, while the 630.25 nm line has a redshifted zero-crossing of $v_\mathrm{zc} \approx +2\,\mathrm{km\,s^{-1}}$.

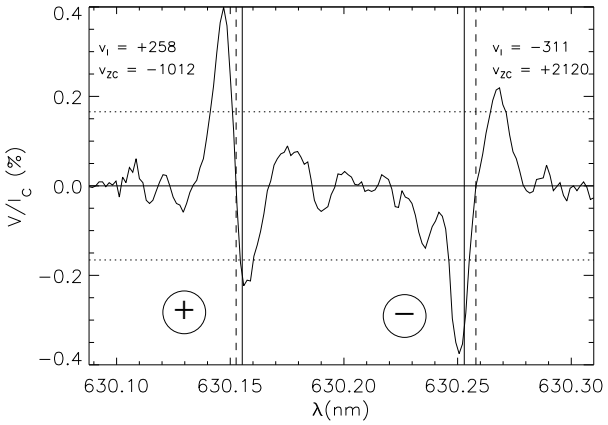

Figure 2.9: Stokes-V line pair that shows opposite polarity in the 630.15 and 630.25 nm lines. The position of the Stokes-I line core and the Stokes-V zero-crossing are indicated by vertical solid and dashed lines, respectively. The line-core (v_I) and zero-crossing (v_{zc}) velocities are in $m\,s^{-1}$.

The OP profile along with its neighboring profiles are shown in Fig. 2.10. In this figure, the slit direction is vertical and the OP profile is at the center. The Stokes-V profiles above and below the OP profile show strong V signals of normal shape which shows that the OP profile was located at the center of a polarity reversal. The polarity of the 630.25 nm line of the OP profile is the same as that of the lower pixels and the polarity of the 630.15 nm line is identical to that of the upper ones. The V profile left to the OP profile (Fig. 2.10, second row, left) is also strange: a pathological profile for the 630.15 nm line and a regular profile of the 630.25 nm line with a polarity similar to the 630.25 nm line in the OP profile. The same is true for one scan-step after the OP profile (Fig. 2.10, second row, right column): a normal V profile at 630.15 nm with a polarity identical to the 630.15 nm line of the OP profile and no signal for the 630.25 nm line.

Note that the OP profile cannot be produced by seeing effects that mix spectra from neighboring spatial locations. The adjacent profiles above and below of the central OP profile in Fig. 2.10 have incompatible shifts, line widths and amplitudes: A least-squares fit to a superposition of the adjacent upper and lower profiles yielded residuals exceeding 2σ. Independently, we measured from the speckle burst that the standard deviation of the image motion during the exposure was only about 0.1 arcsec. Therefore, the OP profile was not due to seeing effects.

2.2.2 The model profile

The basic properties of the observed OP profile are: (i) the opposite polarities of the V profiles at 630.15 nm and 630.25 nm, (ii) the velocity of the deeper forming line (630.25 nm) is positive (downward) and the velocity of the higher forming line (630.15 nm) is negative (upward), and (iii) both lines show positive area and amplitude asymmetries. The vicinity of the OP profile is characterized by two patches of opposite polarity that are separated by only one resolution element as indicated by the rectangle in the middle panel of Fig. 2.8 and in the profile array of Fig. 2.10. This configuration suggests that we witness an electric current sheet in the intermediate atmospheric layers with magnetic field

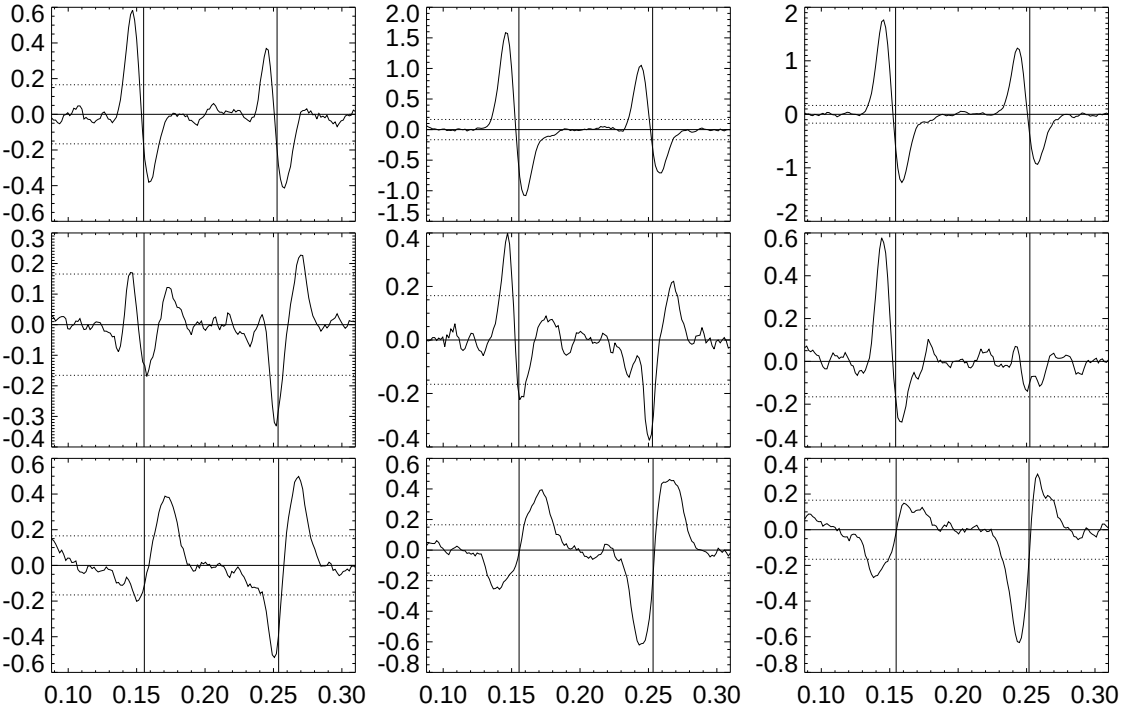

Figure 2.10: The OP Stokes-V profile (center) and its surrounding profiles. Abscissae show the wavelength ($\lambda - 630\,\mathrm{nm}$). The slit direction is vertical. Other parameters are like in Fig. 2.9.

of one polarity in deeper layers and of the opposite polarity in higher layers. The field lines should be inclined w.r.t. the LOS since there is a U signal in the observed Stokes parameters (Fig. 2.12). The finding of upward velocity in the higher layer and downward velocity in the deeper layer presents evidence for magnetic reconnection[2], since such an event produces a bipolar jet. In the central region in-between the two magnetic polarities one expects an enhanced temperature due to Joule heating (gray scale, Fig 2.11). This basic picture is sketched in the left panel of Fig. 2.11. Based on these ideas, we construct in the following a quantitative model which allows us to compute a set of synthetic Stokes profiles for a direct comparison with the observed OP profile.

We used the SIR code (Ruiz Cobo & del Toro Iniesta 1992; Bellot Rubio 2003) to synthesize the Stokes profiles of the Fe I 630 nm pair. In order to fit the degree of polarization and to account for straylight, the model atmosphere had to contain a field free (non-magnetic) component beside the magnetic component. The non-magnetic component was taken to be the HSRA model atmosphere (Gingerich et al. 1971). This thermal stratification was also used for the magnetic component with a slight modification: in an intermediate layer around $\log \tau_{500\,\mathrm{nm}} \approx -1.2$, we introduced a temperature bulge. At the peak of this hot bulge, it was 270 K hotter than in the HSRA atmosphere. The hot bulge was partly field free and partly overlapped with the magnetic field of the deeper

[2]Magnetic reconnection is a process by which magnetic energy is converted into plasma kinetic energy due to rearrangement of the field lines (see Sect. 2.4.2).

layer. Above and below this hot bulge, the velocity and magnetic field have opposite orientations. The ranges of non vanishing magnetic field strength and velocity overlapped, but did not have their peak values at the same optical depth. Constant values for the inclination of the magnetic field w.r.t. the vertical (35°) and the azimuth (135°) were used to fit the ratios between Q, U, and V. The model atmosphere that was finally used to reproduce the OP profile is shown in Fig. 2.11 (right). All structure elements of this model atmosphere were necessary ingredients for a successful reproduction of the OP profile. In particular, the temperature bump was essential to reproduce the different Stokes-V profile polarities when using only one LOS along which two magnetic polarities were present. This demonstrated that OP profiles could be synthesized with a realistic model, but note that this solution may not be unique.

To obtain the filling factor of the magnetic atmosphere, we performed an inversion of the regular Stokes profiles in the surrounding pixels of the OP profile. The inversion set up was similar to that of Bellot Rubio & Beck (2005), except that we assumed a constant value for the stray light and allowed for a linear gradient of the LOS velocity in the magnetic component. From these inversions we obtained magnetic filling factors of 10 – 30 %, so we assumed a filling factor of 20 % for our model atmosphere.

The upper layer of magnetic field along with the bump of negative velocity led to a very asymmetric V profile for both lines. This profile had the polarity of the 630.15 nm line of the OP profile and showed a higher amplitude in 630.15 nm than in 630.25 nm. The lower-layer magnetic field of opposite polarity produced an almost antisymmetric V profile at 630.25 nm but the profile at 630.15 nm was asymmetric. The combination of these two components gave the final fit to the data that is shown in Fig. 2.12. The quality of the fit is satisfactory considering that we only used a single LOS for this complex topology. With a slight shift of the velocity peaks we were also able to reproduce the pathological profile to the left to the OP profile (Fig. 2.10).

2.2.3 Evidence for a photospheric magnetic reconnection

The magnetic area with polarity rendered in dark in the $V_{\rm tot}$ map of Fig. 2.8 was present throughout the observing time of 64 minutes and was persistently bright in Ca II H, which suggests that it belonged to network magnetic fields (see the left column of Fig. 2.19). Different from that, the opposite polarity, white patch, visible in the center of the $V_{\rm tot}$ map, was a transient feature – it assembled from diffuse flux of white polarity, concentrated and intensified to the white patch seen in Fig. 2.8, before it rapidly weakened. Within the scanning cadence of 97 s it virtually disappeared, not without influencing the opposite polarity (black) neighboring patches to the upper and lower sides, which weakened during this time. Such events must frequently take place considering that the magnetic flux in the quiet network is permanently replaced by and in interaction with mixed polarity flux (Schrijver et al. 1997). When flux concentrations of opposite polarity collide, flux cancellation and magnetic field reconnection are likely to be involved (Zwaan 1987). At the reconnection site we expect conversion from magnetic to thermal energy and the formation of a bipolar jet (Priest & Forbes 2000): processes that are compatible with

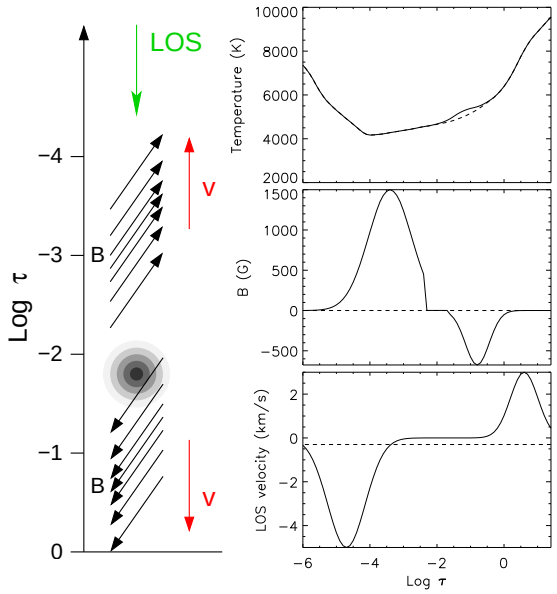

Figure 2.11: *Left*: schematic configuration of the magnetic field, the LOS velocity, and the temperature enhancement (gray scale). *Right*: stratification of the atmosphere as a function of optical depth for the magnetic (solid) and non-magnetic (dashed) components. From top to bottom: temperature, magnetic field strength (with the the sign denoting the polarity), and LOS velocity. The non-magnetic atmosphere has a convective blueshift of $300\,\mathrm{m\,s^{-1}}$.

the temperature bulge in between the two layers of oppositely directed velocities and magnetic fields of the atmosphere of Fig. 2.11 and with the observed flux cancellation and weakening.

For a check of compatibility with the thermal, kinetic, and magnetic energy fluxes required in a reconnection event, we first consider a control volume given by the size of one POLIS pixel of $A_p = \Delta_x \times \Delta_y = 350\,\mathrm{km} \times 210\,\mathrm{km}$ and the height range spanned by the FWHM of the temperature bulge of $h = 135\,\mathrm{km}$, which encompasses a mass of $m = 1.3 \times 10^{12}\,\mathrm{kg}$. With a bulge peak of $\delta T = 270\,\mathrm{K}$ we obtain from Newton's law of cooling[3] a radiative heat loss from this volume of

$$\dot{Q} = 16\,\sigma\,\kappa\,T^3\,\delta T\,m\,f = 9 \times 10^{16}\,\mathrm{W}, \tag{2.4}$$

where σ is the Stefan-Boltzmann constant, $\kappa = 1.1 \times 10^{-2}\,\mathrm{m^2\,kg^{-1}}$ the opacity corresponding to the mean density of $1.3 \times 10^{-4}\,\mathrm{kg\,m^{-3}}$, $T = 5100\,\mathrm{K}$ the corresponding temperature of the unperturbed background atmosphere, and $f = 0.2$ the filling factor. This radiative energy flux should be of the same order of magnitude as the kinetic energy flux,

$$F_{\mathrm{kin}} = (1/2)\,\rho\,v^3\,A_p\,f, \tag{2.5}$$

carried by the bipolar reconnection jets. Using the values of the lower, heavier (downward moving) layer with $v_{\mathrm{LOS}} = 3\,\mathrm{km\,s^{-1}}$ and $\rho = 3.0 \times 10^{-4}\,\mathrm{kg\,m^{-3}}$, and assuming the velocity to be directed parallel to the magnetic field we obtain $F_{\mathrm{kin}} = 1 \times 10^{17}\,\mathrm{W}$. The kinetic energy of the upwards moving jet is negligible, because of the lower density. The kinetic

[3]Newton's law of cooling states that the rate of change of the temperature of an object is proportional to the difference between its own temperature and the ambient temperature (e.g., Kittel 1980).

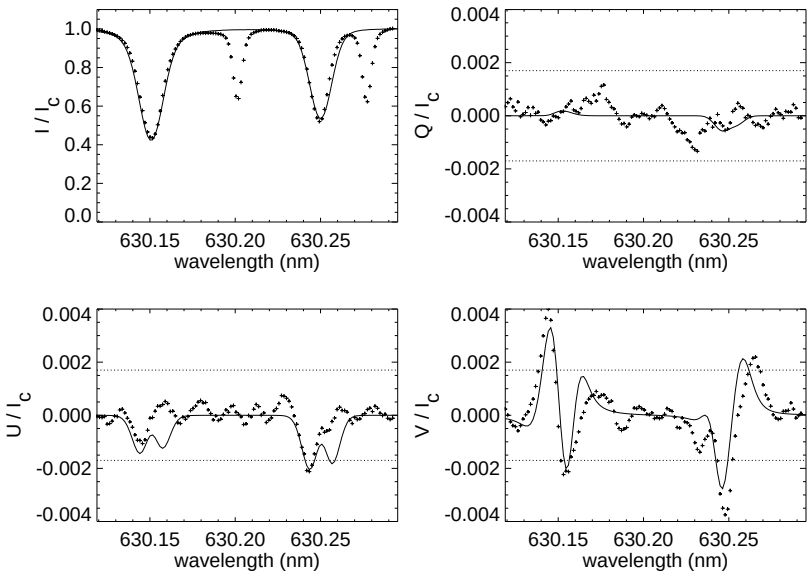

Figure 2.12: Comparison between the observed Stokes profiles (pluses) and the synthesized ones (solid lines). The horizontal dotted lines show the 3σ noise level.

and thermal energy fluxes need to be sustained by a corresponding influx of magnetic energy of

$$F_{\rm mag} = v\,(B^2/2\mu_0)\,\Delta_x\,h\,\sqrt{f}. \tag{2.6}$$

With $B = 0.1\,\mathrm{T}$ we obtain $F_{\rm mag} = 1\times10^{17}\,\mathrm{W}$ if the influx velocity is $1.2\,\mathrm{km\,s^{-1}}$, which is a reasonable value for the horizontal velocity of photospheric magnetic flux concentrations.

Photospheric magnetic reconnection has been previously studied by Litvinenko (1999) and Takeuchi & Shibata (2001). Since we observe a flux intensification prior to flux canceling for the white polarity patch of Fig. 2.8, the scenario of Takeuchi & Shibata (2001) consisting of reconnection induced by convective intensification may apply to this event. We would like to stress that the model presented here is not necessarily unique and that other model atmospheres may also reproduce the data. However, we expect any alternative model to show strong gradients in velocity and magnetic field strength.

Conclusion: We have discovered several sets of opposite-polarity Stokes-V profiles. Each set is a single spectrum of the 630.15 and 630.25 nm neutral iron lines pertaining to a single resolution element. We used a model atmosphere consisting of a non-magnetic and one magnetic component for synthesizing the observed profiles. The magnetic component contains strong gradients along the LOS in the magnetic field strength and the velocity. In particular, the higher and deeper layers have opposite magnetic polarity. In accordance with the observed red- and blue-shifts of the spectral lines, the proposed model atmosphere contains a bipolar flow of material along the LOS and a temperature enhancement in-between. These atmospheric elements provide evidence of magnetic reconnection in the solar photosphere. Our estimated values for the thermal, kinetic, and magnetic energy fluxes are also compatible with a reconnection event.

2.3 Hinode observations reveal boundary layers of magnetic elements

With ever increasing polarimetric sensitivity and spatial resolution, it becomes now clear that even the most quiescent areas on the solar surface harbor ample amounts of magnetic flux. This flux becomes visible in small patches of field concentrations, called magnetic elements for short. While horizontal fields tend to occur near the edge of granules, in this section we focus on fields predominantly oriented in the vertical direction and mainly occurring in the intergranular space (Lites et al. 2008, 2007b). There, magnetic elements are often visible in G-band filtergrams as point-like objects. In more active regions, magnetic elements of extended size appear in the form of 'crinkles', 'ribbon bands', 'flowers', etc. (Berger et al. 2004), which show a sub-structure consisting of a dark central area surrounded by a striation of bright material and further outside by a downdraft of plasma (Langangen et al. 2007). While Doppler measurements of this downdraft are at the limit of spatial resolution with the best ground-based solar telescopes, spectropolarimetric measurements have less spatial resolution due to image degradation by atmospheric seeing during the required long integration times.

Measurements with the spectropolarimeter on board the Hinode satellite have a superior spatial resolution of approximately 0.3 arcsec thanks to excellent pointing capabilities (Shimizu et al. 2007). The data obtained with the instrumentation on-board the satellite have a superior spatial resolution compared to the ground-based data because they are not affected by seeing. Using Hinode data, we show examples of unipolar magnetic elements of the network-cell interiors that possess a distinct sub-structure, which is strikingly manifested in maps of the asymmetry of spectral lines in the circularly polarized light – the Stokes-V area asymmetry.

The areas of the blue and the red lobes of Stokes-V profiles are identical when formed in a static atmosphere, but become asymmetric in the presence of gradients in the velocity and magnetic field strength (Illing et al. 1975; Solanki & Pahlke 1988; Sánchez Almeida et al. 1989; Landolfi & Landi degl'Innocenti 1996). Hence, the variation in the Stokes-V asymmetry across magnetic elements gives information on their magnetic field and plasma flow properties. Since this information is involved, we computed synthetic Stokes-V profiles of magnetic elements that occur in a three-dimensional simulation of magneto-convection and compared their asymmetries with the measured ones in order to understand their origin.

2.3.1 Observation and data reduction

The observations were carried out on 10 March, 2007 with the spectropolarimeter (SP) of the Solar Optical Telescope (SOT) on board of the Hinode space satellite (Kosugi et al. 2007; Tsuneta et al. 2008; Suematsu et al. 2007). The four Stokes profiles of the Fe I 630 nm line pair were recorded in a quiet Sun area close to the disk center. The integration time of 4.8 s led to an RMS noise level in the polarization signal of $\sigma \approx 1.2 \times 10^{-3}\, I_{\rm c}$. The data calibration for the SP was described in Ichimoto et al. (2008) and Tarbell (2006). The

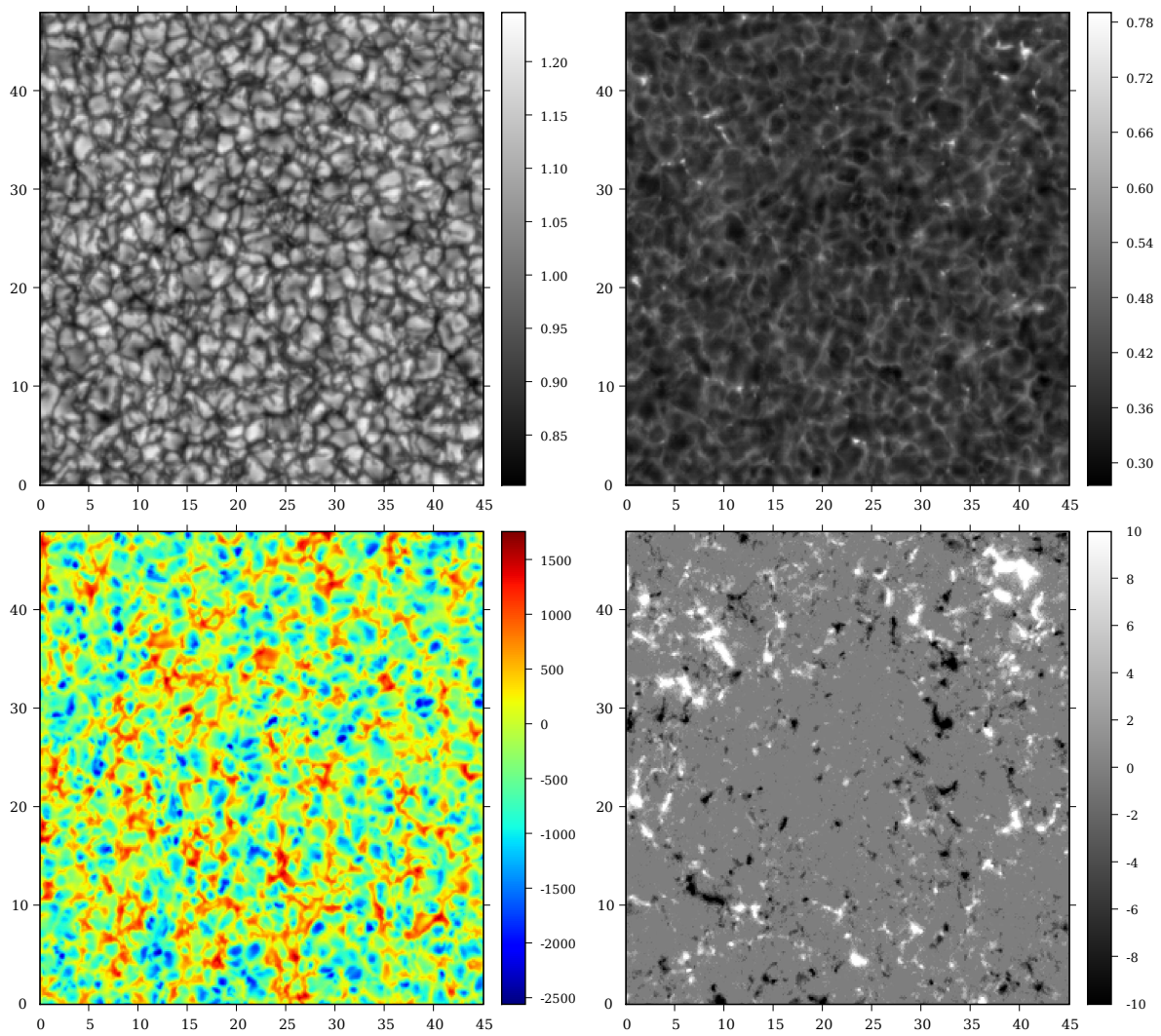

Figure 2.13: *Left to right, top to bottom:* continuum intensity at 630 nm, line-core intensity of Fe I 630.25 nm, velocity of the Fe I 630.25 nm line ($\mathrm{m\,s^{-1}}$), and V_{tot} in pm. This is a small area of the whole observed region. In the velocity map, blue and red colors correspond to up- and downflows, respectively. Dark intergranular lanes in the continuum intensity map are co-spatial with redshifts in the velocity map. A strong magnetic flux concentration in V_{tot} map, e.g., at $[38, 42]$, is bright in both top panels. Note that such strong flux concentrations are generally located in intergranular lanes.

field of view comprised an area of $162 \times 302\,\mathrm{arcsec}^2$ with a spatial sampling of 0.16 arcsec along the slit and 0.15 arcsec in the scanning direction. Figure 2.13 shows a small part of the observed area. The spatial resolution of the resulting spectropolarimetric maps was approximately 0.3 arcsec, and the spectral sampling was 2.15 pm. The RMS continuum contrast at 630.0 nm was around 7.5 %, far above the 3 % value typically observed from the ground at the same wavelength (Rezaei et al. 2007c; Khomenko et al. 2005a). This same

data set served Lites et al. (2007b, 2008) in an investigation of the horizontal magnetic fields in the quiet Sun.

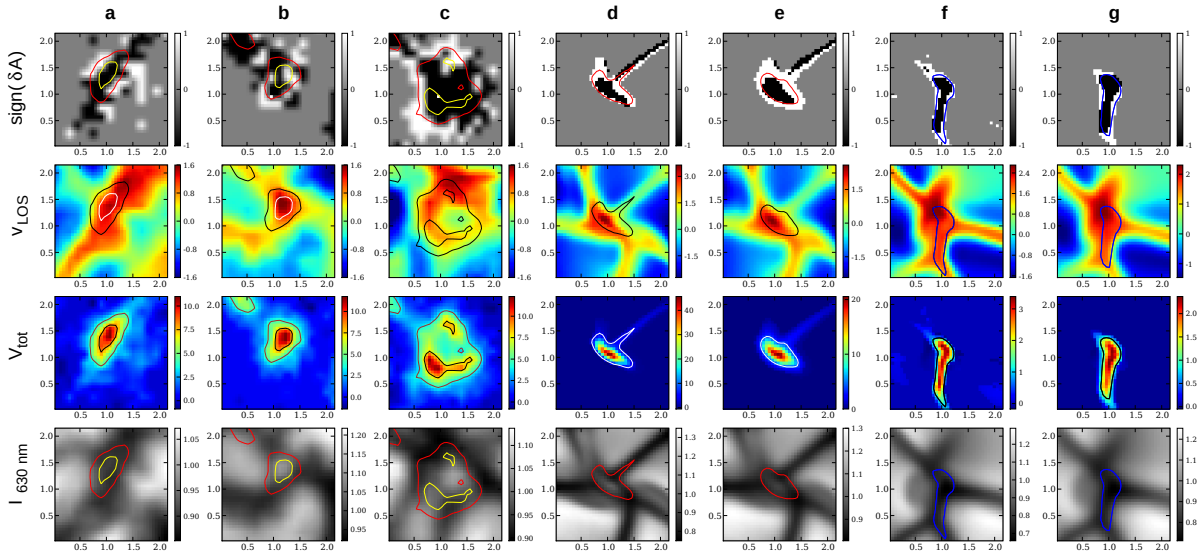

Figure 2.14: *Columns a-c*: observational data obtained with the spectropolarimeter of Hinode/SOT. *Columns d and f*: synthetic data from the 3D MHD simulation. *Columns e and g*: same as d and f but after application of the SOT-point-spread function (PSF) to the synthetic intensity maps (Wedemeyer-Böhm 2008). *Rows from top to bottom*: the sign of the Stokes-V area asymmetry for the line Fe I 630.25 nm, where black and white correspond to negative and positive, respectively; the Fe I 630.15 nm line-wing velocity in $\mathrm{km\,s^{-1}}$; V_{tot} of Fe I 630.25 nm in mÅ; and the continuum intensity at 630.0 nm. Contours refer to V_{tot}. Axis labels are given in arcsec.

2.3.2 Numerical simulation

The three-dimensional magnetohydrodynamic simulation comprised an area of $4\,800 \times 4\,800\,\mathrm{km}^2$, corresponding to $6.6 \times 6.6\,\mathrm{arcsec}^2$ and spanned a height range of 2 800 km from the top layers of the convection zone to the middle chromosphere. Details of the simulation, carried out with the CO^{5}BOLD code, can be found in Schaffenberger et al. (2005, 2006).

Initially, a homogeneous vertical magnetic field with a strength of 1 mT was superposed on a model of relaxed thermal convection. After relaxation, fields of mixed polarity occurred throughout the photosphere with an area-fractional imbalance typically of 3:1 for fields stronger than 1 mT. Similar polarity imbalances of even larger fields of view also occur in observational data (Lites 2002). Because of the periodic side boundaries and the conditions that the magnetic field must remain vertical at the top and bottom boundaries, the horizontally averaged vertical net magnetic-flux density remains 1 mT throughout the simulation. This value compares very well with the mean flux density

of 1.12 mT reported by Lites et al. (2008) for the Hinode data set. The mean absolute horizontal field strength was 2.5 mT in the upper photosphere of the simulation, 2.5 times the net vertical flux density. Lites et al. (2008) reported a ratio of 5. The difference was elaborated in details by Steiner et al. (2008).

The grid constant of the computational domain in the horizontal direction was 0.055 arcsec (120^3 grid cells), three times smaller than the spatial sampling of the Hinode SP data. The simulation was advanced for 4400 s of real time. The results presented here refer to the last 2400 s, well after the initial relaxation phase. Using the SIR code (Ruiz Cobo & del Toro Iniesta 1992; Bellot Rubio 2003), we synthesized the Stokes profiles of the Fe I 630 nm line pair from a large number of simulation snapshots with a spectral sampling of 2 pm. The profiles were computed for a vertical LOS on each grid point. We additionally applied a theoretical PSF to the resulting intensity maps to account for the spatial resolution capability of the SOT optics (Wedemeyer-Böhm 2008).

Data analysis: The line parameters extracted from both the calibrated Stokes data of the observation and from the simulation included the area and amplitude asymmetry of Stokes-V, the line-core and line-wing velocities, and the total (signed) circular polarization, Eq. 2.3,

$$V_{\rm tot} = \int_{\lambda_{\rm b}}^{\lambda_0} V(\lambda)/I_{\rm c}\,{\rm d}\lambda - \int_{\lambda_0}^{\lambda_{\rm r}} V(\lambda)/I_{\rm c}\,{\rm d}\lambda\,,$$

where λ_0 is the zero-crossing wavelength of a regular Stokes-V profile, and $\lambda_{\rm r}$ and $\lambda_{\rm b}$ denote fixed wavelengths in the red and blue continua of the lines (similar to Rezaei et al. 2007c). The relative Stokes-V area asymmetry (Eq. 2.2) is defined as

$$\delta A = \left(\int_{\lambda_{\rm b}}^{\lambda_0} |V(\lambda)|\,{\rm d}\lambda - \int_{\lambda_0}^{\lambda_{\rm r}} |V(\lambda)|\,{\rm d}\lambda\right) \Big/ \int_{\lambda_{\rm b}}^{\lambda_{\rm r}} |V(\lambda)|\,{\rm d}\lambda\,.$$

Figure 2.14 shows a few selected examples of magnetic elements from the Hinode data (columns a-c) and the simulation (columns d-g). The observed ones were all taken from network cell interiors. Columns e and g are based on the same synthetic data as are columns d and f, respectively, but degraded with the theoretical PSF of SOT. The top row displays the sign of the area asymmetry: black corresponds to negative and white to positive area asymmetries. Gray indicates that the Stokes-V profile has a signal below the 3σ noise level (65% of the total field of view) or that it has an irregular shape (20 %), where most of the latter would classify as regular when lowering the noise level. This same threshold also applied to the simulation data of the panels in columns d-g, where we ignored Stokes-V-profiles with an amplitude less than $3.6 \times 10^{-3}\,I_{\rm c}$ for comparison with the Hinode data. In the rightmost two panels, this threshold is 5 times lower in order to highlight the case of a weak magnetic element that would have barely been detected with Hinode.

The line-wing velocity of Fe I 630.15 nm, shown in the second row, was obtained by averaging the Stokes-I Doppler shift in the intensity interval 0.8-0.9 $I_{\rm c}$. We set the convective blue shift of the line-core velocity in the quiet Sun to -0.2 km s^{-1}. Because of the low degree of polarization, the line-wing velocity was not spoilt by magnetic influence.

The third row displays $V_{\rm tot}$, whose contours are shown in all the panels. It is a linear measure of the magnetic flux density according to Lites et al. (1999) and Lites et al. (2008). From the fourth row, which shows the continuum intensity at 630 nm, we see that the magnetic flux concentration occurs mainly in the intergranular space.

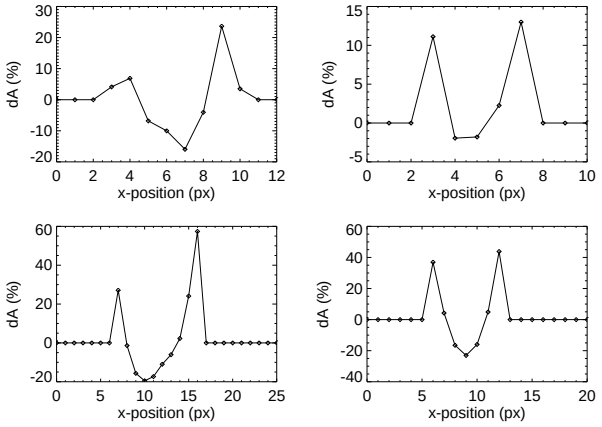

Figure 2.15: Variation in δA across magnetic elements from the Hinode data *(top row)* and the simulation *(bottom row)*. From left to right and top to bottom, the sections are taken from the data corresponding to columns a, b, d, and f of Fig. 2.14.

2.3.3 Current sheets at the boundary of magnetic elements

Both the observation and the simulation show magnetic elements of either sheet-like or roundish shape, possessing the same striking pattern with regard to the Stokes-V asymmetry: a central region with negative Stokes-V area asymmetry is surrounded by a narrow seam of pixels having positive area asymmetry (Fig. 2.14, first row). Plotting δA across a magnetic element, we find that $|\delta A|$ is typically larger in the periphery than in the central region of the magnetic flux concentration. Representative cross sections that demonstrate this behavior are shown in Fig. 2.15 for both the observation and the simulation. Along with δA in the top right panel of Fig. 2.15, Fig. 2.17 also gives the corresponding observed Stokes-V profiles. Also from Fig. 2.14 we see that the magnetic elements are located within and surrounded by a downdraft.

To obtain deeper insight, we consider in Fig. 2.16 the vertical cross section through the simulation snapshot shown in column d of Fig. 2.14 for the position $y = 1.15$ arcsec. It displays the magnetic field strength (color-coded) together with the velocity field, projected on the vertical plane (white arrows). The horizontally running curve indicates optical depth $\tau_{500\,\rm nm} = 1$. A magnetic flux concentration was forming in the downdraft and has reached a field strength of 0.13 T at $\tau_{500\,\rm nm} = 1$. Close to the surface of optical depth unity and through the photosphere, a relatively sharp, funnel-shaped boundary separates the magnetic flux concentration from the weak-field or field-free surroundings.

The inner vertical white lines indicate a central part of the flux concentration ($880 < x < 1120$ km), where Stokes-V profiles have $\delta A < 0$. This is because their LOS sample increasing field strength and increasing downflow velocity with increasing continuum optical depth (Solanki & Pahlke 1988). This situation changes drastically in the peripheral

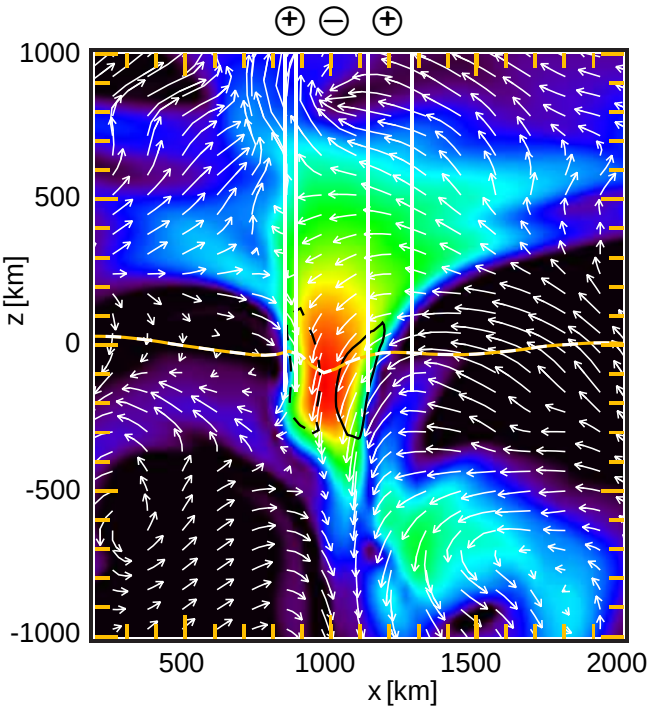

Figure 2.16: Vertical cross section through the simulation box corresponding to position $y = 1.15$ arcsec of the column d of Fig. 2.14. It displays the logarithmic magnetic field strength (from 1 to 200 mT, color-coded), together with the velocity field, projected on the vertical plane (white arrows) and the electric current density normal to the plane (black contours). Optical depth $\tau_{500\,\mathrm{nm}} = 1$ is shown as well. The white vertical lines indicate the ranges in which Stokes-V profiles from vertical LOS have either positive or negative area asymmetry, δA. Outside this range, the Stokes-V signal is below the 3σ noise level of the observations. $\delta A(x)$ is plotted in the lower left panel of Fig. 2.15.

region $840 \leq x < 880$ km and $1120 < x \leq 1280$ km (also indicated with white lines), where $\delta A > 0$. Here, the downflow speed still increases with optical depth; but because of the funnel-shaped flux concentration, the LOS traverse a magnetic boundary layer, where the field strength rapidly drops with increasing optical depth. The combination of increasing velocity and decreasing field strength produces positive area asymmetry. From this, we conclude that the narrow seam of positive area asymmetry in the periphery of magnetic flux elements seen in the Hinode data is a consequence of their well-defined boundary (or magnetopause) that expands with height in a funnel-like manner.

As an immediate consequence of Ampère's law, this boundary carries an electric current sheet. The black contours in Fig. 2.16 indicate a current density of $0.5\,\mathrm{Am}^{-2}$, encircling higher values of up to $4.0\,\mathrm{Am}^{-2}$. This refers to the current component perpendicular to the section plane, which flows in the opposite direction on either side of the magnetic flux concentration (Steiner 2007).

If the magnetic flux concentration was inclined enough w.r.t. the viewing direction, the LOS traversed the boundary layer on only one side of the flux concentration, which led to a one-sided seam of positive area asymmetry. This is almost the case in Fig. 2.16 (and corresponding δA-panel of Fig. 2.14), where the flux concentration is slightly inclined to the right making the seam of positive δA to the left much narrower than that on the right side. In fact, most magnetic elements in the field of view of the observation show a one-sided pattern like in the upper right corner of the synthetic δA-map in columns d or e.

Because the mean magnetic flux density in the inter-network is low, granular flow

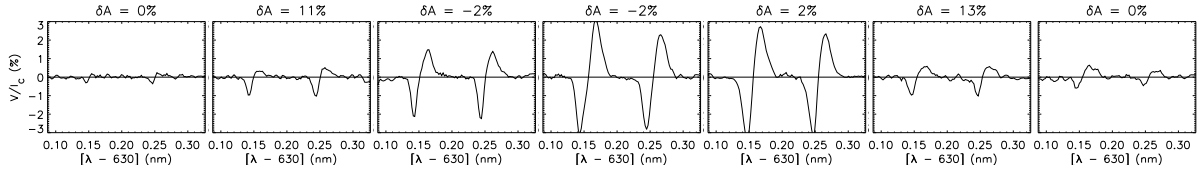

Figure 2.17: Stokes-V profiles from the Hinode data across the magnetic element of column b of Fig. 2.14. $\delta A(x)$ for the same section is shown in Fig. 2.15 (top right panel).

gathers only small amounts of flux so that only small and weak magnetic flux concentrations form (Steiner 2003a). They form and disperse with the onset and cessation of intergranular downdrafts. Therefore we observed strong downflows associated with the magnetic elements considered in this work. Indeed, Grossmann-Doerth et al. (1996b), Martínez Pillet et al. (1997), and Sigwarth et al. (1999b) also observe mainly downflows associated with weak magnetic signals. In combination with increasing field strength, these downflows give rise to negative area asymmetry. Yet, the peripheral positive area asymmetry is larger (Fig. 2.15) and may partially balance or even outweigh the negative contribution when observing at a lower spatial resolution.

Langangen et al. (2007) found that the downdraft velocity near the edges of magnetic elements is larger than in the central part. Here we find in both observations and simulation the maximum speed in the center of the flux concentration. In the simulation this is because the magnetic element forms as a consequence of an intergranular downdraft, with peak velocity in the center. This is different from the regime of a mature strong flux concentration for which simulations exhibit veritable downflow jets near their edges but not in the center (Steiner et al. 1998; Shelyag et al. 2007). This regime might be more representative of the active region elements observed by Langangen et al. (2007).

Grossmann-Doerth et al. (1988, 1989) and Solanki (1989) first pointed to the peripheral, canopy-like magnetopause of magnetic elements as the origin of the observed positive Stokes-V area asymmetry. Steiner (1999) found this effect at work in a two-dimensional MHD-simulation, but also found that the central region of the magnetic flux sheet tends to have negative values and that a delicate balance with the peripheral region exists in which the positive values may dominate and outweigh the negative ones. These findings have recently been confirmed in a three-dimensional environment by Shelyag et al. (2007). Bellot Rubio et al. (2000) came to a similar conclusion based on semi-empirical modelling. Leka & Steiner (2001) found a similar pattern in the Stokes-V area asymmetry in pores and magnetic knots. Here, for the first time, we find this pattern in observations of small-scale magnetic elements in the network cell interior.

Conclusion: Spectro-polarimetric data of a quiet Sun area close to the disk center obtained with SOT on board Hinode were analyzed. We find magnetic elements of either a roundish (tube) or an elongated (sheet) shape, which show Stokes-V profiles of negative area asymmetry in the center, framed by pixels of larger, positive area asymmetry. A comparison with results from 3D MHD simulations suggests that this peculiar pattern in

Stokes-V area asymmetry (first predicted by Steiner 1999) is due to the confined nature of the field in magnetic elements with a funnel-shaped boundary layer that gives rise to a steep gradient in field strength along the LOS. We also conclude that this kind of magnetic element of the internetwork is accompanied by electric current sheets. While these conclusions are evident from the comparison, we cannot exclude the hypothesis that a suitable magnetic structuring on scales not resolved by the present observation and simulation would lead to the observed pattern in δA.

2.4 Temporal evolution of magnetic elements

Magnetic features are best studies in polarized light, due to their well-defined spectropolarimetric signature which allows them to be identified. Polarimetric observations indicate that there is virtually no area on the Sun without magnetic field (Trujillo Bueno et al. 2004; Lites et al. 2008; Steiner et al. 2008). In strong flux concentrations, the field lines are nearly vertical to the surface. Magnetic elements are structures with diameters smaller than a few hundred kilometres. In the hierarchy of the magnetic structures, the magnetic elements take the position between dark and bright structures, i.e., between pores and network bright points (see Sect. 1.5). While the magnetic elements are not visible in continuum or line wing, they appear bright in the core of the chromospheric Ca II H and K lines. The convective motion associated with the photospheric granulation sweeps the magnetic flux toward the intergranular lanes. Due to the geometry of these lanes, the magnetic flux is arranged there either in chains of individual flux tubes or elongated sheets. This behavior is seen in high-resolution observations (Berger et al. 2004; Rouppe van der Voort et al. 2005) as well as in numerical simulations (Schaffenberger et al. 2006, Steiner 2005, Vögler et al. 2005).

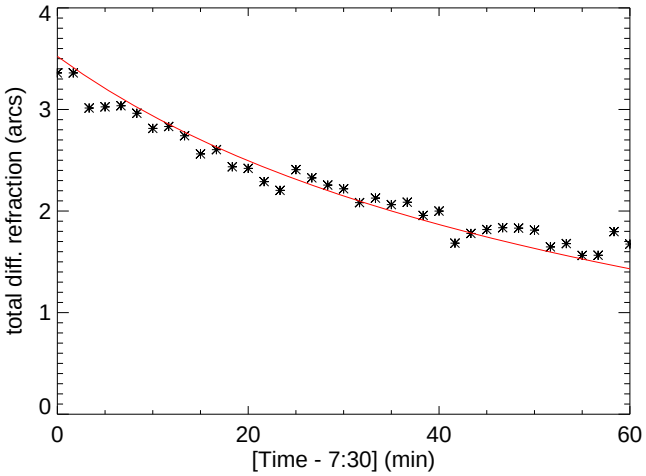

Figure 2.18: Differential refraction between the blue and red channels in POLIS. Stars denote the measured shifts and the curve shows calculated values for the given date and time (Beck et al. 2008). The component which was perpendicular to slit was larger than the component along the slit.

Magnetic flux cancellations are common events in the solar atmosphere. There are examples in which it led to a clear enhancement in the chromospheric intensity (Bellot

Rubio & Beck 2005; Beck et al. 2005a). They had a temporal cadence of seven minutes, comparing to 100 s in present data. Magnetic reconnection at the photospheric level was also studied by Litvinenko (1999) and Takeuchi & Shibata (2001). Rezaei et al. (2007c) presented Stokes-V profiles of the Fe I 630 nm line pair, where the two lines show opposite polarities in a single spectrum (OP profile). They suggested that it may be understood as a magnetic reconnection event at the solar photosphere with a line of arguments similar to Steiner (2000).

In this section, we present the temporal evolution of physical quantities before and after a magnetic reconnection event associated with the OP profile discussed in Sect. 2.2. In addition to the polarimetric data, we investigated Ca II H profiles which contain information about higher layers of the solar atmosphere.

2.4.1 Observations and data reduction

The data set used in this study is the same as introduced in the Sect. 2.2: a time-series of a small quiet Sun region close to disk center observed with the VTT in Tenerife, July 07, 2006. We normalized the Ca II H intensity profiles at the line wing at 396.490 nm to the Fourier Transform Spectrograph (FTS) profile (Stenflo et al. 1984). Following Cram & Damé (1983) and Lites et al. (1993), we defined a set of parameters to quantify properties of the Ca II H line profiles, Table 2.3 (a more detailed explanation will be given in Chapter 3). The normalization procedure of the calcium line profiles is very similar to that described by Rezaei et al. (2007a).

Table 2.3: Definition of the characteristic parameters of the Ca II H line profile following Lites et al. (1993). V/R is defined as H_{2V}/H_{2R}. Wavelengths are in nm.

parameter	wavelength range (nm)
H-index	396.849 ± 0.050
H_{2V}	396.833 ± 0.008
H_{2R}	396.865 ± 0.008
W1 (outer wing)	396.632 ± 0.005
W2 (middle wing)	396.713 ± 0.010
W3 (inner wing)	396.774 ± 0.010

Due to the wavelength dependence of the refractive index of air, the solar images at different wavelength do not coincide in the focal plane (Filippenko 1982; Reardon 2006; Beck et al. 2008). Differential refraction leads to a shift between images of different wavelengths. The amount of the displacement depends on the zenith distance of the Sun (Appendix B). We used the procedure explained in Beck et al. (2008) to remove the effect of differential refraction between the red and blue channels of POLIS. In Fig. 2.18, the observed values of differential refraction between the blue and red channels of POLIS (asterisks) are compared with the theoretical amounts (curve). There is a time lag between

co-spatial data in the two channels; the polarimetric data was actually recorded 10 seconds later than the calcium data for the case shown in Fig. 2.19.

As explained in Sect. 2.2, a continuum speckle channel in POLIS recorded a larger field of view at 500 nm, simultaneously to the observations of spectral lines. The obtained high spatial resolution images were aligned with the POLIS intensity maps. Figures 2.19 and

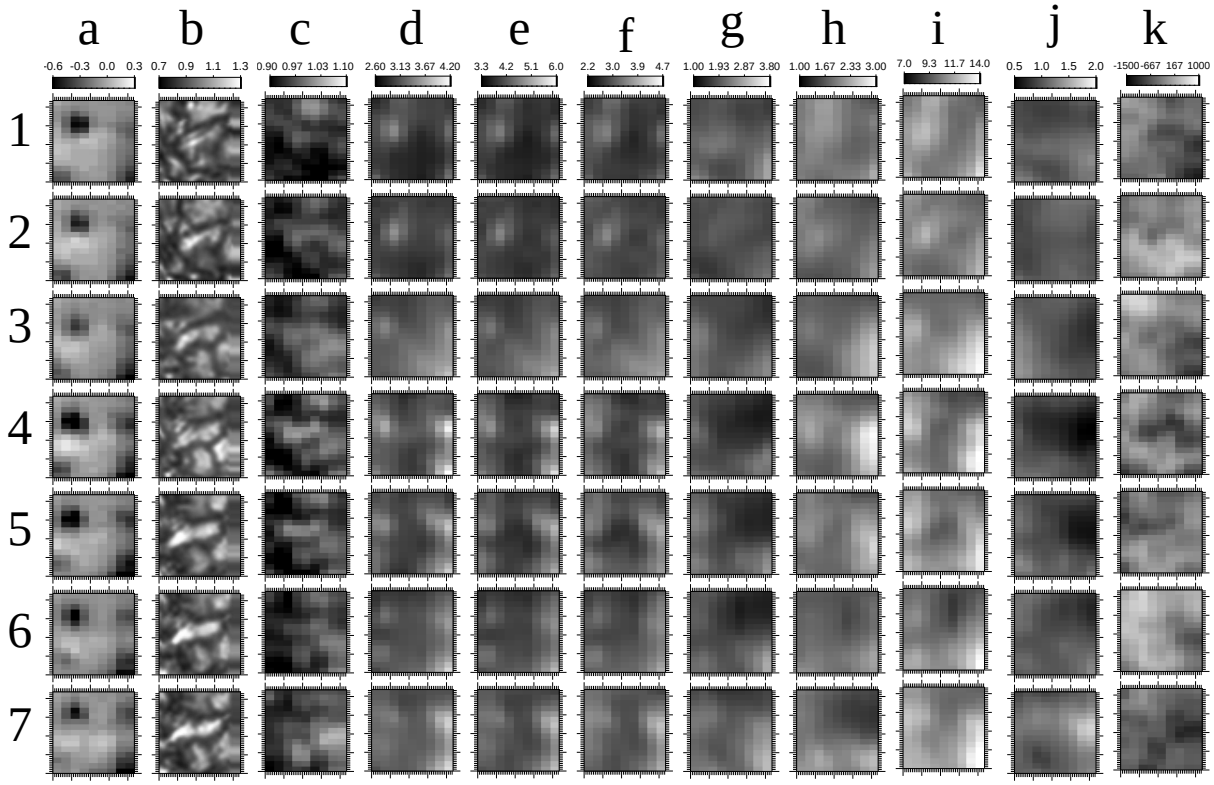

Figure 2.19: Temporal evolution of physical parameters in a flux cancellation event. *From left to right: a)* $V_{\rm tot}$, *b)* speckle reconstructed image, *c)* Stokes-I, *d)* W1, *e)* W2, *f)* W3, *g)* H_{2v}, *h)* H_{2r}, *i)* H-index, *j)* V/R, and *k)* Fe I 630.25 nm velocity in $\mathrm{m\,s^{-1}}$ (see Table 2.3 for definitions). Numbers on the left show the time steps where each time step is about 97 seconds. The OP profile (Sect. 2.2) was observed in time step No. 4 ($x = 1$, $y = 2$). There are weak enhancements in the corresponding chromospheric emissions, e.g., $(4 - i)$. Maps in columns $(d - i)$ are in pm. The spatial extension of each map in both axes is 4.4 arcsec.

2.20 show two examples of flux cancellation events: one with and one without significant chromospheric brightening. This can be seen by comparing the maps $(4 - i)$ in Fig. 2.19 and $(3 - i)$ in Fig. 2.20.

We used the signed integral of the Stokes-V profile, $V_{\rm tot}$ (Eq. 2.3), which traces the magnetic flux (Lites et al. 1999; Rezaei et al. 2007c). It enabled us to follow weak polarimetric signals where the Stokes-V amplitude is below the $3\,\sigma$ noise level. The column a of Figs. 2.19 and 2.20 shows the variation of $V_{\rm tot}$ for seven time steps around the reconnection frame (row 4). The cancellation started as the smaller patch (white in Fig. 2.19)

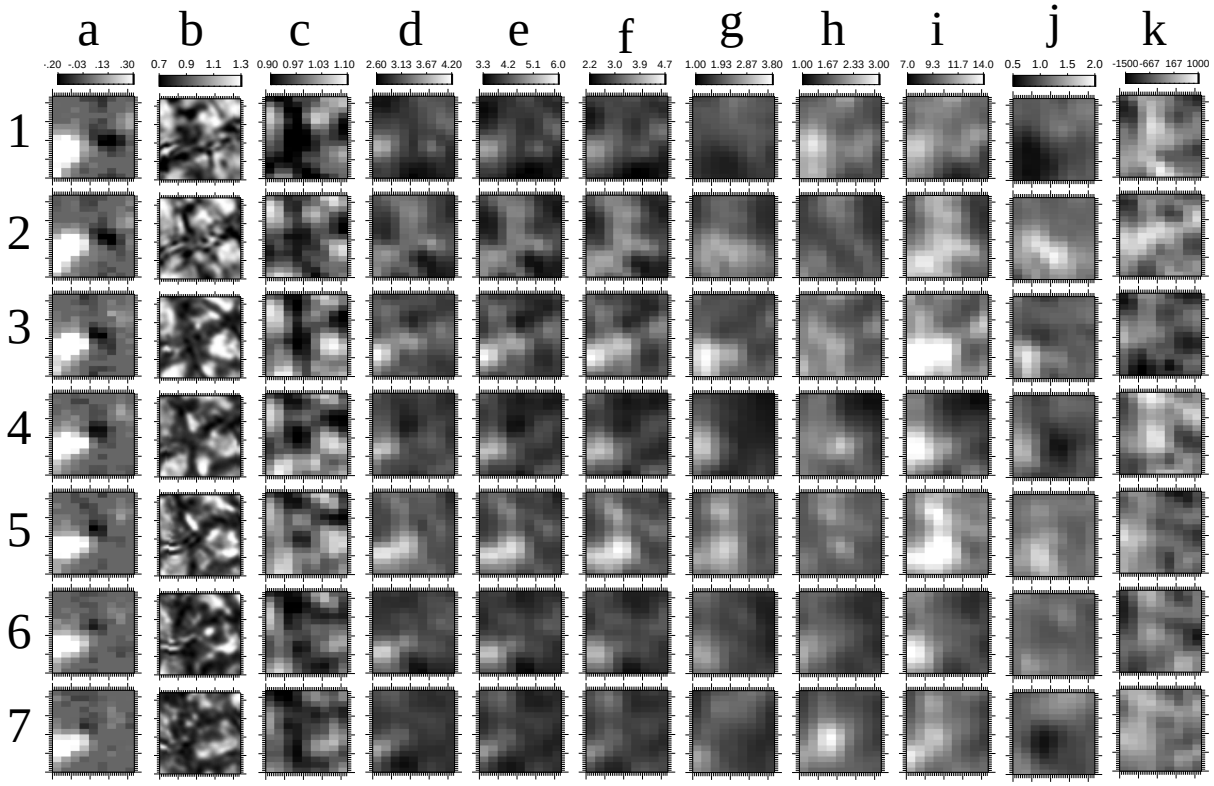

Figure 2.20: Same as Fig. 2.19 but for another example of flux cancellation in our data. In this case, there is a significant enhancement in the chromospheric emission (H-index, H_{2v}, and H_{2r}, columns *i, g,* and *h*), far stronger than the case in Fig. 2.19.

concentrated and lasted until it has almost disappeared.

As noted in Table 2.3, the V/R is a measure of the asymmetry between the violet and red emission peaks (H_{2v} and H_{2r}, respectively) in the calcium profile. Signatures of bright and dark structures in V/R maps (column *j*) can be directly compared with H_{2v} and H_{2r} maps (columns *g* and *h*, respectively). The wing intensities show the gradual variation of the intensity, in-between the Stokes-*I* and the calcium core parameters. The photospheric velocity, column *k*, shows the patterns of up- and downflow structures corresponding to granules and intergranular lanes (e.g., compare the upper left corner of $(3-b)$ and $(3-k)$, Fig. 2.19).

2.4.2 Signature of magnetic reconnections in the solar atmosphere

Magnetic reconnection: Magnetic reconnection explains a wide range of phenomena within single universal concepts like many fundamental concepts in physics. Reconnection is a topological restructuring of a magnetic field caused by a change in the connectivity of its field lines. Magnetic reconnection is the process by which magnetic lines of force break

and rejoin into a lower-energy configuration. This change allows the release of stored magnetic energy. Magnetic reconnection is considered to be the fundamental process by which magnetic energy is converted into plasma kinetic energy (Giovanelli 1946; Priest & Forbes 2000). While there are clear examples of magnetic reconnection events in the solar chromosphere and corona (Sturrock 1966; Jing et al. 2008), there are only few examples of photospheric reconnections (Litvinenko 1999).

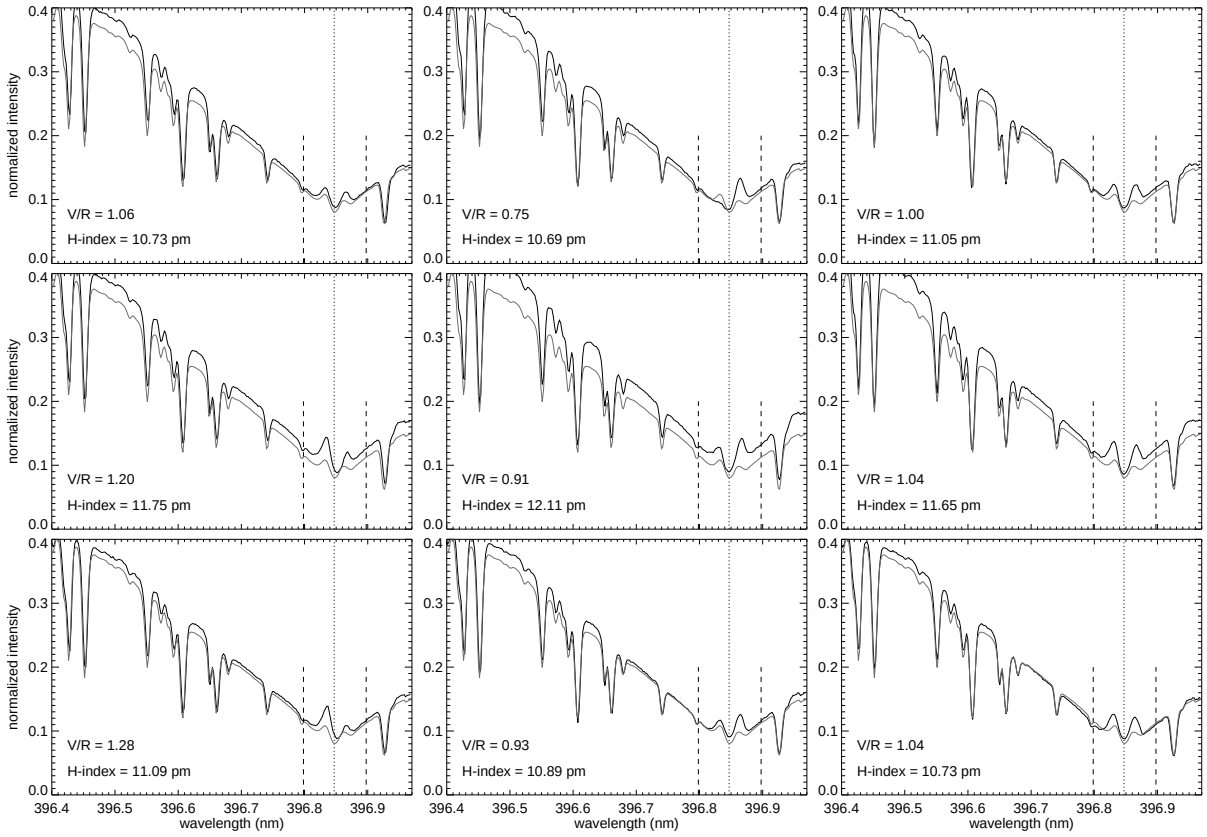

Figure 2.21: Variation of emission peaks at three locations ([1,3] top, [0.5, 2.6] middle, [0.5, 2.2] bottom) in time-steps 3 (left), 4 (middle), and 5(right) for the Fig. 2.19 example. The gray profile is the average of a few thousand profiles. The dashed lines show a distance of ± 0.05 nm from the average calcium core, which is indicated by a vertical dotted line.

Similarities between the two observed events: The negative polarity patch in Fig. 2.19 (column *a*) was a network patch, which was present during the whole observing run. In contrast, the positive patch gathered from diffuse flux, enhanced, and almost disappeared (the positive patch corresponds to the white color in Figs. 2.19 and 2.8). Since the magnetic flux is continuously replaced in the network, events like this may be common in the solar photosphere (Schrijver & Shine 1997). The strong positive patch in Fig. 2.20 (column *a*) was not a network component. However, it was much stronger than

the negative one and persisted for the whole observing sequence. Although, the larger patches in both cases survived the cancellation event, they weakened clearly. In both cases, the cancellation event happened in an intergranular vertex (see panel $(4-b)$ in Figs. 2.19 and 2.20). Therefore, these two events have comparable configurations at the photospheric level.

Differences: The comparison of the two flux cancellation events presented in this section demonstrates essential differences in the chromospheric reaction. In the first case, there is a mild chromospheric brightening at the cancellation site, e.g., row (4) in Fig. 2.19. In contrast, rows (3-5) of Fig. 2.20 show a significant brightening in the H-index at the cancellation site. Note that the color bar has similar scales for the H-index. At the same time, columns (d, e, and f) that represent the wing intensities showed similar patterns as the corresponding calcium core (columns i) with lower contrast. Comparing columns (d, e, and f) in row (3) of Fig. 2.20, the brightening increases toward the core. In contrast, these columns in row (4) of Fig. 2.19 show the opposite: the brightening in d is larger than e, and in e it is larger than f. So the wing intensities show a different vertical gradient. While in the first example the deeper layer was brighter than the upper layer, the second example showed the reverse behavior.

The H_{2v} emission peak in the average quiet Sun calcium profile is stronger than H_{2r} emission peak (e.g., Linsky & Avrett 1970). In contrast in both cancellation events, we observed a stronger H_{2r} emission peak comparing to H_{2v}. This can be seen by comparing columns g and h, or by looking at column j (V/R map) in Figs. 2.19 and 2.20. While the cancellation site in the first example (about $[1, 2]$) is mildly dark in map $(j-4)$ of Fig. 2.19, there is a darker structure in map $(j-4)$ of Fig. 2.20 at the cancellation site(about $[2, 2.5]$). Figure 2.21 shows nine calcium profiles, sampled at three spatial locations and three time instants, at the cancellation site (Fig. 2.19). These plots display the full profiles: the H_{2r} and H_{2v} peaks of the cancellation site can be compared with each other. The left, the middle, and the right columns in Fig. 2.21 show three profiles before, during, and after the cancellation, respectively. The profiles in the left and right columns of Fig. 2.21 show either a stronger H_{2v} peak or comparable H_{2v} and H_{2r} peaks. The fact that the profiles in the middle column of Fig. 2.21 show a H_{2r} peak that is stronger than H_{2v} is in agreement with Beck et al. (2005a).

Conclusion: Time-series of co-spatial and co-temporal polarimetric data of a quiet Sun region revealed a variety of connections between photospheric flux cancellations and chromospheric enhanced emission. We present two examples of magnetic flux cancellations with different levels of the enhanced chromospheric emission. In the first case, the intensity contrast in outer wing is larger than the inner wing, and is vice versa in the second case. Since different wing wavelengths form at different geometrical heights, we attribute the difference to the geometrical height at which the cancellation happened. This is in accordance with the interpretation of the opposite-polarity profile as a signature of photospheric reconnection by Rezaei et al. (2007c).

2.5 Single-lobe Stokes-V profiles: extreme cases of asymmetry

As explained in Sect. 1.3, Stokes-V profiles are expected to be strictly antisymmetric w.r.t. their zero-crossing wavelength, if no velocity gradients with height is present and if LTE applies (Auer & Heasley 1978; Illing et al. 1975; Landi degl'Innocenti & Landolfi 1983). Stokes polarimetry provides detailed information about the magnetic field and its interaction with the plasma in the solar photosphere and chromosphere. While most of the observed Stokes-V profiles in active regions and the network are nearly antisymmetric, strongly asymmetric and *abnormal* V profiles are common in the inter-network (abnormal V profile means profiles either with one lobe or more than two lobes; Sigwarth 2001). We observed several areas in quiet Sun regions close to the center of the solar disk with the SP of the SOT on board the Hinode space mission (Kosugi et al. 2007). Stokes profiles of the neutral iron lines at 630.15 and 630.25 nm were recorded with a spatial resolution of 0.3 arcsec and a 3σ noise level of $3.4 \times 10^{-3}\, I_{\rm c}$. In this study, we checked 6.5 million Stokes-V profiles. Some 18 % of them show just a single-lobe above the 3σ noise level which is more than half of all profiles with an amplitude above the 3σ noise level. We separated profiles with only a blue lobe from profiles with only a red lobe. This is because theoretical investigations on single-lobe profiles predicted different formation scenarios for blue-only and red-only profiles (Steiner 2000).

There are also other categories of abnormal Stokes-V profiles in which there are significant differences between the Fe I 630.15 and 630.25 nm lines. For example, we have profiles where Fe I 630.15 nm line has two lobes while 630.25 nm line shows three lobes (Q-like) or vice versa. An extreme case of such profiles is the OP profile (Sect. 2.2). We will not discuss these cases of profiles here.

2.5.1 Observations and data reduction

Five quiet Sun regions close to disk center ($\mu = \cos\theta > 0.98$) were observed with the Hinode SP in different observing epochs from March to September, 2007 (Ichimoto et al. 2008; Tsuneta et al. 2008). Table 2.4 lists properties of the observed regions. Data set #1 was observed by Lites et al. (2008) while the rest were observed within International Time Program (ITP) 2007 campaign[4]. The exposure time for all these observations (Table 2.4) was 4.8 s, and the noise level in the polarimetric data was $3\sigma = 3.4 \times 10^{-3}\, I_{\rm c}$, the same as presented in Sect. 2.3.1. The spectral sampling of 2.15 pm corresponds to a velocity dispersion of $1.0\,{\rm km\,s^{-1}}$ per pixel.

In total, 6.5 million profiles have been analyzed. Figure. 2.22 shows examples of blue-only and red-only profiles. Among the profiles with an amplitude above the 3σ noise level, 14 % and 18 % showed a normal shape with two antisymmetric lobes and only a single lobe, respectively. For each single-lobe profile, amplitude, area, FWHM of the lobe

[4]ITP allocates observing time at several telescopes. So it makes it possible to observe an area with all the accessible telescopes. The principal investigator of this campaign was Dr. Rolf Schlichenmaier, KIS.

and wavelength position of the lobe were determined along with line-core intensity and velocity of the corresponding Stokes-I profiles. In addition, the integral of the total linear polarization signal, $L_{\rm tot}$, (Lites et al. 1999),

$$L_{\rm tot} = \int L(\lambda){\rm d}\lambda = \int \sqrt{{\rm Q}(\lambda)^2 + {\rm U}(\lambda)^2}\ {\rm d}\lambda, \tag{2.7}$$

was also calculated. Note that the above definition, even for a pure noisy profile, yields a positive value since $L(\lambda)$ is always positive. Hence, there is a lower level in the measured values corresponding to noisy profiles (right panels, Fig. 2.23).

Table 2.4: Properties of the maps observed with Hinode SP and used in single-lobe analysis. Exposure time and 3σ noise level for all of them were 4.8 s and 3.4 $\times$ $10^{-3}\,I_{\rm c}$, respectively. The spatial sampling along the slit and perpendicular to the slit were 0.15 and 0.16 arcsec, respectively (Kosugi et al. 2007).

No	Date	area (arcsec^2)
1	Mar 10, 2007	302×162
2	Sep 07, 2007	344×76
3	Sep 14, 2007	182×76
4	Sep 15, 2007	344×76
5	Sep 16, 2007	454×76

Table 2.5: Statistics of single-lobe Stokes-V profiles in each amplitude class for blue-only (n_b) and red-only (n_r) profiles. Note the increase of ratio with increasing amplitude.

amplitude class (% $I_{\rm c}$)	n_b	n_r	n_b/n_r
$0 < a < 1$	722302	433310	1.7
$1 < a < 2$	50127	9345	5.4
$2 < a < 3$	4369	192	22.9
$3 < a < 4$	691	15	46.1

The fraction of single-lobe profiles indicates how often the physical conditions in the solar atmosphere consists of sufficient gradients of parameters (T, ρ, ...) to form very asymmetric Stokes-V profiles, namely single-lobe profiles. In previous ground-based studies Sigwarth et al. (1999a), Grossmann-Doerth et al. (2000), and Sigwarth (2001) found that about 4 % of all profiles had only a single lobe. The spatial resolution and 3σ noise level in their data sets were 1 arcsec and 1.5 $\times$ $10^{-3}\,I_{\rm c}$, respectively. In contrast in our study (Table 2.4), we find that 18 % of all profiles are single-lobe. Our space-based data sets have a spatial resolution of 0.3 arcsec and a 3σ noise level of 3.4 $\times$ $10^{-3}\,I_{\rm c}$.

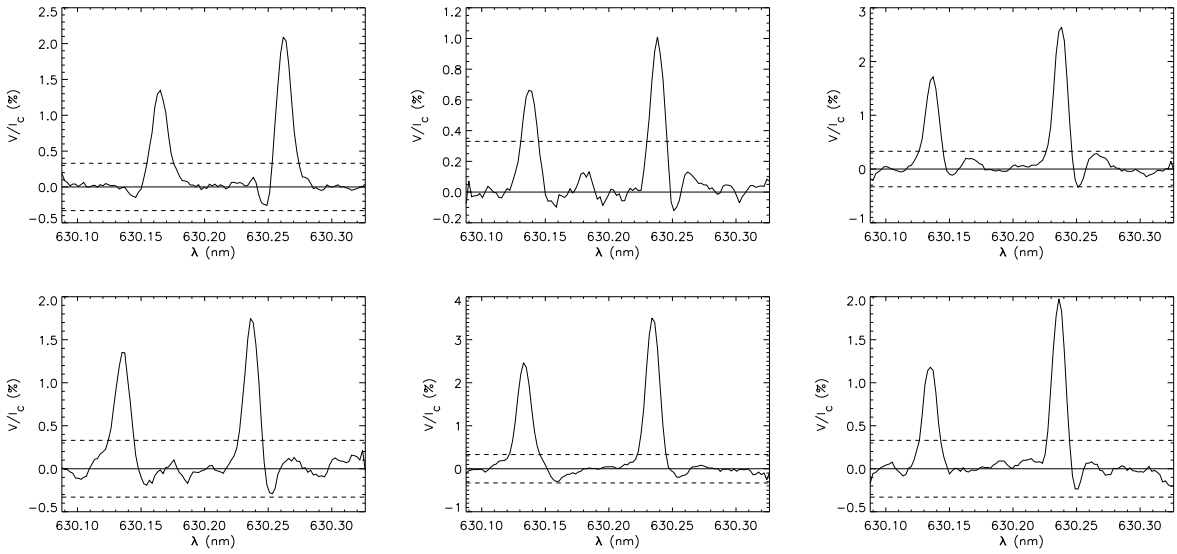

Figure 2.22: Sample single-lobe Stokes-V profiles. The top left panel shows a red-only profile while the rest show blue-only profiles. Horizontal dashed lines show the 3σ noise level of $\pm 3.4 \times 10^{-3}\, I_{\rm c}$.

The better spatial resolution and higher noise level in our data result in larger fraction of single-lobe profiles. In our data sets (Table 2.4) of the single-lobe profiles, 64 % are blue-only and 34 % red-only. This can be compared with Sigwarth et al. (1999a) who reported 80 % and 20 % for the blue-only and red-only profiles, respectively. The larger fraction of blue-only profiles in Sigwarth et al. (1999a) data is a direct consequence of worse spatial resolution of their data: they lost many small red-only profiles due to spatial smearing.

Blue-only vs. red-only: Single-lobe profiles were separated into two categories: profiles with only a blue lobe (blue-only profiles) and profiles with only a red lobe (red-only profiles). In each of the two categories, amplitude classes were created. For example, amplitude class of $1\,\% < a < 2\,\%$ means profiles with an amplitude between one and two percent of the average continuum intensity. Table 2.5 presents statistics of blue-only and red-only profiles in each amplitude class. As seen the right column of Table 2.5, ratio of blue-only to red-only profiles increases significantly with increasing amplitude. It means that the physical conditions leading to the formation of the high-amplitude blue-only profiles happen more frequent than the conditions required by the red-only profiles.

2.5.2 Average properties of blue-only and red-only profiles

Figure 2.23 shows scatter plots of area of the lobe (left panels), FWHM of the lobe (middle panels), and $L_{\rm tot}$ (right panels) versus amplitude. Top and bottom panels correspond to blue-only and red-only profiles, respectively. Each point in any of these plots represents average over the corresponding amplitude class (Table 2.5). Error bars indicate statis-

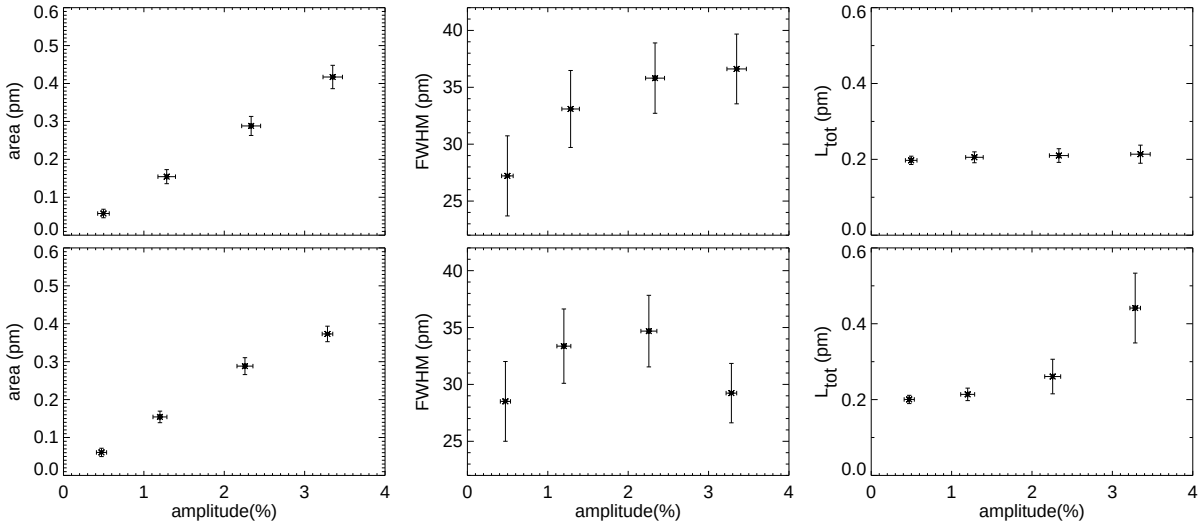

Figure 2.23: Plots of the area (*left*), FWHM (*middle*), and $L_{\rm tot}$ (*right*) vs. the amplitude of Stokes-V profiles. $\rm L_{tot}$ is an indicator for the transverse magnetic flux. Top (bottom) panels are results of the blue (red) lobe only profiles. Each point shows average properties of all profiles for the corresponding category, e.g., profiles with an amplitude between $1\,\%I_{\rm c}$ and $2\,\%I_{\rm c}$.

tical dispersion in the class, rather than the measurement error which is smaller. The amplitude and area of single-lobe profiles show a linear trend: the larger the amplitude, the larger the area. The FWHM of lobes also increases with increasing amplitude (middle panels). However, it levels off at about $2\,\%I_{\rm c}$ amplitude for blue-only profiles while decreases for red-only profiles from $2\,\%I_{\rm c}$ onward. Note that the FWHM of the lobe depends on the magnetic and thermal properties of the atmosphere along with values of the microturbulence and macroturbulence (Sect. 1.2).

The right panels of Fig. 2.23 show $L_{\rm tot}$ which is a tracer for the horizontal magnetic field (Lites et al. 2008). Comparison of the top- and bottom-right panels of Fig. 2.23 indicates that the magnetic field configuration was almost vertical in the case of blue-only profiles while there is a trend of increasing $L_{\rm tot}$ with increasing amplitude of red-only profiles. In other words, red-only profiles had a more inclined magnetic field geometry than the blue-only profiles. Since Q and U signals are intrinsically weaker than V (Sect. 1.3.5), they require longer exposure times to be recorded (e.g., Lites et al. 2008, his Fig. 10). Hence, one should be aware that the absence of linear polarization signal in our data is partly due to short exposures and low signal-to-noise ratio.

Figure 2.24 is similar to Fig. 2.23 except that it presents intensity parameters. The left panels show the line-core intensity of Fe I 630.25 nm line. The right panels show the continuum intensity at 630.10 nm. Unlike the red-only profiles (bottom row), the blue-only profiles (top panels) show that the intensity increases with increasing amplitude of the single-lobe blue-only profiles. If one use the intensity at a certain wavelength and the Plank equation (Eq. 1.1), it is possible to attribute a temperature to the measured intensity. This temperature is called the brightness temperature. In LTE, the brightness

temperature is a good tracer of the thermodynamic temperature. Since the continuum forms in LTE (Stix 2004) and the core of the Fe I 630.25 nm line also forms below the temperature reversal (where LTE mostly holds), we conclude that the blue-only profiles experienced hotter formation conditions than the red-only profiles.

Figure 2.25 shows an example of locations of blue-only profiles. The right panel shows the Stokes-V profiles at the slit position of the vertical white line (about 11 arcsec) in the continuum map of the observed area (left panel). The blue-only profile (Fig. 2.25, right panel, $y \approx 2$) appears inside a granule but not at its center. A direct consequence of this finding is that one expects to see upward motion in the Stokes-I signal, i.e., a blueshift in the line-core velocity. It is consistent with the upper right panel of Figure 2.26 which shows scatter plot of the line-core velocity vs. amplitude: blue-only profile at all amplitude classes have a blueshifted line-core position.

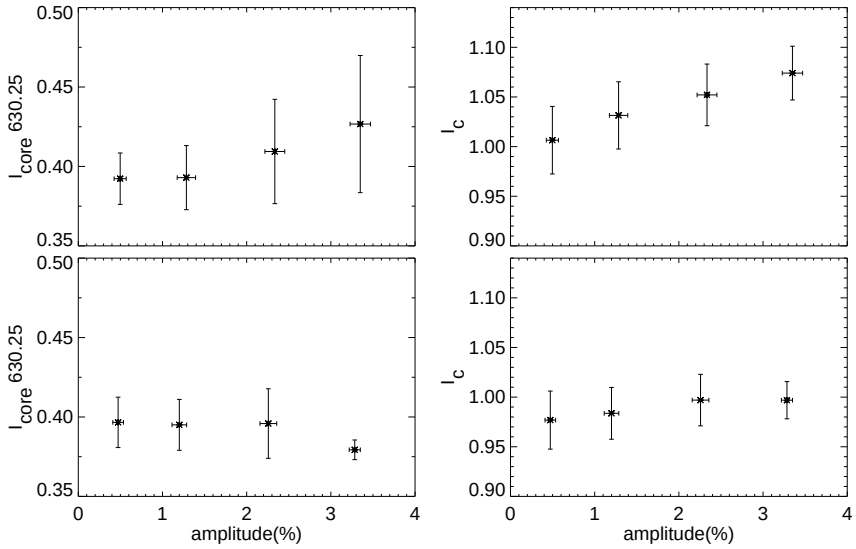

Figure 2.24: Plots of the amplitude of the V profiles vs. line-core intensity of Fe I 630.25 nm line (*left*), and 630 nm continuum intensity (*right*). Other properties are similar to Fig. 2.23.

The left panels of Fig. 2.26 show the *absolute* shift of the peak position of the Stokes-V lobe w.r.t. the *average* line-core position of the Stokes-I profile of the corresponding map. So in case of blue-only profiles, it shows negative of the real shift. Comparing the two left panels of Fig. 2.26, one finds that the shift of the Stokes-V lobe w.r.t. the average line-core position increases with increasing amplitude for the blue-only profiles. For the red-only profiles, the situation is reversed: large amplitude profiles had smaller redshift comparing to small amplitude profiles. A shifted single lobe may indicate either a larger magnetic field strength or more Doppler-shifted plasma in the magnetic part of the atmosphere. The right panels of Fig. 2.26 is the same as left panel for the line-core velocity. For blue-only profiles (top-right panel, Fig. 2.26), the Doppler shift of the Stokes-I profiles increases with increasing amplitude. The red-only profiles (bottom-right panel, Fig. 2.26) do not show a significant trend between the line-core velocity and the

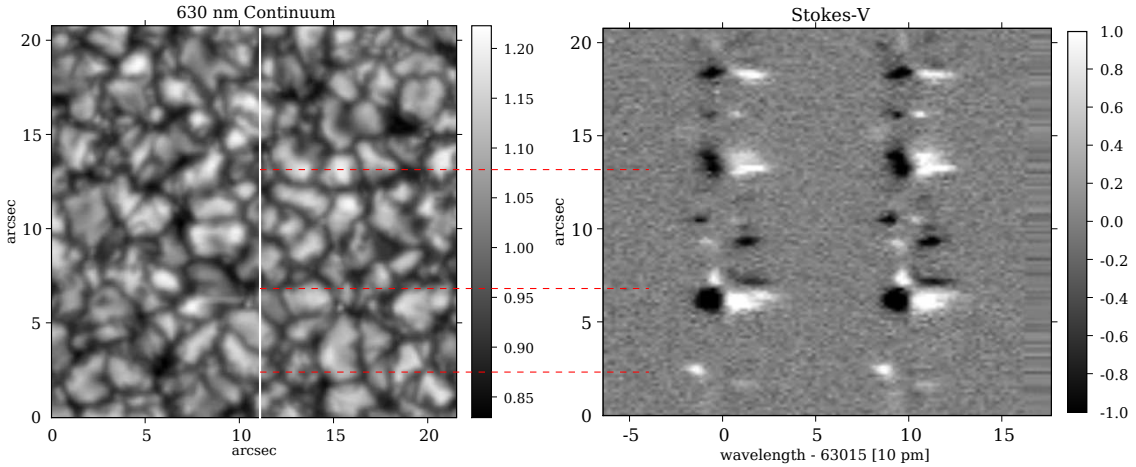

Figure 2.25: The left panel shows the 630 nm continuum intensity map derived from Stokes-I data. The right panel shows the Stokes-V raster signal corresponding to the vertical white line at about 11 arcsec. The horizontal dotted lines show the corresponding position of three magnetic structures. Note that the blue-only profile (bottom horizontal line) is located inside a granule. The Stokes-V map was saturated to $\pm 1\,\%\, I_{\rm c}$ for better visibility.

amplitude. A spectral line like Fe I 630.25 nm is not fully split in the weak field regime, i.e., when the Zeeman splitting is small compared to the Doppler width. In this regime, the amplitude increases linearly with increasing magnetic flux. In contrast, the distance of the two lobes, i.e., two sigma components, increases with the magnetic field strength only for high field strength (Fig. 1.9). Since top-right panel of Fig. 2.26 shows that blue-only profiles correspond to blueshifted line cores, one can assume that they have also experienced a blueshift in the magnetic part of the atmosphere. Stokes-I profiles form at a wider height range in the atmosphere while the Stokes-V profiles form exclusively in the magnetic part of the atmosphere. If there was the same amount of Doppler shift in the magnetic and non-magnetic parts of the atmosphere, we expect to see smaller shifts in Stokes-I than Stokes-V.

2.5.3 Comparison with model

Steiner (2000) presented two analytical models for single-lobe blue-only and red-only profiles. He considered two atmospheric components along the LOS: one magnetic and one non-magnetic. In the first model, blue-only profiles form in an atmosphere not much hotter than the average quiet Sun atmosphere and in presence of a downflow in the magnetic component. In the second model, there is an upflow in the field-free material along with a prominent temperature enhancement in the magnetic component. Observations at a spatial resolution of 1 arcsec (e.g., Sigwarth et al. 1999a) showed a downdraft in magnetic structures, and thus supported the first model. Our results of blue-only profiles, presented in the previous section, provide evidence for a hot atmosphere with an upflow in its field-free material. This is in accordance with the second scenario of Steiner (2000). The

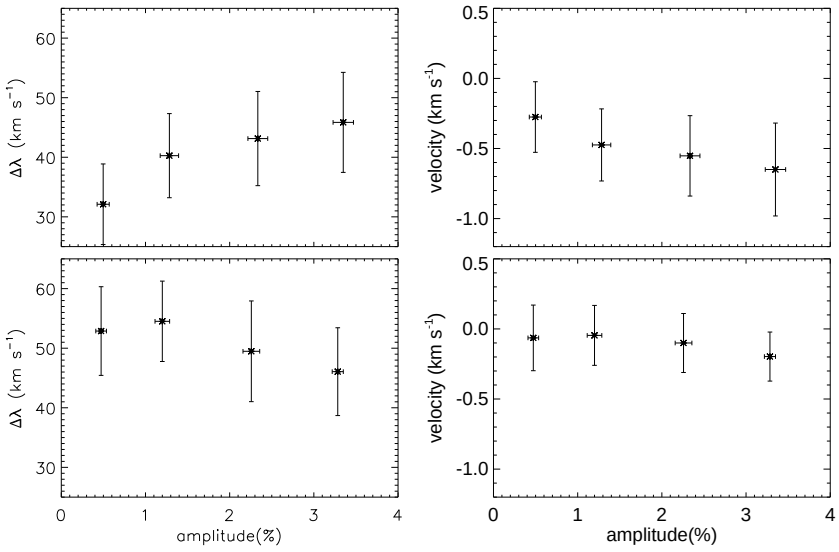

Figure 2.26: Plots of the wavelength of the peak of the lobe (*left*) and line-core velocity of Fe I 630.25 nm line (*right*) vs. amplitude of the V profiles. Other properties are similar to Fig. 2.23.

discrepancy between the old and new observational results can be explained as an effect of spatial resolution: the spatial resolution of our data is by a factor three better than the best ground-based polarimetric data.

Conclusion: Combining data of five separate quiet Sun areas observed with the Hinode SP, we gathered 6.5 million Stokes vectors with identical signal-to-noise ratio, spectral, and spatial resolution. The geometry of the observed regions, e.g., the heliocentric angle, was quite similar. We studied abnormal Stokes-V profiles in the inter-network and separated single-lobe profiles. Among single-lobe Stokes-V profiles with an amplitude above the 3σ noise level of $3.4 \times 10^{-3}\, I_{\rm c}$, about 64 % are blue-only and 36 % are red-only. The number of blue-only profiles exceed red-only ones with a factor two. Additionally, the number of red-only profiles in each amplitude class (a>1%) is by an order of magnitude less than blue-lobe only profiles in the same class. Blue-only profiles showed brighter continuum and line-core intensities, whereas this is not the case for red-only profiles. They also show blueshift in their line-core velocity, i.e., upflow, in contrast to red-only profiles. These findings are consistent with an analytical model proposed by Steiner (2000) who predicted that an upflow in the non-magnetic layer in combination with a hot magnetic layer can produce a blue-only profile. The observed blue-only profiles in our data correspond to line-core and continuum intensities larger than the average quiet Sun along with blueshifted line-core positions.

Chapter 3

The emission of the chromosphere and its temperature stratification

In this chapter, we provide new constraints on the physical models of the solar chromosphere. In Sect. 3.1, we present correlations between the observed properties of the Ca II H line profiles (which mainly forms in the chromosphere) and the physical conditions in the photosphere. Then, in Sect. 3.2, extreme low-activity calcium profiles are presented. We also discuss the importance of our measurements for the semi-empirical description of the solar atmosphere.

3.1 Relation between photospheric magnetic field and chromospheric emission

As explained in Sect. 1.1.1, granulation is the dominant pattern covering the solar surface outside sunspots. Its diameter is 1-2 Mm, much smaller than supergranules with a dimension of $\sim$20–40 Mm. Supergranules show the same pattern as granulation: a horizontal flow from the center towards the boundary of the cell. These large scale convection cells have a mean lifetime of 20 h, much longer than the granular time-scale (some 10 minutes). The boundary of the supergranular cells is where the chromospheric network forms (Fig. 1.5). The network harbors strong magnetic flux concentrations with a magnetic field strength of about 1 kG. In contrast, he interior of the network cells, the inter-network, has much less magnetic field than the network (e.g., Keller et al. 1994).

The chromospheric heating mechanism is one of the main challenges of solar physics (Narain & Ulmschneider 1996; Carlsson et al. 2007, and references therein). The core emission of the Ca II H and K lines is an important source of radiative losses in the chromosphere (Table 1.2). Moreover, this emission is an important tool to study the temperature stratification and the magnetic activity of the outer atmosphere of the Sun and other stars (e.g., Schrijver & Zwaan 2000). Most of the observational studies based on these lines use either the calcium intensity profile (e.g., Cram & Damé 1983; Lites

et al. 1993) or combinations of calcium filtergrams and magnetograms[1] (e.g., Berger & Title 2001). From the observation of the calcium spectrum alone, it is not possible to distinguish between the magnetic and non-magnetic heating components. Combining calcium filtergrams with magnetograms allows to separate those components, but the spectral information is lost. Simultaneous observations that allow to reconstruct the magnetic field and record the spectrum of the Ca II H line are rare (e.g., Lites et al. 1999) and only available at lower spatial resolution. Therefore, it is not surprising that none of the present theories, mechanical and magnetic heating, was confirmed or rejected observationally (De Pontieu et al. 2007; Carlsson et al. 2007; Wedemeyer-Böhm et al. 2007).

Schrijver (1987) studied a sample of late-type stars and introduced the concept of the *basal flux* to separate the non-magnetic heating from the magnetic one. The Sun is not a very active star, with a chromospheric radiative loss on the order of the basal flux for Sun–like stars (Fawzy et al. 2002b). Carlsson & Stein (1997) presented a semi–empirical hydrodynamic model where enhanced chromospheric emission is due to outward propagating acoustic waves. This model was criticized in subsequent investigations (e.g., Kalkofen et al. 1999; Fossum & Carlsson 2005), which was partly due to disagreements on the temperature stratification in higher layers (e.g., Ayres 2002; Wedemeyer-Böhm et al. 2005). In addition, it is not clear whether high- or low-frequency acoustic waves play a dominant role in the energy transport to higher layers (Fawzy et al. 2002a; Jefferies et al. 2006). While there are theoretical indications that the magnetic filling factor discriminates between different regimes of heating (Solanki & Steiner 1990), there is no canonic model reproducing thermal, dynamical and magnetic properties of the solar chromosphere (Judge & Peter 1998; Rutten 1999).

The POLIS spectropolarimeter (Schmidt et al. 2003; Beck et al. 2005b) was introduced in Chapter 2. It records the full Stokes profiles of Fe I 630 nm (photospheric lines) and the intensity profile of the Ca II H line (chromospheric line). With the information on the photospheric magnetic field (POLIS red channel), we separated the contributions of the magnetically and non-magnetically heated component. We used POLIS to address the question of the chromospheric heating mechanism, by comparing properties of network and inter-network in photosphere and chromosphere using a statistical analysis. With the information on the photospheric fields, we separated the contributions of the magnetically and non-magnetically heated components. For the first time, we studied the correlation of the chromospheric emission with the simultaneously measured amplitude/area asymmetry and Stokes-V zero-crossing velocity at the corresponding photospheric position.

Observations and data reduction are explained in Sects. 3.1.1 and 3.1.2. Histograms of the obtained parameters are presented in Sect. 3.1.3. Correlations between the chromospheric and photospheric parameters are addressed in Sect. 3.1.4. The heating contributions are estimated in Sect. 3.1.5. Discussion and conclusions are presented in Sects. 3.1.6 and 3.1.6, respectively. The straylight contamination and calibration uncertainties for the POLIS Ca channel are estimated in Appendix C. An overview of some of these results

[1] A magnetogram is a solar image showing a rough estimate of the longitudinal magnetic field strength. It is based on measurement of the Stokes-V at only a few (sometimes one) wavelength bands.

Table 3.1: Properties of the observed regions in the ITP 2004 campaign. The heliocentric angle of all observed maps is 53°. All the maps are time-series of a piece of network.

Scan No.	Time	scan-steps	area (arcsec^2)
1	09:39:32	81	40.5×47.3
2	09:48:09	111	55.5×47.3
3	10:01:33	41	20.5×47.3
4	10:06:02	51	25.5×47.3
5	10:11:20	51	25.5×47.3
6	10:16;20	51	25.5×47.3
7	10:21:13	51	25.5×47.3
8	10:26:04	51	25.5×47.3
9	10:30:55	51	25.5×47.3
10	10:35:46	51	25.5×47.3
11	10:40:38	51	25.5×47.3
12	10:45:29	51	25.5×47.3
13	10:50:20	51	25.5×47.3

appeared in Rezaei et al. (2006b) while details were published in Rezaei et al. (2007a).

3.1.1 Observations

We observed a network area close to the active region NOAA 10675 on September 27, 2004, with the POLIS (Schmidt et al. 2003; Beck et al. 2005c) instrument at the German VTT in Tenerife. The observations were part of a coordinated observing campaign in the ITP 2004 program[2] (see Sect. 2.1.1 for details of the observations). Here we analyzed a series of thirteen maps of the same network region at a heliocentric angle of 53°, taken during several hours (Table 3.1). We achieved a spatial resolution of around 1 arcsec, estimated from the spatial power spectrum of the intensity maps.

Figure 3.1 displays an overview of one of the thirteen maps after spatial alignment (the whole set of maps is shown in Fig. 2.1). Map (a) shows the Fe I 630 nm continuum intensity normalized to the average quiet Sun intensity. Map (b) shows the Ca II H wing intensity, at a wavelength of 396.490 nm (for a definition of line parameters see Fig. 3.2 and Table 3.2). These two maps were used for the spatial alignment of the red and blue channels. The next two maps (c and d) show the intensities in the outer and inner wings (W1, respectively, W3). The inner wing samples a wavelength band close to the calcium core; hence, it is more influenced by the line-core emission and shows higher contrast of the network than the outer wing. The next map (e) is the H-index, i.e., the intensity of the calcium core integrated over 0.1 nm (cf. Table 3.2). The network features appear broadest and show the highest contrast in this map. The map (f) demonstrates network

[2]The principal investigator of this campaign was Dr. Pit Sütterlin, Utrecht University.

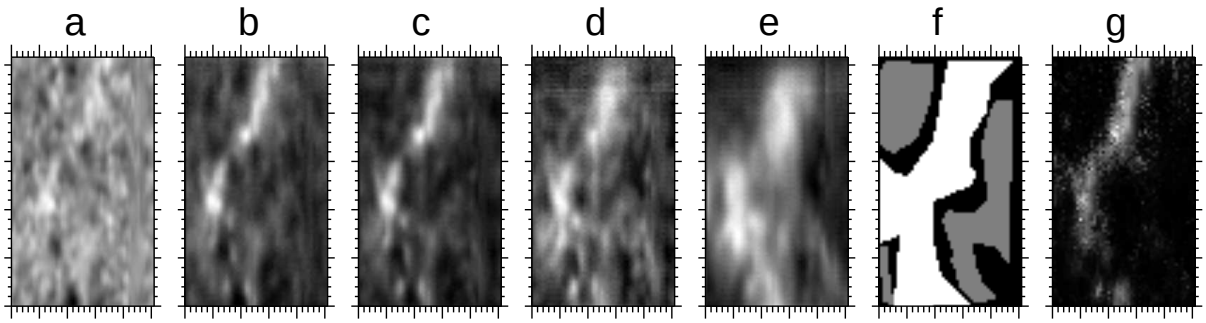

Figure 3.1: *From left to right:* a) the Fe I 630 nm continuum intensity, b) the calcium wing intensity at 396.490 nm which was calibrated to FTS data (Stenflo et al. 1984), c) the outer calcium wing intensity (W1), d) the inner calcium wing intensity (W3), e) the H-index, f) the masks which separate network (white) from the inter-network (gray), and g) the magnetic flux density obtained from the inversion. We did not use the black region between the network and inter-network. Each small tickmark is one arcsec. Note that sampling in x and y directions are different.

Table 3.2: The definition of the characteristic parameters of the Ca II H profile for the peak sample (upper part) and the band sample (lower part) adopted from Cram & Damé (1983) and Lites et al. (1993). Figure 3.2 shows the band definitions graphically. Wavelengths are in nm.

quantity: peak sample	description
H_3	core intensity
H_{2V}	violet emission peak
H_{2r}	red emission peak
V/R	H_{2V}/H_{2r}
emission strength	H_{2V}/H_3
$\lambda(H_3)$	calcium core wavelength
$\lambda(H_{2V})$	H_{2V} wavelength
$\lambda(H_{2r})$	H_{2r} wavelength
quantity: band sample	**description**
H-index	396.849 ± 0.050
H_3	396.849 ± 0.008
H_{2V}	396.833 ± 0.008
H_{2r}	396.865 ± 0.008
W1 (outer wing)	396.632 ± 0.005
W2 (middle wing)	396.713 ± 0.010
W3 (inner wing)	396.774 ± 0.010

and inter-network masks (Sect. 3.1.2). The map (g) shows the magnetic flux density obtained from the spectro-polarimetric data (Sect. 2.1).

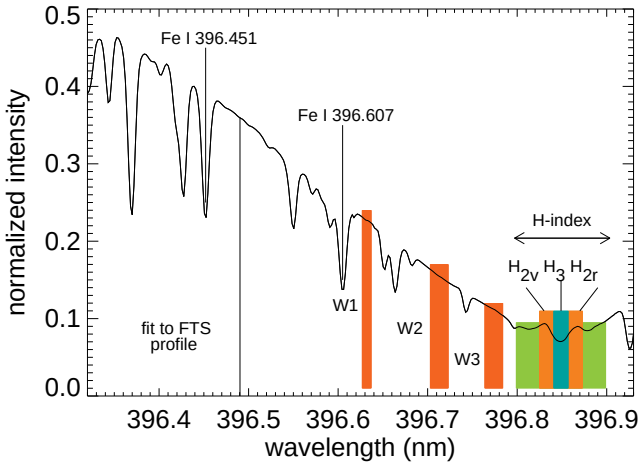

Figure 3.2: Sample averaged calcium profile of one of the maps (the average profile is similar for all other maps). The bands are explained in Table 3.2. Double reversal in the calcium core is seen on the both sides of the core at 396.850 nm. The wing wavelength bands outside spectral lines form in the photosphere while the calcium core and emission peaks form in the chromosphere (cf. Fig. 3.13).

3.1.2 Data analysis

The characteristic parameters of the calcium profile and the Fe I 630 nm line pair are discussed in this subsection. The inversion method used to infer the vector magnetic field was explained in Sect. 2.1.

Definition of network and inter-network

For each map, we created a mask to distinguish between the network and inter-network regions (Fig. 3.1f). This was done manually on the basis of the magnetic flux and the H-index. We did not use the black region in Fig. 3.1f which separates the network from the inter-network. To study structures in these two regions, we define two statistical samples:

The peak sample: Each member of this sample has a regular V profile and a double reversal in the calcium core. For this sample, we study quantities related to the Ca II H emission peaks (Table 3.2, upper part). The number of data points in the network and inter-network are 19509 and 1712, respectively. We emphasize that the few inter-network points in this sample were not distributed uniformly. They usually belong to small-scale magnetic elements surrounded by large areas without magnetic signal above the noise level.

The band sample: All network and inter-network points, marked in the masks, are present in this sample. Since some of these profiles do not have two emission peaks in the calcium core, we use integrated intensities in a fixed spectral range at the core and wing of the calcium profile (Cram & Damé 1983; Lites et al. 1993, Table 3.2). This definition retrieves reasonable chromospheric parameters. In total from all the maps, 24225 points were selected as network (white in Fig. 3.1f) and 20855 as inter-network positions (gray in Fig. 3.1f).

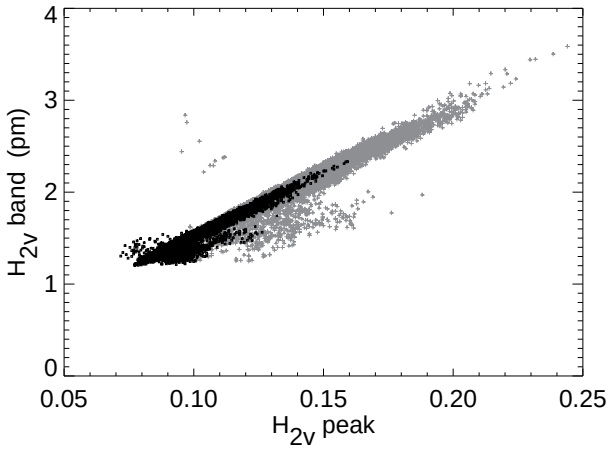

Figure 3.3: Scatter plot of the H_{2V} band vs. peak definition. In the band definition, a fixed spectral range was used. Gray and black show the network and inter-network, respectively. It shows that the two definitions are consistent to each other.

Analysis of Ca II H profiles: We averaged the line profiles over a large area (including network) to obtain an average profile for each map; an example is shown in Fig. 3.2. Then we normalized the intensity at the line wing at 396.490 nm to the FTS profile (Stenflo et al. 1984). The same normalization coefficient was applied to all profiles of the map. Hence, all profiles were normalized to the average continuum intensity. Table 3.2 lists the characteristic parameters we define for each calcium profile:

a) The intensity of the Ca II H core, H_3, and the amplitudes of the emission peaks, H_{2V} and H_{2R}, and their respective positions, λ_{H_3}, $\lambda_{H_{2V}}$, and $\lambda_{H_{2R}}$ (peak sample).

b) Intensities in the outer (W1), middle (W2), and inner line wings (W3), which are integrated over spectral bands with a *fixed* spectral range (band sample).

From these quantities we derive:

1. the ratio of the emission peaks, $V/R = H_{2V}/H_{2R}$, and
2. the emission strength which is the intensity of the violet emission peak divided by the core, H_{2V}/H_3.

The band intensities are defined such that the wavelength intervals are fixed for all the profiles and do not depend on the peak/core positions (Table 3.2, lower part). Figure 3.3 shows a comparison between the H_{2V} parameters derived from the band and peak definitions. The correlation is very strong (also for other peak parameters). Thus, it is justified to use the values from the band sample to improve the statistics for the inter-network.

3.1.3 Histograms of the intensity parameters

The network patches are brighter than the inter-network at all wavelengths: in the core and wing of the Ca II H line and in the Fe I 630 nm continuum. The distributions of the intensity parameters at different wavelengths are shown in Fig. 3.4. Thick and thin curves

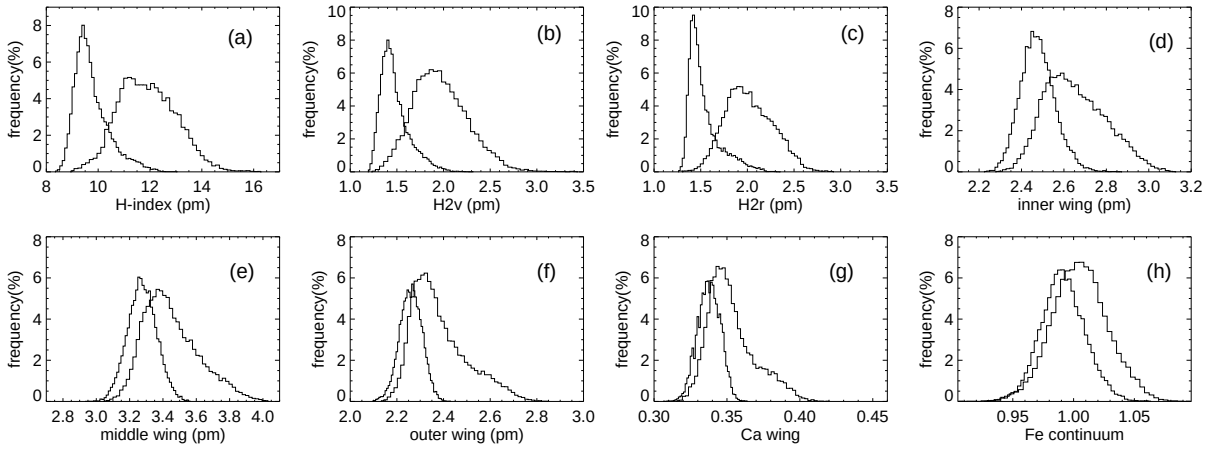

Figure 3.4: Histograms of intensity parameters for the network (thick) and inter-network (thin), using the band sample: *a)* H-index, *b)* H_{2V}, *c)* H_{2R}, *d)* W3 (inner wing intensity), *e)* W2 (middle wing intensity), *f)* W1 (outer wing intensity), *g)* calcium wing intensity at 396.490 nm which was used for normalization (see Fig. 3.2), and *h)* Fe I 630.2 nm normalized continuum intensity (see Table 3.2 for definitions). In all panels, from the red continuum (h) to the calcium core, the network shows brighter structures than the inter-network.

show network and inter-network, respectively. A comparison between the network and inter-network histograms indicated that the calcium core parameters (H-index, H_{2V}, H_{2R}) are more shifted than the wing/continuum intensities (Fig. 3.4a, b, c). In other words, the intensity contrast increases from the continuum toward the wing and peaks at the core. Moreover, the wing intensities show different behaviors due to their respective distances to the core: the closer the selected wavelength band to the core, the larger the shift between network and inter-network distributions. Hence, the histogram of the inner wing intensity (Fig. 3.4d) has a larger shift than the middle and outer wings (Fig. 3.4e and f). The distribution of the Ca II H wing[3] and Fe I 630 nm continuum intensities also show a shift between the network and inter-network: the peak of the distribution in the network is slightly brighter than that in the inter-network in the 396.490 nm and also 630 nm continuum (Fig. 3.4g and h).

3.1.4 Correlations

Correlations between chromospheric quantities: There is a strong correlation between the H-index, H_3, H_{2V}, H_{2R}, and the inner wing intensity (with a correlation coefficient ≥ 0.8, see Fig. 3.5). Therefore, we adopt the H-index as a proxy for the calcium core emission. It is the closest calcium intensity parameter to the widely used filtergrams[4].

[3]Here, wing means the wavelength that was used for the intensity calibration (see Fig. 3.2).

[4]Note that filtergrams, e.g., from DOT (de Wijn et al. 2005) also cover parts of the line wing while we integrate over a band with a width of 0.1 ± 0.001 nm, centered at the line core.

Table 3.3: Correlation coefficients between the band intensities and the H-index (see Fig. 3.2 for definitions) in the network and inter-network using the band sample. The wing correlations in the network are larger than the inter-network.

parameter	network	inter-network
H_3	0.88	0.90
H_{2V}	0.92	0.94
H_{2r}	0.88	0.93
W3	0.77	0.68
W2	0.73	0.53
W1	0.58	0.36

The (V/R) ratio is an indicator for the H_3 line-core position (Rutten & Uitenbroek 1991; Cram & Damé 1983). There is a strong correlation between the (V/R) ratio and $\lambda(H_3)$: the redshifted and blueshifted calcium profiles correspond to (V/R) ratios smaller and larger than one, respectively (Fig. 3.5, lower right panel). The calcium core position is expressed in velocity units for comparison. This does *not* mean that it corresponds to a Doppler shift. We find a similar correlation between the emission strength and the (V/R) ratio: the larger the (V/R) ratio, the larger the emission strength (Fig. 3.5, lower row, second right panel). The correlation between the inner and outer wing intensities and the H-index are shown in the lower panels of Fig. 3.5. While there is a correlation for the outer wing in the network (gray), there is no significant correlation in the inter-network (Table 3.3). We calculated the correlation coefficient between the H-index and all intensities in the line wing to investigate this difference in more details (Table 3.3). In the network, there is a stronger correlation than in the inter-network for all the wing bands considered. Implications of this finding will be discussed in Sect. 3.1.6.

Calcium core emission vs. magnetic flux: The left panel of Fig. 3.6 shows the relation between the photospheric magnetic flux and the chromospheric emission for the network. For lower flux values (< 100 Mx cm^{-2}), there is a clear increase of emission with flux. However, for higher magnetic flux densities, the H-index increases slowly. To reproduce the observed relation, we utilize a power law fit to the data,

$$H = a\,\Phi^b + c, \tag{3.1}$$

where Φ is the absolute magnetic flux density, H is the H-index, a is a constant coefficient, b is the power index, and c is the non-magnetic contribution (see subsection 3.1.5). We used a variable lower threshold of $0, 3, .., 20$ Mx cm^{-2} (cf. Table 3.4) for the fit and neglected all data points with fluxes below this level. We find that the power exponent, b, depends strongly on the threshold. The higher the threshold, the better the fit curve resembles a straight line, as first reported by Skumanich et al. (1975). If we keep all the points, including inter-network, we obtain a value for the power exponent of $b = 0.2$.

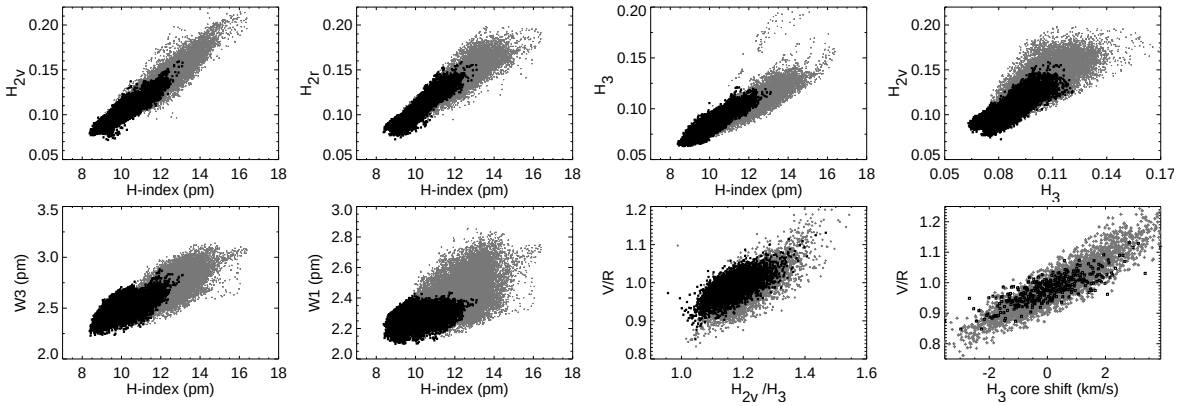

Figure 3.5: *Upper panels, left to right*: Scatter plots of the H_{2V}, H_{2r} and H_3 with H-index, and H_{2V} with H_3 based on the peak sample. *Lower panels, left to right*: Correlation between W_3 and W_1 with the H-index, correlation of the (V/R) ratio with the emission strength and the calcium core position. Gray and black show the network and inter-network, respectively (for abbreviations, see Table 3.2). In the lower right panel, we used binned data to decrease the scatter: each point is average of 25 points.

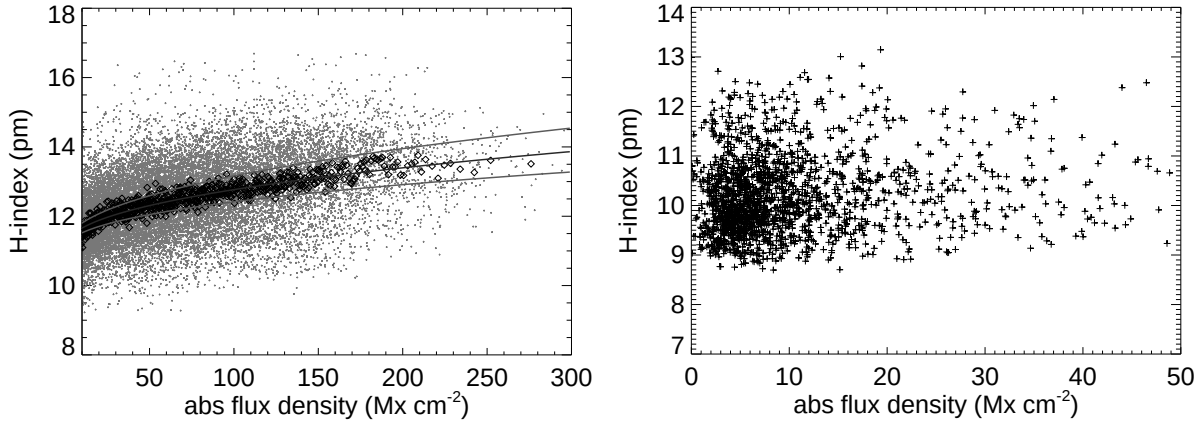

Figure 3.6: *Left panel*: Correlation between the H-index and the absolute magnetic flux density in the network. Gray is the original data and black is the binned data: each point is average of 25 points. The middle curve shows a fit of a power law to the original data (Eq. 3.1), the other two curves give the $\pm 1\sigma$ error range of the fit. There is a variable lower limit in this panel in original data (gray). The upper limit looks independent of the magnetic flux. *Right panel*: There is no correlation between the H-index and the magnetic flux density in inter-network.

The calcium core emission in the inter-network does not correlate with the magnetic flux, at least with the concentrated magnetic field within the Zeeman sensitivity of this observations (Fig. 3.6, right panel). The value of the offset, c, of the fit to the network (Table 3.4) for low magnetic flux densities was around 10 pm, which is consistent with the average H-index value of all the inter-network profiles (10 pm for the peak sample). The

Table 3.4: The parameters of the fit to Eq. 3.1 to the network data. The first column, Φ_0, is the threshold for the magnetic flux density. By increasing the threshold, we avoid the inter-network intrusions. For a comparison to the peak inter-network flux density, see Sect. 2.1

Φ_0 ($\mathrm{Mx\,cm^{-2}}$)	a (pm)	b	c (pm)
0	0.73 ± 0.05	0.28 ± 0.01	10.1 ± 0.1
3	0.71 ± 0.05	0.29 ± 0.01	10.1 ± 0.1
5	0.61 ± 0.04	0.31 ± 0.01	10.3 ± 0.1
10	0.22 ± 0.02	0.45 ± 0.02	11.0 ± 0.1
20	0.14 ± 0.06	0.51 ± 0.06	11.3 ± 0.2

value of the c parameter changes for different thresholds of the flux density (Table 3.4). Implications of this finding for the basal flux will be discussed in Sect. 3.1.6.

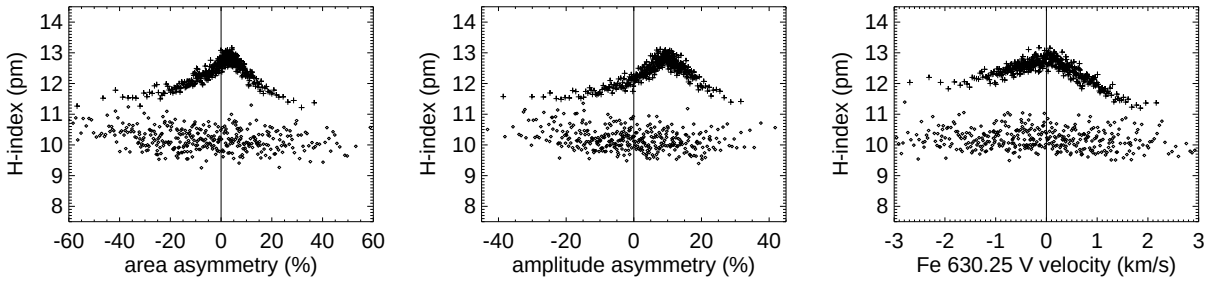

Figure 3.7: Correlation between the H-index and amplitude/area asymmetry and V velocity. Plusses and squares show network and inter-network, respectively. The binning method is similar to Fig. 3.6.

Calcium core emission vs. Stokes-V velocity and asymmetries: The calcium core emission peaks at small positive amplitude/area asymmetry in the network (pluses, Fig. 3.7). This is caused by strong V profiles that show small asymmetries (Fig. 2.4, right panels). The highest H-index in the network corresponds to almost zero Stokes-V zero-crossing velocity. In its diagram (Fig. 3.7), the slope of the left branch (blueshift) is shallower than the right one. Moreover for the strong upflow or downflow in the magnetic atmosphere in the network, the H-index decreases significantly. The H-index in the inter-network does not depend on any parameter of the Stokes-V profile (squares, Fig. 3.7).

Considering the fact that the amplitude and area asymmetries strongly correlate with each other (top left panel, Fig. 2.4), a natural consequence is that the left (right) branch of the scatter plot of the H-index vs. amplitude asymmetry corresponds to the left (right) branch of the scatter plot of the H-index vs. area asymmetry (Fig. 3.7). However, comparing only negative or positive branches of the scatter plots of the H-index vs. V velocity and asymmetries in the network, the left branch in the V velocity *does not*

correspond to the similar branch in the asymmetry plots. The left diagrams in Fig. 3.8 contains only the profiles with a negative Stokes-V zero-crossing velocity, while in the right panels profiles with a negative area asymmetry are shown. A positive Stokes-V zero-crossing velocity may thus correspond to a positive or negative area asymmetry. There is no relation between the amplitude/area asymmetries and the V signal in the inter-network (right panels, Fig. 2.4).

Table 3.5: Fractional distribution of the total H-index, δ, for different magnetic flux thresholds. It shows that a small fraction of the whole emission comes from structures with large magnetic flux densities.

Φ_0 (Mx cm^{-2})	#	δ (%)
4.	38 905	63.7
10.	26 071	44.5
50.	11 190	20.4
100.	4 933	9.2
150.	1 709	3.3
200.	329	0.6

3.1.5 The magnetically and non-magnetically heated components

The H-index includes the H_1 (the minima outside the emission peaks), H_2, and H_3 spectral regions. So its formation height extends from the higher photosphere to the middle chromosphere (see Sec. 3.2). The Ca II H & K lines are one of the main sources of the chromospheric radiative loss (Sect. 1.1.2, Table 1.2). We used the H-index as a proxy for the emission in the low/mid chromosphere, and assumed a linear relation between the H-index and the chromospheric radiative loss. To derive the contribution of magnetic fields to the chromospheric emission, we added the H-index of all points with magnetic flux above a given flux threshold. The *fractional H-index*, δ, is then defined by normalizing this quantity to the total H-index of all points in the field of view[5]:

$$\delta\left(\Phi > \Phi_0\right) = \frac{\sum H \quad (\Phi > \Phi_0)}{\sum H \quad (\text{all maps})}.$$

Table 3.5 lists the fractional H-index in different magnetic flux thresholds. Some 20 % of the total H-index is provided by strong flux concentrations ($\Phi \geq 50$. Mx cm^{-2}) while the remaining 80 % of that is produced by the weak magnetic field and/or field free regions.

The average H-index is 12.0 and 9.8 pm in the network and inter-network, respectively. However, it contains some contributions from the photosphere (outside emission peaks) and a cool chromosphere (without temperature rise)[6]. Therefore, we decomposed the

[5]We used all data points in this part and did not use the mask defined in Sect. 3.1.2.

[6]Cool chromosphere means a radiative equilibrium atmosphere (Sect. 1.1.1).

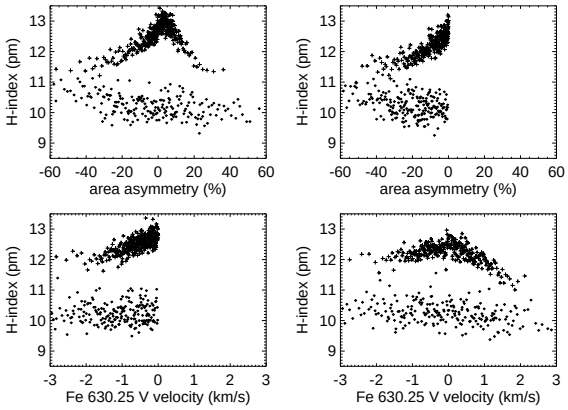

Figure 3.8: Plots of the H-index vs. the area asymmetry (*t*op) and Stokes-V zero-crossing velocity (*b*ottom). In the left column diagrams, only the points with a negative Stokes-V zero-crossing velocity are plotted. In the right panels, only points with a negative area asymmetry are plotted. Pluses and squares show network and inter-network, respectively. Definitions of the H-index and the area asymmetry are shown in Figs. 3.2 and 2.2, respectively.

observed calcium profiles in a *heated* and a *non-heated* component,

$$\mathrm{H_i} = \mathrm{H_{re}} + \mathrm{H_{non}} + \mathrm{H_{str}} \tag{3.2}$$

where $\mathrm{H_i}$ is the average H-index of the inter-network, $\mathrm{H_{re}}$ is the non-heated component of a radiative equilibrium atmosphere, $\mathrm{H_{non}}$ is the non-magnetically heated component, and $\mathrm{H_{str}}$ is the straylight contribution. The non-heated component of the profile originates from the line–wing emission (photosphere) and a cool chromosphere.

We used the Holweger & Müller (1974) model atmosphere to describe those parts of the solar atmosphere that are not affected by any heating process. This model is very similar to a theoretical radiative equilibrium model (see Sect. 1.1.1), but it was not constructed to strictly satisfy this condition. We prefer this semi-empirical model over a theoretical radiative equilibrium model because it results in a slightly better reproduction of the Ca II H line wings. We note, however, that 3D MHD simulations of the solar atmosphere commonly produce regions in the upper photosphere and chromosphere with temperatures significantly lower than in the Holweger-Müller model. These structures, however, are generally so small that their evolution is strongly influenced by their surroundings, so that they cannot serve as a model for those parts of the solar atmosphere that are not influenced by any heating processes. That means that they are not suitable for determining the absolute minimum value of the H-index.

We performed a consistent NLTE radiative transfer computation in plane-parallel geometry, including effects of partial frequency redistribution[7], in order to estimate the non-heated component of the H-index. We added an (almost) isothermal hydrostatic extension up to a height of 2000 km to the model in order to be able to compute the core parts of the Ca II H & K lines. This may seem an arbitrary choice, but considering that the computed intensity is essentially zero at the line core for models with such low

[7]When the scattering is neither completely coherent nor completely incoherent or redistributed, one has partial redistribution. In this situation the photon that is deexcited has some correlation with the photon that excited the atom. In this case, propability of scattering photons from one frequency to another must be accounted for (Rutten 2003; Mihalas 1978).

temperatures in the upper atmosphere, its influence on the H-index is very small. This model atmosphere and the obtained profile (right panel of Fig. 3.12) are similar to the COOLC model of Ayres et al. (1986) and the corresponding profile. We find a value of $H_{re} = 5\,pm$ at disk center. At a heliocentric angle of 53°, the corresponding value is $H_{re} = 5.9\,pm$.

We find an upper limit of $\sim 12\,\%$ for the straylight contamination of the observed profiles (Appendix C). Therefore, we decomposed the average H-index in the inter-network ($H_i = 9.8\,pm$) to obtain the non-magnetically heated component, H_{non}:

$$H_{non} = H_i - H_{re} - H_{str} \tag{3.3}$$

$$H_{non} = 9.8\,(\pm 1.0) - 5.9\,\left(^{+0.6}_{-0.0}\right) - 1.1\,(\pm 0.1) = 2.8\,\left(^{+1.1}_{-1.0}\right).$$

We find an average non-magnetic heating of $H_{non} \sim 2.8 \pm 1.1\,pm$. To decompose the average H-index of the network, we also considered the magnetically heated component, H_{mag}, and used the same method:

$$H_{mag} = H_n - H_{re} - H_{non} - H_{str}. \tag{3.4}$$

where the magnetically heated contribution is the first term in Eq. 3.1. Assuming a similar non-magnetically heated contribution, H_{non}, for the network as in the inter-network (which was supported by observations, e.g., Schrijver 1987, 1995), we find an average magnetically heated component of about $H_{mag} \sim 1.9 \pm 1.4\,pm$, which is consistent with the difference between the mean H-index in the network and inter-network. Thus, the non-magnetically heated component has a larger contribution to the observed H-index than magnetically heated one, both in the network and inter-network. Our error estimates in Appendix C show that the uncertainties of the measurements do not affect this result.

3.1.6 Chromospheric structures in the presence of magnetic field

Thermal coupling: All intensity parameters, from the calcium core to the Fe I 630 nm continuum, show different distributions in the network and inter-network: the network patches are brighter not only at all observed wavelengths of the calcium profile, but also in the 630 nm continuum (Figs. 2.4 and 3.4). As noted by Cram & Damé (1983), this implies that the temperature fluctuations are spatially coherent between the photosphere and the lower chromosphere. This coherent intensity increase is presumably due to the fact that the optical depth scale is shifted downwards in the evacuated magnetic part of the atmosphere (network).

The correlation between the inner wing intensity and H-index is strong, both in the network and inter-network (Table 3.3, Fig. 3.5). However, the correlation between the outer wing intensity and the H-index is significant only in the network. This indicates that the height range of the thermal coupling between the photosphere and low/mid chromosphere increases in presence of a magnetic field.

H-index vs. magnetic flux: The amount of energy deposited in the network depends on the magnetic flux density. To reproduce the dependence of calcium core emission on the magnetic flux, we used a power law function (Eq. 3.1). We find that the exponent derived strongly depends on the inclusion (or exclusion) of the weakest fluxes. We obtain a power exponent, b, of about 0.3, which is smaller than the values given by Schrijver et al. (1989) and Harvey & White (1999). We ascribe the difference to the higher quality of our data set: better spatial resolution, a lower detection limit for magnetic signals, an accurate estimate of the magnetic flux due to the inversion of vector polarimetric data instead of a magnetogram, and unlike these authors, we did not consider an assumption for the background component prior to the fit. Instead, we kept it as a free parameter. In this way, we find a background component close to the mean H-index of the inter-network for the weakest flux concentrations.

The rate of increase of the chromospheric emission vs. magnetic flux reduces for strong magnetic flux densities. This implies that for large flux concentrations, either the filling factor or the magnetic field strength saturates. There are indications that it is the filling factor: the available space is completely filled by expanding flux tubes (Hammer 1987; Saar 1996; Schrijver et al. 1996). There is an upper limit for the chromospheric emission, independent of the magnetic flux, as seen in the left panel of Fig. 3.6. In addition, a lower limit of the chromospheric emission also exists. In the inter-network, no relation between emission and the photospheric fields is found (Figs. 3.6 and 3.7). The average value of the H-index in the inter-network of around 10 pm corresponds to the offset, c, Eq. 3.1. This reflects a constant contribution to the H-index which is present even without photospheric magnetic flux, in agreement with Schrijver (1987, 1995) who argued that the basal flux does not depend on the magnetic activity. The basal flux contains two components: the non-heated (cf. Sect. 3.1.5) and the non-magnetically heated contributions. The non-heated contribution depends on the temperature stratification, so the non-magnetically heated component has an inverse dependence on the temperature stratification.

Figure 3.6 (left panel) shows that there is a variable lower limit for the H-index versus the magnetic flux density. In contrast, the upper limit is less clearly defined, and would be in agreement with a constant maximum value independent of the amount of the magnetic flux. There are also similar behaviors for the upper and lower limits in the scatter plots of the H_3, H_{2V}, and H_{2R} versus the magnetic flux density. This is similar to upper and lower limits of the basal flux of stars vs. the color (B-V) where the lower boundary changes but the upper one is almost constant (Fawzy et al. 2002b, their Fig. 2). The situation for the inter-network is different: both the upper and lower limits are independent of the magnetic flux density. Better spatial resolution and detection limit for polarization signal is required to double check if this is true.

Decomposing the Ca II H profile: We interpret the solar Ca II H line profile as the superposition of a cool chromospheric profile, the heated component and straylight components. Oranje (1983) first applied this method to reproduce different observed Ca II K profiles from two "basic" profiles. Later, Solanki et al. (1991) used the same idea to decompose the observed profiles by a combination of two theoretically calculated profiles.

Our one-dimensional NLTE radiative transfer calculations reveals that the H-index of a cool chromosphere is about 5.9 pm. Since the chromospheric emission of the Sun as a star is slightly above the minimum among the Sun-like stars (Schrijver & Zwaan 2000), the average quiet Sun profile contains a heated component. Subtraction of the cool chromospheric component from the measured H-index (along with straylight considerations) led to an estimation of the *pure* non-magnetically and magnetically heated components in the measured H-index. The non-magnetically heated component is almost 50 % larger than the magnetically heated component. The presence of a significant non-heated contribution in the H-index indicates that not all of the chromospheric emission emerges from a *hot* chromosphere, in contrast to findings from, e.g., Kalkofen et al. (1999). The minimum heated component in a calcium profile provides evidence how cool the chromosphere may be (e.g., Wedemeyer-Böhm et al. 2005). Moreover, it favors theories in which the non-magnetic heating plays the dominant role in the chromospheric heating (Fawzy et al. 2002a).

The fact that the non-magnetic chromospheric heating contributes significantly to the chromospheric energy balance is also found in the relative contributions of mainly field-free inter-network and network areas to the total emission in the field of view. Magnetic flux densities above $50\,\mathrm{Mx\,cm^{-2}}$ provide only 20 % to the total emission, which is also seen in the ratio of the mean H-index in the network and inter-network, $12.0\,/\,9.8 \approx 1.2$ (Table 3.5) .

Uncertainties: The main uncertainty in the non-magnetically and magnetically heated components is the presence of some heating in our cool chromosphere profile. The Holweger & Müller (1974) model atmosphere is close to an atmosphere in radiative equilibrium without non-magnetic or magnetic heating, so no heated component (cf. Sect. 3.1.5) is expected to be found on its calcium profile. Since there is no general agreement how cool the chromosphere may be (e.g., Kalkofen et al. 1999; Ayres 2002), the best answer would be to use the observed calcium profile with the lowest H-index. However, Solanki et al. (1991) concluded that it is not possible to observe a low activity profile as presented by the COOLC model of Ayres et al. (1986), which is similar to the one employed by us on base of the Holweger & Müller (1974) model atmosphere. Thus, our cool profile can well serve as lower limit of the non-heated contribution to the H-index. Note that a larger value for $\mathrm{H_{re}}$ would increase the contribution of the magnetically heated component, leading to a larger fractional contribution for the magnetically heated to the total heated component.

There are some mixed polarity fields below our polarimetric detection limit and spatial resolution which may influence the ratio of the magnetically heated to the non-magnetically heated component. Discovery of the ubiquitous horizontal magnetic field everywhere on the solar surface by Lites et al. (2008) opened new questions on the real estimate and role of the magnetic field.

H-index vs. Stokes-V asymmetries: From the relations of the chromospheric emission to quantities of the photospheric magnetic field in the network, we find that the chromospheric emission peaks at small positive values of the Stokes-V asymmetries and

at zero Stokes-V velocity (Fig. 2.3). It reflects the histograms of the respective photospheric field quantities which show similar distributions even at disk center (e.g., Sigwarth et al. 1999a). However, in combination with the dependence of the emission on the flux density it is inferred that the stronger flux concentrations mainly show small material flows along with non-zero asymmetries.

The magnetically heated component is related to Stokes-V profiles with non-zero area and amplitude asymmetries (Figs. 2.3 and 3.7). A possible explanation for this finding would be the absorption of upward propagating acoustic waves, generated by the turbulent convection, by the inclined fields of expanding flux tubes (Beck et al. 2008). This would imply that the energy is deposited at the outer boundary or in the canopy of flux concentrations rather than in the central, more vertical, part. It is mainly because the non-magnetic cut-off frequency (Sect. 1.1.2) is lowered at the boundary of the flux tubes, where the field lines are inclined. This was first predicted by Suematsu (1990) and recently achieved some observational support (Hansteen et al. 2006; Jefferies et al. 2006). Figure 3.7 indicates that the maximum observed H-index has non-zero V asymmetry. These asymmetric V profiles are consistent with the case when the LOS passes through the canopy of a magnetic element or through a flux tube axis (positive and negative asymmetries respectively, Steiner 1999). Therefore our finding supports Suematsu (1990).

Conclusion: There is no correlation between the H-index and magnetic field parameters in the inter-network. Therefore, we conclude that the magnetic field has a negligible role in the chromospheric heating in the inter-network. On the other hand, the H-index is a power law function of the magnetic flux density in the network with a power index of 0.3. The average H-indices observed in the network and inter-network are $\sim$10 and 12 pm, respectively. We find a non–magnetic component in the network (based on Eq. 3.1) of about 10 pm which shows the consistency of our analysis: the non-magnetic part of the network H-index is equal to the H-index of the inter-network.

A NLTE radiative transfer calculation, using the Holweger–Müller model atmosphere, indicates that the non-heated component of the H-index, emerging from a cool chromosphere, is about 5.9 pm. Comparison of this non-heated component and the average H-index in the inter-network has two implications: a) some of the observed chromospheric emission does not originate from a hot chromosphere, and b) the non-magnetically heated component is about 50 % larger than the magnetically heated component. From this, we conclude that the non-magnetically heated component has a larger contribution in the chromospheric radiative loss than the magnetically heated component, both in the network and inter-network.

In our statistical ensemble, spatial positions with strong magnetic flux contribute about 20 % of the total H-index. Correlations and histograms of the different intensity bands in the Ca II H spectrum indicates that above a magnetic threshold, photosphere and low/mid chromosphere are thermally coupled. Moreover, our findings are consistent with the idea that the energy transfer in a flux tube has a skin effect: the energy transfer is more efficient in the flux tube boundary (canopy) than at its center (axis).

3.2 Reversal-free Ca II H profiles: a challenge for solar chromosphere modeling in quiet inter-network

Solar model atmospheres are built to reproduce the observed intensity spectrum of the Sun in continuum windows and selected lines (e.g., the series of models initiated by Vernazza et al. 1981). These models rely on temporally and spatially averaged spectra. Hence, they provide information about the average properties of the physical parameters in the solar atmosphere (Linsky & Avrett 1970). At high spatial, spectral, and temporal resolution, differences from the average profiles arise, leading to different interpretations of the atmospheric stratification. In this context, there is no general agreement on the temperature stratification in the solar chromosphere. This is closely related to the fundamental problem of the heating mechanisms in the chromosphere (Sect. 1.1.2). Carlsson & Stein (1994, 1997) proposed that apart from short-lived heating episodes in the chromosphere its time-averaged temperature stratification is monotonically decreasing with geometrical height. As noted by Carlsson et al. (1997), there are disagreements between this model and Solar Ultraviolet Measurements of Emitted Radiation (SUMER) data. Moreover, the cool model was criticized by Kalkofen et al. (1999) who argued that the chromosphere is always hot and can never reach such a low activity state as proposed by Carlsson & Stein. On the other hand, Ayres (2002) challenged the arguments of Kalkofen et al. based on observations of CO lines at the solar limb. The results of the CO observations are supported by three-dimensional MHD simulations that suggests very cool structures in the upper atmosphere and implies a thermally bifurcated medium in non-magnetic regions (Wedemeyer-Böhm et al. 2004, 2005; Scott et al. 2006). Recently, Avrett (2007) suggested that it is possible to reproduce a wide range of continuum and line intensities with a temperature stratification within 400 K of the semi-empirical models (Fontenla et al. 2006, and references therein). He concluded that "...these results appear to conflict with dynamical models that predict time variation of 1000 K or more in the chromosphere...".

In this section, we comment on both full-time hot and dynamic models, based on the lowest intensity profiles observed. We present observations and data reduction in Sect. 3.2.1. Then, we try to reproduce the observed reversal-free calcium profiles (i.e., profiles without emission peaks) by synthesizing line profiles from a variety of model atmospheres using a NLTE radiative transfer code (Sects. 3.2.2 and 3.2.3). The discussion and conclusion appear in Sect. 3.2.4.

3.2.1 Observations and data analysis

A quiet Sun area close to disk center ($\cos\theta = 0.99$) was observed at the German VTT in Tenerife, July 07, 2006. The good and stable seeing condition during the observation and the KAOS (von der Lühe et al. 2003) provided high spatial resolution in the calcium profiles, leading to a collection of different structures observed in the quiet Sun. We used an integration time of 4.8 s and achieved a spatial resolution of 1 arcsec. Details of the observation appeared in Sects. 2.2 and 3.1.

The Ca II H intensity profile and Stokes vector profiles of the visible neutral iron lines

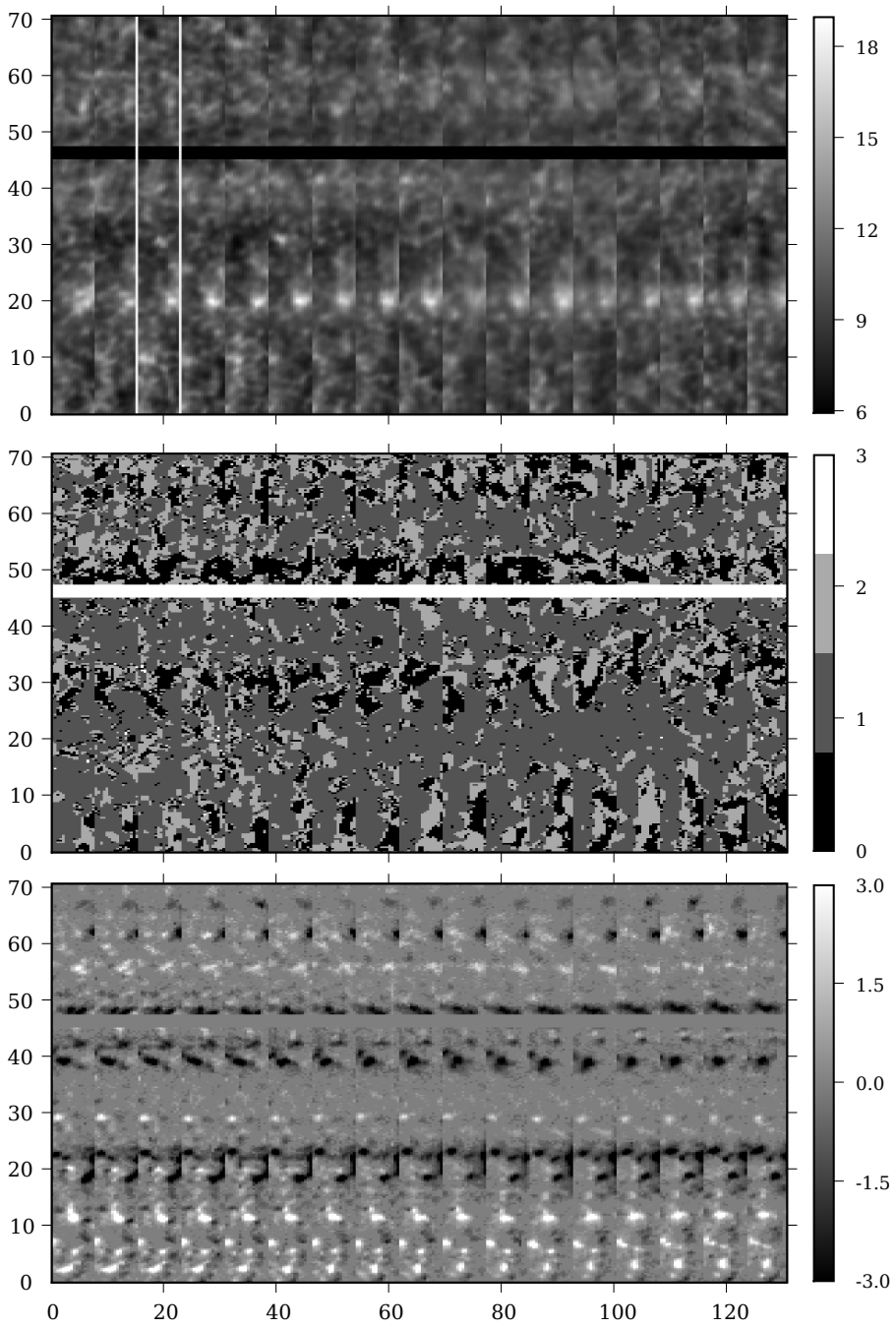

Figure 3.9: Maps of the observed area on July 07, 2006. *Top:* H-index in pm; *middle:* profile type. It is coded as follows: 0: reversal-free; 1: normal; 2: asymmetric; 3: other types. *Bottom:* V_{tot}, which is a measure of the net vertical magnetic flux density (Lites et al. 1999) in arbitrary units. The x-axis shows both scanning direction and time (width of a single map is eight arcsec). The y-axis is the slit direction. Both axes are in arcsec. Only 17 out of 40 scans are shown here. The time duration per scan was about 100 s.

Table 3.6: Classification of the Ca II H line profiles in July 07, 2006 data.

profile type	#	percent	description
absorption	33389	21	one central minimum only
normal	80566	51	two maxima
asymmetric	43343	28	one maximum, central minimum
umbral	10	$\ll 1$	one central maximum only
3-lobe	65	$\ll 1$	three emission peaks

at 630.15 nm, and 630.25 nm were observed with the blue and red channels of the POLIS (Schmidt et al. 2003; Beck et al. 2005c). The overall properties of the observed time-series are shown in Fig. 3.9 concatenated to a single map. The H-index, which is the integral of the normalized calcium profile within 0.1 nm around the core, is shown in the top panel (for definitions of the H-index, V and R band intensities, see Table 3.2). The middle panel shows the profile type, that is coded as follows: [0] reversal-free, [1] normal (with two emission peaks), [2] asymmetric (with only one emission peak), and [3] other types. The bottom panel of Fig. 3.9 shows V_{tot} (Eq. 2.3) which is a measure of the signed magnetic flux (Lites et al. 1999). It is immediately seen that reversal-free profiles are absent in the vicinity of network elements ($y \sim 20$ arcsec in Fig. 3.9). The top row of Fig. 3.10 shows three profiles belonging to different activity levels in the quiet Sun. The left profile has two red emission peaks, the middle profile shows virtually no violet emission peak and the right profile shows a strong violet and a weak red emission peak ($V/R > 2.1$). The gray profile is the average of a few thousand profiles (cell interior and boundary) with an H-index of 10.1 pm. An alternative way to measure the asymmetry of the two emission peaks is dividing the peak values rather than band integrated intensities (Rezaei et al. 2007a). In very asymmetric cases, i.e., where there is only a large violet peak, we can easily achieve a large V/R ratio with band definitions whereas the peak ratio is undefined. Double reversal calcium profiles in old observations with lower spatial resolution do not show extreme values for the ratio of the peaks. It requires both high spatial and temporal resolution and large signal to noise ratio. The maximum and minimum V/R (peak) ratio in our data set are 2.2 and 0.5 (top right and middle panels, Fig. 3.10). The importance of using peak values instead of bands is that the formation height of different wavelengths in the band can differ by more than one Mm (see Fig. 3.13 and the left panel of Fig. 3.14). The bottom panels of Fig. 3.10 show calcium profiles observed in absolutely quiet Sun regions. There is no emission peak or bulge in the core of these profiles. In the bottom row of Fig. 3.10, the left profile has the same wing intensity as the average profile (gray), while the middle and right profiles show lower and higher wing intensities than the average profile, respectively. Note that the reversal-free profiles usually have a V/R ratio very close to one, i.e., they are symmetric (check values in the bottom panels of Fig. 3.10). These reversal-free profiles were called absorption profiles by Grossman-Doerth et al. (1974). They rightly concluded that the source function of the

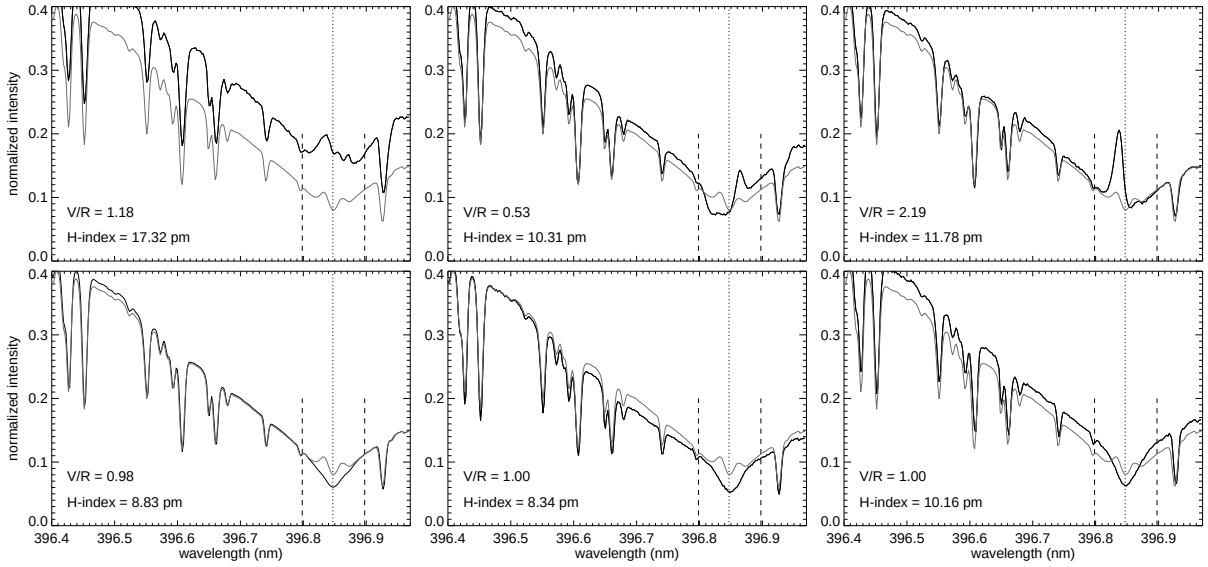

Figure 3.10: Examples of single calcium profiles with drastically different properties observed in the quiet Sun. The gray profile is the average of a few thousands profiles (cell interior and boundary). *Top left:* a profile with three emission peaks. *Top middle:* a very asymmetric profile with only a red emission peak. *Top right:* a very asymmetric profile with two emission peaks. *Bottom:* three reversal-free profiles. Note the level of the wing intensity with respect to the wing of the average profile. The dashed lines show a distance of $\pm\,0.05$ nm from the average calcium core, indicated by a vertical dotted line. The bottom left profile is an average of 59 reversal-free profiles while the other panels show single profiles. Except for the top middle and right panels, the V/R ratio was calculated using bands.

calcium line then shows negligible enhancement in the atmospheric layers where the line forms. An emission bulge existed in the minimum profile of Cram & Damé (1983, their Fig. 2) while this is not the case in the bottom panel, Fig. 3.10. This difference means that our reversal-free profiles present a new minimum state for the observed Ca II H profiles. The high spatial and temporal resolution of our data enabled us to find more extreme cases than in previous studies (e.g., Cram & Damé 1983).

Statistics: In this thesis, we present the first statistical analysis of reversal-free Ca II H line profiles. Statistics of all profiles (network and inter-network) is listed in Table 3.6. We excluded the range $y = 15 - 25$ arcsec in our maps because that clearly contains network. Then we performed a statistical analysis to check how often the reversal-free profiles occur. The inter-network sample had some 129 000 profiles. We checked the existence of the emission peaks by analyzing the profile shape. Among the profiles that had no emission peaks, some show a strong H-index as in the left panel of Fig. 3.11; but others, like the bottom panels of Fig. 3.10, show a rather normal wing intensity and a dark core. We find that 25 % of all profiles do not show any emission peak: 16 % had an H-index larger than 9 pm, 8 % between 8 and 9 pm, and 1 % below 8 pm. Examples of

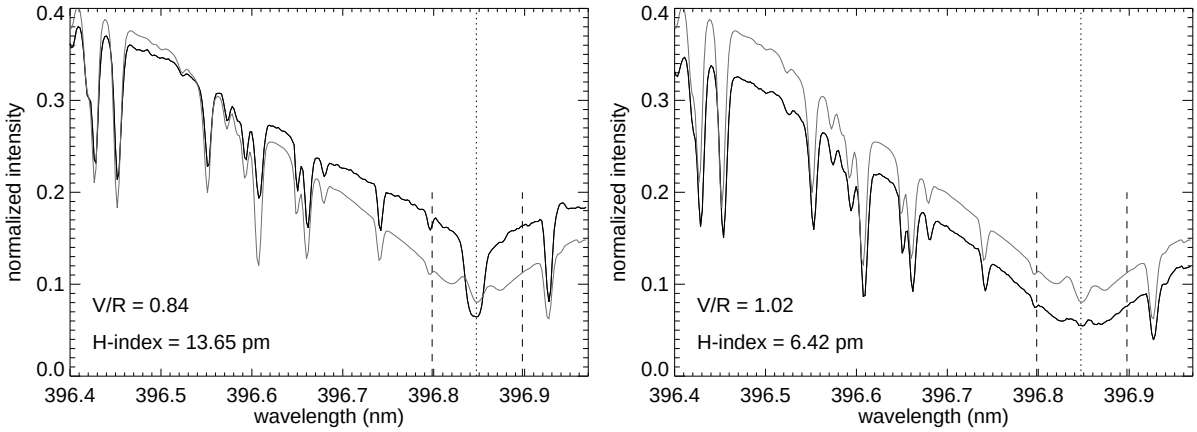

Figure 3.11: These two examples show that the integrated intensity close to the core is not a reliable criterion to separate reversal-free profiles from profiles with emission peaks. Positions of the upper and lower profile are (18.7, 30.5) and (32.6, 30.2) in Fig. 3.9, respectively. Other parameters are similar to Fig. 3.10.

calcium profiles with low H-index and no emission peak are shown in the lower panels of Fig. 3.10. A majority of these 25 % showed a tiny bulge at the position of the emission peaks.

It is worthwhile to note that the H-index alone is not a reliable parameter for identifying the reversal-free profiles, as is demonstrated in Fig. 3.11. The left profile shows no emission peaks, but the wing intensities suggest a hotter upper photosphere and a lower photospheric temperature gradient; the right profile has two clear emission peaks, but the wing intensities demand a cooler upper photosphere. Consequently, the H-index of the right profile is less than half of the left profile. This is in accordance with the fact that all three panels of Fig. 3.10 (bottom row) show reversal-free profiles with an H-index larger than 8 pm.

Besides the 25 % fraction of reversal-free profiles in our sample, 46 % of all profiles show a double reversal, most of them with a stronger violet peak. The remaining 29 % of all inter-network profiles show just one emission peak, again with a majority of stronger violet emission peaks, similar to previous studies (e.g., Cram & Damé 1983).

3.2.2 Synthetic calcium profiles

To reproduce the reversal-free profiles we computed synthetic Ca II H profiles by means of the NLTE radiative transfer code RH, developed by Uitenbroek (2001). The atomic model is the standard 5-level plus continuum model that is included with the RH code; apart from minor atomic data updates this model is essentially equal to the one used by Uitenbroek (1989), which in turn dates back to Shine & Linsky (1974) and references therein. As shown by Uitenbroek (1989), partial frequency redistribution of the photons in both Ca II H and K needs to be taken into account, whereas assuming complete redistribution in the lines of the infrared triplet has no noticeable influence on the profiles of H and K.

Partial frequency redistribution makes the line source functions wavelength dependent and significantly reduces the strength of the H_2 and K_2 emission w.r.t. the common complete redistribution case. Note that since we only dealed with static atmosphere models, it sufficed to use angle-averaged partial frequency redistribution. Furthermore, Solanki et al. (1991) found that the width of the K_2 (and implicitly H_2) peaks correlates with the microturbulent velocities in the chromosphere. Zero microturbulence produces stronger and narrower peaks whereas the microturbulence values given with semi-empirical 1D solar models typically result in shallower, wider peaks. Microturbulence is a parameter that is used in particular in 1D radiative transfer modeling to account for the influence of spatially unresolved velocities on the line profiles. For 2D and 3D dynamic models it is generally not needed.

Since full 2D or 3D (dynamic) radiative transfer modeling is beyond current computational resources, we used static 1D plane-parallel models to synthesize Ca II H line profiles, even though the structures that we observe are so small that we expected lateral radiative transfer to play a role. In addition, we used the microturbulence values as specified with the semi-empirical models we employed, even though we did not know anything about the unresolved small-scale velocities in the observed features. Synthetic profiles from semi-empirical 1D quiet-Sun models with non-zero microturbulence tend to have H_2-peaks that are generally stronger than observed; using zero microturbulence, as one would do if the structure to be modeled were completely resolved, would only widen this discrepancy. Since we could not be sure that the structure is completely resolved in the observations, and also because we expected that radiative interaction with the environment would lead to broadening of the H_2-peaks, we decided not to change the microturbulent velocities. Note that the latter is not an observational effect, but solely due to scattering of line photons in the solar atmosphere.

As model atmospheres, we used four semi-empirical models: FALC (quiet Sun) and FALA (inter-network) from Fontenla et al. (1999, 2006); the Holweger-Müller atmosphere (Holweger & Müller 1974), which is very similar to a theoretical radiative equilibrium model, but not constructed to strictly satisfy this condition; and the recent C6 quiet Sun model atmosphere, provided in advance of publication (Avrett & Loeser 2008, where this model is now called C7). The left panel of Fig. 3.12 shows the temperature stratification of these four model atmospheres. All of the models, except the Holweger-Müller model, show a chromospheric temperature rise at different heights in the atmosphere. The Holweger-Müller model has a monotonically-decreasing temperature stratification with an artificial extension with constant slope (almost isothermal). The extension was required to include the formation height of the Ca II resonance lines. The synthesized calcium profiles are shown in the right panel of Fig. 3.12. For comparison, the reversal-free profile from the bottom left panel of Fig. 3.10 is overplotted in gray.

For all synthesized profiles, except the one derived from the Holweger-Müller model, there are well-defined emission peaks at the H_{2v} and H_{2r} wavelengths. All the synthetic profiles are significantly different from the observed reversal-free profiles. It might suggest that, e.g., the temperature rise in the chromosphere is either shifted to higher layers, or the temperature gradient is not as steep as proposed by, for example, the C6 model. For

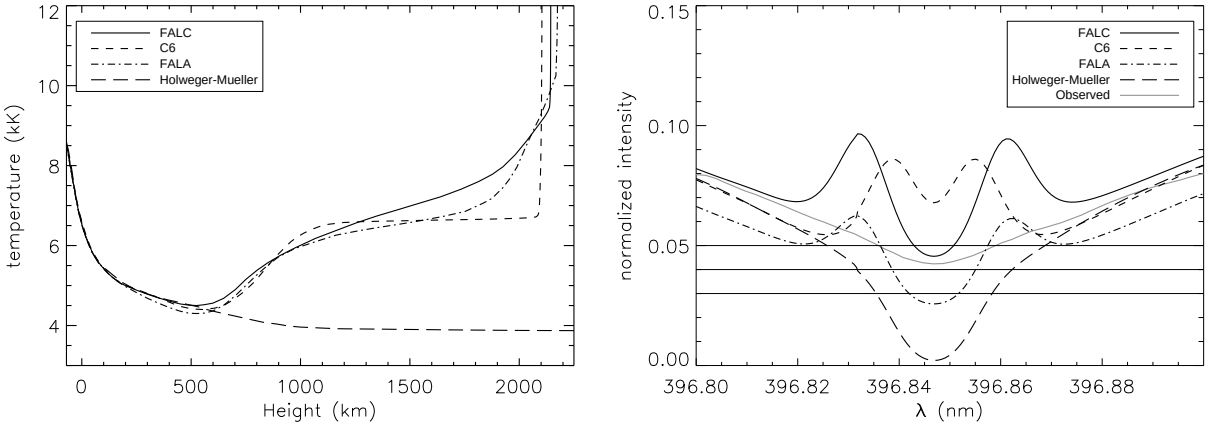

Figure 3.12: *Left:* Stratification of the temperature in the FALA, FALC, Holweger-Müller, and C6 model atmospheres. *Right:* Resulting calcium profiles. Except for the Holweger-Müller model atmosphere, which does not show a temperature rise, all model atmospheres result in two emission peaks. We set the nearby pseudo-continuum of the FALC profile to unity and use this normalization factor for all synthetic profiles. The observed reversal-free profile in the bottom left panel of Fig. 3.10 is shown in gray. All synthetic profiles convolved to the spectral resolution of the observed spectra; scattered light removed from the observed profiles.

a very inhomogeneous model atmosphere, the region with high emission may be very "patchy".

The new chromospheric model C6, as well as FALC, includes a chromospheric temperature rise. If one considers a velocity stratification in the atmosphere, it will be possible to reproduce a variety of asymmetric calcium profiles (e.g., Heasley 1975). However, it is not trivial to diminish both emission peaks at the same time to reproduce a reversal-free profile. As seen in Fig. 3.12, none of the applied models with a chromospheric temperature rise produced a reversal-free calcium profile. While the C6, FALA, and FALC models look too hot, with strong emission peaks, the Holweger-Müller model fails due to its very deep calcium core. The dynamical models of Carlsson & Stein (1994, 1997) and Rammacher & Cuntz (2005) have episodes (significantly) cooler than the Holweger-Müller model with correspondingly lower line core intensities (Uitenbroek 2002; Rammacher 2005). It should be remembered, however, that the chromospheric radiative transfer in those simulations is not "consistent": important cooling agents were not represented at all and deviations from various equilibrium states were ignored.

3.2.3 Modified model atmospheres

Given the large deviations between all synthetic profiles of the Ca II H line and the observed reversal-free profiles, it was tempting to try to obtain a closer match to the observed profiles by making changes to one of the model atmospheres, specifically to the FALC model. This procedure was by no means unique and given that we employed static

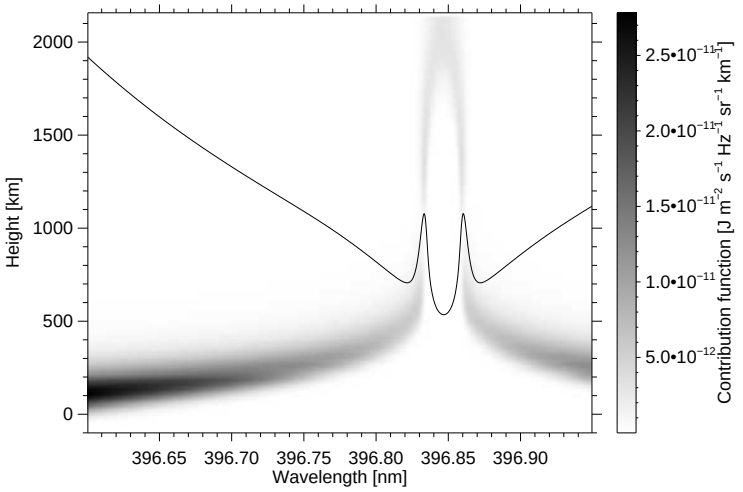

Figure 3.13: Intensity contribution function for the inner part of the Ca II H line computed for the FALC model. The thin line is the calcium profile of the model. It shows that the wing wavelengths form in a narrow height range while the emission peaks have a wide formation height (Courtesy J. Bruls, KIS).

models it was not clear whether we could reproduce the observed profiles that resulted from the dynamic and highly-structured solar atmosphere. We could end up adjusting all atmospheric parameters and still not get a satisfactory match. Instead, we chose to adjust only the FALC temperature in a very schematic way to get at least an indication which changes might be needed. We stress, however, that these modified models are no longer consistent since only the temperature was changed and all other parameters remained unchanged. They may not reproduce observed profiles of other lines. From the NLTE radiative transfer computations we know that the monochromatic source function follows the local temperature fairly well throughout most of the Ca II H line, even though it is a strong, scattering line. This means that a naive change of the temperature stratification at some height translates into a change in emergent intensity for those parts of the line that form at that particular height. The intensity contribution function for the Ca II H line (Fig. 3.13) indicates that the formation range for any given wavelength is very limited, which means that temperature corrections at a given height will lead to predictable line profile changes. This procedure should work particularly well for the line wings up to the H_1 minima, where the source function is very close to LTE, and for the very core, whose source function drops way below the Planck function in a predictable way. However, even though the formation range at any wavelength within the H_2 peaks is narrow, the wide range of formation heights spanned by these peaks as a whole necessitates temperature changes over a wide height range to suppress the emission peaks completely. In addition, we need a rather high temperature in the upper chromosphere to obtain a reasonable core intensity; for that reason we use the FALC model as starting point. This means that we may only change the temperature structure in the lower and middle chromosphere: we created models with the temperature minimum region isothermally extended upward to column mass values of $10^{-3.0}$ (ISO_30), $10^{-3.5}$ (ISO_35), and $10^{-4.0}$ (ISO_40), followed by a linear $T(\log m)$ relation up to a column mass of $m = 2 \cdot 10^{-5}\,\mathrm{g\,cm^{-2}}$, above which the original FALC temperatures are retained (Fig. 3.14, left panel). The lower temperature in

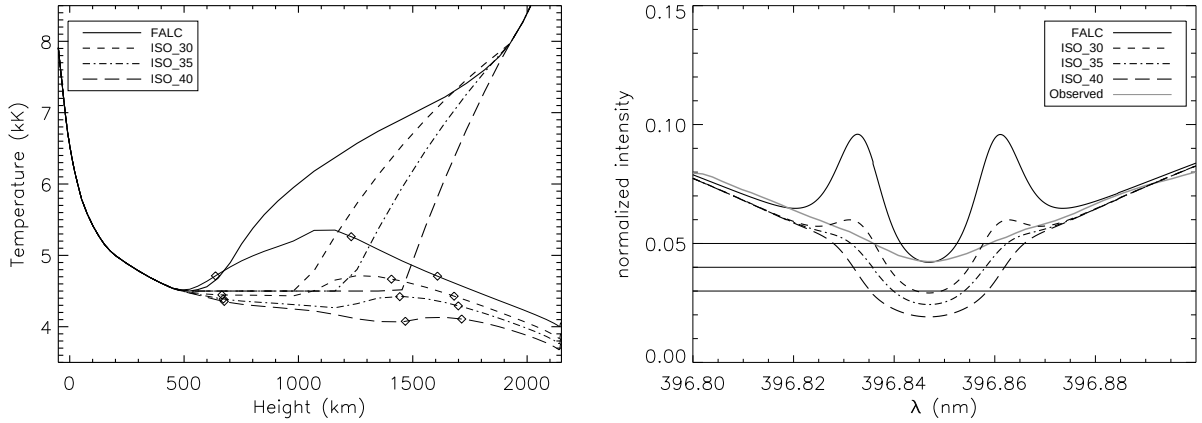

Figure 3.14: *Left:* Stratification of the temperature in the FALC model atmosphere and three modified versions of that. The thin curves represent the monochromatic source functions of these models at $\Delta\lambda = -0.014$ nm from line center. The diamonds (from left to right on each curve) represent the location of $\tau_\nu = 1$ for $\Delta\lambda = -0.016$, $\Delta\lambda = -0.014$, and $\Delta\lambda = -0.012$ nm. The source function is similar for all three wavelengths, so that we restrict to just one source function curve per model. *Right:* Resulting calcium profiles of the mentioned models convolved to the spectral resolution of POLIS. The ISO_30 profile is much closer to the observed reversal-free profile than the FALC model.

the height range about 600-1900 km weakened the emission peaks, while the temperature rise in the higher layers prevented a very deep calcium core. The profiles (Fig. 3.14, right panel) suggest that a temperature rise shifted to larger heights is a step toward producing a reversal-free profile.

3.2.4 Chromospheric temperature stratification

We find that a quarter of all observed profiles are reversal-free profiles. We observed reversal-free profiles of the Ca II H line with an exposure time of about 4.8 s. However, they may get lost at longer exposure times. The maximum spatial extension of these reversal-free profiles in our map was about 5 arcsec; they mostly appeared in smaller structures (Fig. 3.9, middle panel). The coherency of the position of the reversal-free profiles shows that they are not an artifact due to effects caused in the Earth atmosphere. The observed reversal-free Ca II H profiles (Fig. 3.10, lower panels) suggest that there may be some cool patches in the chromosphere for short periods of time. In contrast, Carlsson et al. (1997) tried to find reversal-free profiles in chromospheric spectral lines observed with SUMER (46.5–161 nm). On the basis of a few lines they concluded that "all chromospheric lines show emission above the continuum everywhere, all the time". These lines cover a large height range above the classical temperature minimum and should also reveal the cool patches seen in Ca II H line profiles if observed at the proper spatial and temporal resolution.

We propose that at a spatial resolution of one arcsecond, the average temperature

stratification in the solar atmosphere is probably hotter than the Holweger-Müller model atmosphere, but still does not show a permanent temperature rise at all spatial positions. Moreover, the residual core intensity of these profiles is about $0.05\,I_c$. The Holweger-Müller model, as well as comparable cool models (like model Q of Solanki et al. (1991) or model COOLC of Ayres et al. (1986)) and the cool phases of the dynamic models resulted in a very dark calcium core (Uitenbroek 2002), far below the observed reversal-free profiles. In these models, we have a longer cool phase and a shorter hot phase in the chromosphere (Rutten 1998; Judge & Peter 1998). Statistics of our inter-network sample indicated that some 75 % of all profiles showed one or more clear emission peaks. This appears to be in conflict with these models. But we recall that even if at any given point in the atmosphere the temperature is low most of the time, the Ca II H line may still show emission peaks most of the time because it is an integral property with contributions from a large height range. We speculate that this is even more important in 3D models, where lateral interaction with the ubiquitous shocks plays a role as well. Unfortunately, so far no one has attempted to compute Ca II H profiles simultaneously with the 3D MHD simulations. Even worse, computing Ca II H a posteriori for a single 3D snapshot already presents an unsolved task.

Our statistical studies of the inter-network calcium profiles show that about 25 % of the profiles do not show any emission peak (but might show a bulge). These reversal-free profiles (bottom panels, Fig. 3.10) are not reproduced by any of the hydrostatic model atmospheres with a chromospheric temperature rise, like in the new C6 model. This challenges Avrett & Loeser (2008), who claimed that they can reproduce all continuum and line intensities with models that have a temperature variation of at most 400 K. In addition, the observed reversal-free profiles cannot be derived from the dynamical models during the cool phase (Uitenbroek 2002, Fig. 6). Similarly, Avrett (1985) tried to modify the temperature stratification of VALA, VALC and VALF models to reproduce minimum and maximum profiles of Cram & Damé (1983). While we kept the temperature minimum constant and extended it isothermally, they introduced a hotter temperature minimum and decreased the temperature gradient (their Fig. 17). Our model ISO_30 and the corresponding profile (Fig. 3.14) better fits the observed reversal-free profile, which has lower intensity at the emission peak wavelengths than the minimum profile of Cram & Damé (1983).

Fontenla et al. (2007) presented a compromise solution for the cool patches. They proposed that cool patches may occur in a limited height range, such that they contribute substantially to the temperature sensitive molecules, but affect other spectral lines very little. This argument may apply to high-resolution filtergrams (Wöger et al. 2006). If we had cool temperatures in a very limited height range as proposed by Fontenla et al. (2007), and a hot atmosphere elsewhere, we would see emission features somewhere in each Ca II H spectrum, which is not the case. Therefore, although we have strong indications of cool patches in the solar chromosphere, they are more extended (in height) than was proposed by Fontenla et al. (2007).

Balasubramaniam (2001) presented multiple reversal calcium profiles and interpreted them as a signature of magnetic flux emergence. We observe some calcium profiles with

more than two emission peaks (Fig. 3.10, upper left panel) in the quiet Sun, without signature of magnetic flux emergence in the polarimetric channel of POLIS. Therefore, his explanation is not unique.

Conclusion: We find that a quarter of the observed calcium profiles in the quiet Sun inter-network show a reversal-free pattern. We interpret these profiles as strong indication for a temperature stratification cooler than that of the average quiet Sun. Although they do not imply a very cool atmosphere, like the one based on CO line observations (Ayres 2002) and numerical simulations (e.g., Carlsson et al. 1997; Rammacher & Cuntz 2005), it should be clearly cooler than that was suggested by Avrett & Loeser (2008). The reversal-free profiles we observed, at a spatial resolution of 1 arcsec and a temporal resolution of 5 s, show a residual intensity at the calcium core of about $0.05\,I_{\mathrm{c}}$. Hence, the profiles indicate that the cool components are cooler than the FALA, FALC, and C6 models in the sense that their corresponding profiles do not have any emission peak, but hotter than the extended Holweger-Müller model or the cool phase in the dynamic models.

Chapter 4

Conclusions

In recent years, our knowledge of the quiet Sun physics has changed drastically. The minimum phase of the solar cycle along with new space observatories and improved AO systems for ground-based telescopes provided a unique chance to clarify a variety of issues that were unknown for decades. For example, when Rouppe van der Voort et al. (2005) presented their G-band images with sub-arcsec spatial resolution, there was no clear answer for the following questions: Is there a sharp boundary around the magnetic elements as seen in the G-band images? Does the magnetic field change rather smoothly within the small-scale structures? Were the observed strange shapes of the magnetic elements just a result of integration along the LOS? These questions were addressed through recent high-resolution observations providing strong evidence for sub-structures and a sharp boundary in small-scale magnetic elements (e.g., Rezaei et al. 2007e). In addition, the existence of the magnetic field lines virtually everywhere on the solar surface observed with the Hinode SP (Lites et al. 2008) makes the quiet Sun not that '*quiet*'. Hence, new questions emerged with the new findings, to be answered in the future, e.g., what is the role of horizontal magnetic field in the heating of the upper atmosphere?

Our contributions to this revolutionary time are summarized in this chapter. First, our achievements on the photospheric magnetic fields are presented. Next, we discuss the connection between the chromospheric emission and the underlying photospheric magnetic field. Then, observational evidence for cool structures in the solar chromosphere is deduced. Finally, concluding remarks and an outlook for future work are presented.

4.1 Summary

Opposite-polarity profiles are two Stokes-V profiles in a single spectrum that show opposite magnetic polarities. We took a sequence of Stokes spectra of the Fe I 630 nm line pair in a region of quiet Sun near the disk center, using the POLIS spectropolarimeter at the German VTT in Tenerife. The line cores of these two lines form at different heights in the photosphere. We presented co-temporal and co-spatial Stokes-V profiles of the Fe I 630 nm line pair, where the two lines showed opposite polarities in a single spectrum. We computed synthetic line profiles and reproduced

these spectra with a two-component model atmosphere: a non-magnetic component and a magnetic component. The magnetic component consists of two magnetic layers with opposite polarity: the upper one moves upwards while the lower one moves downward. In-between, there is a region of enhanced temperature. The Stokes-V line pair of opposite polarity in a single spectrum can be understood as the result of a magnetic reconnection event in the solar photosphere (Sect. 2.2, see also Rezaei et al. 2007c).

The magnetopause is an electric current sheet at the interface layer between a magnetic element and its surroundings. Although there were observational indications for a sharp boundary in G-band images of magnetic elements, no direct polarimetric signature of a magnetopause had been found. We studied the structure of magnetic elements in network-cell interiors to find evidence for the existence of magnetopauses. A quiet Sun area close to the disk center was observed with the SP of the SOT on-board the Hinode space mission, with a spatial resolution of 0.3 arcsec in polarimetric data of the Fe I 630 nm line pair. For comparison and interpretation, we synthesized a similar data set from a 3D MHD simulation. We find several examples of magnetic elements, either roundish (tube) or elongated (sheet), that show a central area of negative Stokes-V area asymmetry surrounded by a peripheral area with larger positive asymmetry. This pattern was predicted some ten years ago on the basis of numerical simulations and interpreted as a signature of a magnetopause. Here, we observationally confirm its existence for the first time. We gathered convincing evidence that this pattern of Stokes-V area asymmetry is caused by the funnel-shaped boundary of magnetic elements that separates the flux concentration from the weak-field environment. This means that the magnetic field strength does not decrease gradually going away from the center of a magnetic element. Instead, there is a sharp boundary. On this basis, we conclude that electric current sheets induced by such magnetic boundary layers are common in the photosphere (Sect. 2.3, see also Rezaei et al. 2007d,e).

Temporal evolution of small-scale magnetic flux concentrations is due to the continuous interaction of magnetic elements and granulation. To study the structure and evolution of the magnetic elements, we observed a quiet region close to the disk center with POLIS at the German VTT. Stokes profiles of the Fe I 630 nm line pair, the Stokes-I profile of the Ca II H line at 396.8 nm, and a continuum speckle channel at 500 nm were recorded simultaneously. We presented two examples of magnetic flux cancellation of small-scale opposite-polarity patches, followed by an enhanced chromospheric emission. Speckle-reconstructed continuum images show that both sites were located in inter-granular vertices. In each case, the two opposite-polarity patches gradually became smaller and, within a few minutes, the smaller one completely disappeared. The larger patch also diminished significantly. While in one case there was a significant brightening in the chromospheric level, the second case showed just a weak enhancement. In the first case, the intensity enhancement at outer wing wavelengths of the Ca II H line profile was larger than in the inner wing,

and vice versa in the second case. The discrepancy between the two cases in their calcium wing intensity contrasts and calcium core emission is explained by a difference in the geometrical height at which the cancellation happened. Therefore, the second example provides evidence for a cancellation scenario *in the photosphere* that leaves minor traces at the chromospheric level (Sect. 2.4, see also Rezaei et al. 2007b).

Single-lobe Stokes-V profiles are the extreme case of asymmetric profiles. While most of the observed Stokes-V profiles in active regions and the network are nearly antisymmetric, strongly asymmetric and abnormal (i.e., profiles with more than two lobes) Stokes-V profiles are common in the inter-network. An extreme case of this asymmetry is when one lobe is absent, the single-lobe Stokes-V profiles. We observed several quiet Sun regions close to the center of the solar disk with the SP of the SOT on-board the Hinode space mission. Stokes profiles of the Fe I 630 nm line pair were recorded with a spatial resolution of 0.3 arcsec and a 3σ noise level of $3.4 \times 10^{-3}\, I_{\rm c}$. In this study, we analyzed 6.5 million Stokes-V profiles. Among them, two million profiles had an amplitude above the 3σ noise level. Some 18 % of all profiles show just a single lobe above the 3σ noise level. This is more than half of all profiles with an amplitude above the 3σ noise level. Among single lobe Stokes-V profiles, about 64 % have a blue lobe only and 36 % have only a red lobe. Separating blue-only from red-only profiles, we are able to discriminate between different formation scenarios presented by Steiner (2000). We find that blue-only profiles show brighter continuum and line-core intensity in the Fe I 630 nm line pair, unlike red-only profiles. Blue-only profiles also show a blue-shifted line core which is not the case for red-only profiles. In other words, blue-only profiles are observed inside granular upflows. These findings support the idea that an upflow in a non-magnetic layer along with a hot magnetic atmosphere can produce a blue-only profile (Sect. 2.5, see also Rezaei et al. 2008b).

The magnetic field strength in the solar inter-network was a matter of disagreement since various observational diagnostics presented different values for the typical magnetic field strength. In particular, the infrared neutral iron lines at 1.56μm yielded a magnetic field strength distribution that peaked at 200 G while the visible iron line pair at 630 nm indicated values about 1 kG. We simultaneously observed the Stokes parameters of the photospheric neutral iron line pair at 630 nm and the intensity profile of the chromospheric Ca II H line at 396.8 nm in a quiet Sun region at a heliocentric angle of 53°. The photospheric magnetic field vector has been reconstructed from an inversion of the measured Stokes profiles. In this process, a fixed initial model atmosphere was modified until the corresponding Stokes profiles matched the observed ones. In this initial model, the magnetic field strength was 900 G. However, the majority of the field strength values obtained from the inversion is below 600 G. The inter-network magnetic field is dominated by weak field strengths with values down to 200 G and has a mean absolute flux density of about $11\,{\rm Mx\,cm^{-2}}$ (Sect. 2.1, see also Rezaei et al. 2006b, 2007a).

The relation between photospheric magnetic field and chromospheric emission plays a key role in our understanding of the upper atmosphere. We investigated the relationship between the photospheric magnetic field and the emission of the mid chromosphere of the Sun. The same data set was used as mentioned in the previous paragraph. We performed a statistical analysis of network and inter-network properties. We separated a magnetically, H_{mag}, and a non-magnetically, H_{non}, heated component from a non-heated component, H_{re}, in the H-index. The average network and inter-network H-indices are equal to 12 and 10 pm, respectively. The emission in the network is correlated with the magnetic flux density, approaching a value of $H \approx 10$ pm for vanishing magnetic flux. We find that more than half of the chromospheric emission due to heating in the magnetic network has non-magnetic origin. Considering the effect of straylight, the contribution from an atmosphere with no temperature rise to the H-index ($H_{re} \approx 6$ pm) is about half of the observed H-index in the inter-network. The H-index in the inter-network is not correlated to any property of the photospheric magnetic field, suggesting that magnetic flux concentrations have a negligible role in the chromospheric heating in this region (Sect. 3.1, see also Rezaei et al. 2007a).

Reversal-free Ca II H profiles are profiles that do not show any emission peak at H_{2v} and H_{2r} wavelengths. We studied the chromospheric emission to verify the existence of such profiles and the corresponding temperature stratifications. Over 10^5 line profiles from inter-network regions were analyzed . We compared the observed profiles with synthesized spectra form a variety of model atmospheres with a NLTE radiative transfer code. A fraction of about 25 % of the observed Ca II H line profiles do not show a measurable emission peak in H_{2v} and H_{2r} wavelength bands. None of the chosen model atmospheres with a temperature rise can reproduce such profiles. On the other hand, the synthetic calcium profile of a model atmosphere that has a monotonic decline of the temperature with height shows a reversal-free profile that has much lower line core intensity than any observed line profile. The observed reversal-free profiles indicate the existence of cool patches in the interior of chromospheric network cells, at least for short time intervals. Our finding is in conflict not only with a full-time hot chromosphere, but also with a very cool chromosphere as found in some dynamic simulations (Sect. 3.2, see also Rezaei et al. 2008a).

4.2 Concluding remarks

Simultaneous measurements in the photosphere and chromosphere: The study of the Sun, our nearest star, is systematically moving from morphological observations (e.g., Ellerman bombs[1]) to a more physics-based modeling and theoretical understanding, in terms of nuclear physics, magneto-convection, magneto-hydrodynamics, magnetic reconnection, and particle physics processes. The major

[1]Ellerman bombs are short-lived, small-scale bright points observed best at the wing of chromospheric lines (Ellerman 1917; Socas-Navarro et al. 2006)

impact of physics-based modeling comes from the multi-wavelength observations from solar-dedicated space-based (e.g., Hinode) and ground-based (e.g., VTT) instruments.

Historically, after the invention of the magnetograph (Table 1.1), the measurements in the photosphere became more precise and superior to the chromosphere. Therefore, people started to find physical mechanisms to explain the time-dependent dynamic events in the photosphere (lower layer) and chromosphere (higher layer) instead of expanding the nomenclature. In all of such attempts, there are two important shortcomings: lack of the simultaneous magnetic field information and neglect of the differential refraction. Our effort to correlate a variety of parameters in the photosphere and chromosphere is one of the first attempts in which full Stokes measurements of the magnetic field are accompanied by spectral information in the Ca II H line profile. Although it sounds surprising, a plot like Fig. 3.7 has never been published before due to the lack of the required data. The work presented in Sect. 3.1 is just statistical correlations. The next step is to have time-series with a cadence of a few seconds, a factor of ten better than the cadence of the maps presented in Sect. 2.4. Although data sets like that presented in Sect. 2.4 are enough to trace exotic events, they are quite insufficient to elaborate on the dynamics of the chromosphere in the inter-network regions.

Thermal stratification: The temperature structure of the chromosphere is a controversial issue. The observed existence of the CO molecules (Sect. 3.1), for instance, indicates that cool patches must exist. Numerical simulations show areas as cool as 2000 K in the chromosphere. In contrast, the SUMER UV data showed that the emission lines are everywhere, so the temperature should increase outward. Our observations suggest that a quarter of all observed Ca II H line profiles are not in emission, in contrast to the UV spectral lines observed with SUMER. On the other hand, our NLTE radiative transfer modelling indicates that a monotonically decreasing temperature leads to a very dark core, which is in variant to all observational reports. As presented in Sect. 3.2, a constant temperature from the temperature minimum to the lower chromosphere is enough to diminish both emission peaks while we need a temperature rise to sustain the core intensity in the observed range.

Boundary layer of the magnetic elements: We discovered that smallest-scale magnetic structures obey the same principles as the largest ones: they show a sharp boundary containing a current sheet (Sect. 2.3). In other words, the magnetic field in a small-scale structure does not weaken radially: it is confined by a sharp boundary. While there were G-band images of such boundaries, we presented the first direct polarimetric signature of them. Asymmetric Stokes-V profiles including single-lobe profiles confirm also the canopy-like nature of funnel-shaped expansion of strong flux concentrations. Along with the finding of OP profiles, the large fraction of asymmetric profiles, both in Stokes-V and V/R ratio of the emission peaks of the Ca II H line, is a clear indication of strong gradients in the physical parameters in

the solar atmosphere.

Temporal evolution: Investigating the temporal evolution of small-scale magnetic structures is intrinsically a difficult task. One would like to gather data in two spatial dimensions, one spectral, one temporal, and an additional dimension for four Stokes parameters. However, in reality, we have only two dimensions and scan the others. So in any kind of such temporal data, there should be a compromise between cadence and integration time (signal-to-noise ratio). POLIS enabled us to record a two dimensional area ($8 \times 70\,\mathrm{arcsec}^2$) in two spectral bands and four Stokes parameters within a temporal cadence of 100 s. This unique data set was used in three sections (Sects. 2.2, 2.4, and 3.2): we found an OP profile and interpreted that as a signature of a photospheric reconnection, confirmed the existence of different reconnection scenarios in photosphere and chromosphere, and investigated the darkest Ca profiles to challenge the present static model atmospheres.

4.3 Outlook

Limitations of our diagnostics: Inconclusive ideas about the structure and evolution of the magnetic flux concentrations in the photosphere and the chromosphere have been presented in the past two decades. At the same time, a few standard techniques developed to handle photospheric magnetic fields, e.g., the profile inversion. Since the radiative transfer in the chromosphere is strongly influenced by NLTE effects, the present inversion codes which use LTE (Sect. 1.2.1) as a key simplification will break down in the chromosphere. The fact that our knowledge about the chromosphere is much less than that about the photosphere originates from the lack of computer resources to deal with the NLTE effects, both in 3D MHD simulations and in interpreting the observed data. Therefore, old questions like the heating mechanisms of the chromosphere have remained open for half a century.

How do the magnetic field fan out with height? A historic shortcoming in understanding both expansion of the magnetic field lines with height and propagating waves that (can) heat up the chromosphere is the lack of independent measurements of the magnetic field in the layers above the photosphere, i.e., in the temperature minimum and the chromosphere. Classically in an isothermal atmosphere, the density and pressure decrease with height exponentially. Therefore, the magnetic flux concentrations should expand to sustain the hydrostatic equilibrium. Hair-like structures observed in the CaII H filtergrams with the SOT on-board the Hinode near the solar limb challenged the classical explanation of the magnetic field expansion: the cross-sections of the hair-like structures do not significantly increase with height (Suematsu et al. 2007). This observation can be explained with the classical theories if the cross-section of the hair-like structures is far below the resolution limit of about 50 km.

Synthesis and inversion of Stokes spectra: Through various parts of this thesis, we used the SIR code to synthesize (Sect. 2.2 and 2.3) Stokes profiles from model atmospheres and invert (Sect. 2.1 and 3.1) observed Stokes profiles to retrieve the atmospheric parameters along the LOS. In case of synthetic profiles, spectral and spatial smearing were performed to make a consistent comparison between the observed profiles and synthesized ones. The inversion is a complementary method in addition to the profile analysis techniques. These methods especially helped us to interpret asymmetric Stokes profiles and connect them to gradients of magnetic and flow fields and thermodynamic parameters in the solar atmosphere, e.g., Sect. 2.3.

There are other LTE inversion techniques that can handle simultaneously a set of spectral lines. In contrast, NLTE inversion techniques are still under study. Yet worse is the fact that we cannot even synthesize simulation boxes with a NLTE code. Since we cannot invert the observed chromospheric lines to infer the model atmosphere, perform proper simulations of the chromosphere, or synthesize the existing 3D simulation boxes, our understanding of the solar chromosphere is less than that of the photosphere.

Computational power for realistic simulations: Most of the magneto-convection simulations of the solar surface use assumptions like LTE and grey opacity[2] and simplify the lateral radiative interactions. It is worth to note that still more than half of the whole simulation time is used to solve the transfer equation. One can imagine that incorporating a realistic radiative transfer in present codes will make them computationally prohibitive. This is one of the issues that simulations have always been criticized for. While the assumptions mentioned are justified in the photosphere, they are not fulfilled in the chromosphere.

Magnetic field measurement in the chromosphere: A measurement of the magnetic field in the chromosphere is not straightforward. The expansion of the magnetic field lines with height decreases the field strength by an order of magnitude in the chromospheric level comparing to the photospheric level. Therefore, weak polarization signals emerge from the chromospheric magnetic structures. In addition, the chromospheric spectral lines are usually too deep with a residual line core intensity of, e.g., 5 % of the nearby continuum intensity in the Ca II H line. Assuming a polarization degree of 1 % in the light beam, the fraction of polarized photons in the line core will be $5 \times 10^{-4}\, I_{\rm c}$. This is at the border of measurable signals with present solar telescopes assuming a long integration time. However, since the time-scale of the chromospheric evolution is a few seconds, we cannot have an integration time longer than that.

2D spectropolarimeters: Consider for instance a Fabry-Perot imaging spectrometer, an instrument that has two fixed spatial dimensions and scans through wavelength of a spectral line (e.g., Bellot Rubio et al. 2006). It takes about a quarter of a minute to

[2]The grey opacity is the opacity assuming that the extinction coefficient in the atmosphere to be independent of frequency (Rutten 2003).

scan a narrow iron line in the photosphere and measure only the intensity signal. For the same narrow line, measurements of the four Stokes parameters take about one minute. To decrease the scanning time, one can either record less spectral points (worse spectral resolution) or try shorter integration time (worse signal-to-noise ratio). The scanning time for a wide chromospheric line like Hα or Ca II H will be longer by a factor of two or more. The resulting cadence will be far longer than the time-scale of the chromospheric evolution (about 10 s). Therefore, a Fabry-Perot imaging spectropolarimeter is not a preferable instrument to measure chromospheric magnetic field with present solar telescopes.

The importance of differential refraction: The variation of the refractive index of the atmosphere with wavelength causes a tiny displacement of the solar images of two wavelengths (the differential refraction). A common feature of *all* slit spectrographs across the world is that the effect of the differential refraction was ignored in their designs. In practice, one puts the slit somewhere on the solar surface and records a set of spectral lines. These spectral lines can be selected such that they span a wide range in the solar atmosphere: from the lower photosphere to upper chromosphere. In this way, one hopes to trace different layers of the solar atmosphere simultaneously. The nightmare is that each line *sees* a different location on the Sun due to the wavelength dependent differential refraction. So a spectrum of one spatial position in two different wavelengths cannot be recorded with a *single* slit spectrograph. There are two possible ways to compensate for the differential refraction. The first method is constructing multi-slit spectrographs. In this way, the light passing through each slit has its own optical elements. One has to actively adjust the distance between the two slits depending on the amount of differential refraction perpendicular to the slit (Appendix B). The other method is to use optical elements in the light path as compensator. Such a compensator has to do exactly the opposite shift that happens in the earth atmosphere.

Final remark: In the last two decades, the computing facilities have been improving. Simultaneously, new solar telescopes have been constructed. The diameter of the largest solar telescope has not increased in the last half a century. However, there are two plans to build large solar telescopes with a diameter of 3-5 m. In addition, new instrumentation has been developed. In the last ten years, the best spatial resolution improved by a factor of ten. We hope that within a decade or so most of the problems mentioned in this section will be solved. This will provide new insights about the chromospheric physics and its connection to the photosphere.

Appendix A

The absorption line profile

The simplest picture one can construct of the process of emission in a line is to consider the atom to be a classical oscillator. A classical description of damped atomic oscillations was first presented by H. A. Lorentz. In this picture, an atom is assumed to be a harmonic oscillator in an external electromagnetic field (e.g., Symon 1971), a damped oscillator with eigen frequency of ω_0 and damping constant of γ. This system is excited by the external electric field:

$$m\,\ddot{x} + \gamma\,m\,\dot{x} + m\,\omega_0^2\,x = \mathrm{e}\,E_0\,e^{i\,\omega\,t}$$

The left hand side terms are inertia, damping, and restoring force and the right hand side is the excitation term. Assuming a solution of the form $x(t) = x_0 e^{i\,\omega\,t}$, we have

$$(-\omega^2 + i\,\omega\,\gamma + \omega_0^2)x = \frac{\mathrm{e}\,E_0}{m} e^{i\,\omega\,t}.$$

Therefore,

$$x(t) = \frac{\mathrm{e}\,E_0}{m} e^{i\,\omega\,t} \frac{\omega_0^2 - \omega^2 - i\,\omega\,\gamma}{(\omega_0^2 - \omega^2)^2 + \omega^2\,\gamma^2},$$

and the real part of that is:

$$\mathrm{Re}[x(t)] = \frac{\mathrm{e}\,E_0}{m} \left[\frac{\omega_0^2 - \omega^2}{(\omega_0^2 - \omega^2)^2 + \omega^2\,\gamma^2}\,\cos\omega t + \frac{\gamma\,\omega}{(\omega_0^2 - \omega^2)^2 + \omega^2\,\gamma^2}\,\sin\omega t \right].$$

Hence, the electrodynamic radiated power (Jackson 1999) is $p(t) = \frac{2}{3}\frac{\mathrm{e}^2}{c^3}(\ddot{x})^2$ where

$$\ddot{x}(t) = \frac{\mathrm{e}\,E_0}{m} \left[\frac{\omega_0^2 - \omega^2}{(\omega_0^2 - \omega^2)^2 + \omega^2\,\gamma^2}\,(-\omega^2)\,\cos\omega t + \frac{\gamma\,\omega}{(\omega_0^2 - \omega^2)^2 + \omega^2\,\gamma^2}\,(-\omega^2)\,\sin\omega t \right].$$

Average of the sine and cosine square over a period is

$$\overline{\cos^2\omega t} = \overline{\sin^2\omega t} = 1/2 \quad \& \quad \overline{\cos\omega t \sin\omega t} = 0.$$

Therefore, we have

$$\overline{(\ddot{x})^2} = \frac{1}{2}\left(\frac{\mathrm{e}\,E_0\,\omega^2}{m}\right)^2 \left[\frac{(\omega_0^2 - \omega^2)^2 + \gamma^2\,\omega^2}{\left((\omega_0^2 - \omega^2)^2 + \omega^2\,\gamma^2\right)^2}\right] = \frac{1}{2}\left(\frac{\mathrm{e}\,E_0}{m}\right)^2 \left[\frac{\omega^4}{(\omega_0^2 - \omega^2)^2 + \omega^2\,\gamma^2}\right].$$

So, the radiated power, averaged over one period is

$$\bar{p} = \frac{2}{3}\frac{\mathrm{e}^2}{c^3}\overline{(\ddot{x})^2} = \left(\frac{\mathrm{e}^4\,E_0^2}{3\,m^2\,c^3}\right)\left[\frac{\omega^4}{(\omega_0^2-\omega^2)^2+\omega^2\,\gamma^2}\right] = \frac{\mathrm{e}^4\,E_0^2}{3\,m^2\,c^3}\;\varphi(\nu)/C. \tag{A.1}$$

Here, $\varphi(\nu)$ is the profile function and C is the normalization constant,

$$\varphi(\nu) = \frac{\nu^4\,C}{(\nu_0^2-\nu^2)^2+\nu^2\,(\gamma/2\,\pi)^2}.$$

Since $\Delta\,\nu = \nu - \nu_0 \ll \nu, \nu_0$, one can write $(\nu_0^2-\nu^2)^2 \approx 4\,\nu_0^2\,(\nu_0-\nu)^2$ so,

$$\varphi(\nu) = \frac{\nu_0^2\,C}{4\,(\nu_0-\nu)^2+(\gamma/2\,\pi)^2} = \frac{C}{4}\frac{\nu_0^2}{(\nu_0-\nu)^2+(\gamma/4\,\pi)^2}.$$

Normalization:

$$\int_{\nu_0-\infty}^{\nu_0+\infty}\varphi(\nu)\mathrm{d}\nu = 1 \longrightarrow \int_{\nu_0-\infty}^{\nu_0+\infty}\varphi(\nu)\mathrm{d}\nu = \frac{C}{4}\nu_0^2\frac{4\,\pi}{\gamma}\int_{-\infty}^{+\infty}\frac{\mathrm{d}x}{1+x^2} = \frac{C\,\nu_0^2\pi^2}{\gamma},$$

so $C = \gamma/(\nu_0^2\,\pi^2)$. Therefore, the *Lorentz profile* is:

$$\varphi(\nu) = \frac{\gamma/4\,\pi^2}{(\nu_0-\nu)^2+(\gamma/4\,\pi)^2}. \tag{A.2}$$

The Lorentz profile is symmetric, i.e., $\varphi(-\Delta\nu) = \varphi(+\Delta\nu)$, and asymptotically reaches to $\varphi(\nu) \longrightarrow 1/(\Delta\nu)^2$. Its maximum height is $4/\gamma$ and has a full width at half maximum (FWHM) of,

$$\frac{2}{\gamma} = \frac{\gamma/4\,\pi^2}{(\Delta\nu)^2+(\gamma/4\,\pi)^2} \longrightarrow \Delta\nu_{\mathrm{FWHM}} = \frac{\gamma}{2\,\pi}.$$

A.1 The damping constant

The classical damping of oscillation (e.g., by friction, Symon 1971) is $F = \gamma\,m\,\dot{x}(t)$, so the damping power is *force* $\times$ *velocity*, i.e., $p(t) = \gamma\,m\,\dot{x}^2$. However, the damping power in electrodynamics (Jackson 1999) is obtained as $p(t) = \frac{2}{3}\,\frac{e^2}{c^3}\,\ddot{x}^2$. Note that the Ansatz of frictional force is not correct. One has to define damping constant, γ, such that the averaged power over one period is correct:

$$\gamma\,m\,\omega^2 = \frac{2}{3}\,\frac{e^2}{c^3}\,\omega^4 \longrightarrow \gamma = \frac{2}{3}\,\frac{e^2\,\omega_0^2}{m\,c^3}$$

assuming $\omega \approx \omega_0$.

So, we can calculate the FWHM of the transition,

$$\Delta\nu_{\mathrm{FWHM}} = \frac{\gamma}{2\,\pi} = \frac{4\,\pi\,e^2\,\nu_0^2}{3\,m\,c^3}$$

$$\frac{\Delta\nu_{\mathrm{FWHM}}}{\nu} = \frac{\Delta\lambda_{\mathrm{FWHM}}}{\lambda} \longrightarrow \Delta\lambda_{\mathrm{FWHM}} = \frac{c}{\nu^2}\Delta\nu_{\mathrm{FWHM}} = \frac{4\,\pi\,e^2}{3\,m\,c^2} = 1.18\times10^{-5}\,\mathrm{nm}.$$

Table A.1: The oscillator strength of some spectral lines (Allen 2000).

λ (nm)	line	$f_{\rm lu}$	$g_{\rm low}$	$g_{\rm up}$
121.57	Lyα	0.41	2	8
656.28	Hα	0.64	8	18
486.13	Hβ	0.12	8	32
434.05	Hγ	0.04	8	50

A.2 The absorption cross-section

The absorption coefficient, $\alpha(\nu)$, is defined as $\mathrm{d}I_\nu = -\alpha(\nu)\, I_\nu\, \mathrm{d}s$, where $\alpha(\nu) = \sigma(\nu)\, n_{\rm low}$, $n_{\rm low}$ is the number density of absorbers, and $\sigma(\nu)$ is the absorption cross-section. It is possible to separate the frequency dependence: $\sigma(\nu) = \sigma_0\, \varphi(\nu)$, where $\varphi(\nu)$ is measured per Hertz. We can calculate the absorption cross-section of a classical harmonic oscillator for plane electromagnetic waves. The power, averaged over one period, extracted from the radiation field (Eq. A.1) is:

$$\bar{p} = \frac{\mathrm{e}^4\, E_0^2}{3\, m^2\, c^3} \frac{\pi^2\, \nu_0^2}{\gamma}\, \varphi(\nu) \quad \text{with} \quad \gamma = \gamma_{\rm class} = \frac{2}{3} \frac{\mathrm{e}^2\, \omega_0^2}{m\, c^3}$$

$$\bar{p} = \frac{\mathrm{e}^4\, E_0^2}{3\, m^2\, c^3} \frac{\pi^2\, \nu_0^2\, 3\, m\, c^3}{8\, \mathrm{e}^2\, \pi^2\, \nu_0^2} \varphi(\nu) = \frac{\mathrm{e}^2\, E_0^2}{8\, m}\, \varphi(\nu).$$

On the other hand, $\bar{p} = \sigma(\nu) \int_{\nu'} \int_{\mu'} I(\nu',\, \mu') \mathrm{d}\nu'\, \mathrm{d}\mu' = \sigma(\nu)\, \frac{c}{8\,\pi} E_0^2$. Equating both sides, we have:

$$\sigma(\nu)\, \frac{c}{8\,\pi} E_0^2 = \frac{\mathrm{e}^2\, E_0^2}{8\, m} \varphi(\nu) \longrightarrow \sigma(\nu) = \sigma_0\, \varphi(\nu) \longrightarrow \sigma_0 = 2.654\, \times\, 10^{-6}\, \mathrm{m}^2\, \mathrm{H}z.$$

So classically, the line extinction is independent of the particular transition, while quantum mechanically, we need a correction factor. This correction factor is called *oscillator strength*, $f_{\rm lu}$. Hence, total line extinction coefficient per particle (frequency integrated), $\sigma_{\rm lu} = \int \sigma(\nu)\, \mathrm{d}\nu$, is given by

$$\sigma_{\rm lu} = \frac{\pi\, \mathrm{e}^2}{m\, c}\, f_{\rm lu}.$$

Following Eq. 1.5, the opacity equation reads

$$\alpha(\nu) = n_{\rm low}\, \frac{\pi\, \mathrm{e}^2}{m\, c}\, f_{\rm lu}\, \varphi(\nu). \tag{A.3}$$

In Eq. A.3, $n_{\rm low}$ is the population number of the lower level, $\frac{\pi\, e^2}{m\, c}$ is the classical cross-section where we have assumed that the radiated power is equal to damping, $f_{\rm lu}$ is the quantum mechanical correction factor, and $\varphi(\nu)$ is the profile function, i.e., the reaction of an oscillator (atom) to the external EM field. This equation relates the macroscopic quantity (absorption coefficient) to the microscopic atomic physics.

The oscillator strength, $f_{\rm lu}$ is obtained by, e.g., laboratory measurements, the solar spectrum, or quantum mechanical computations (e.g., opacity project). The oscillator strength of the allowed lines is about $f_{\rm lu} \approx 1$ while its value for the forbidden lines is $f_{\rm lu} \ll 1$. Table A.1 lists the oscillator strengths of a few spectral lines.

A.3 Radiation damping

Every energy level has a finite lifetime τ against radiative damping (except for the ground state), $\tau = 1/\sum_{l<u} A_{ul}$ where A_{ul} is the Einstein coefficient for spontaneous deexcitation which is the transition probability for spontaneous deexcitation from state u to state l per second per particle in state u (Rutten 2003). From the Heisenberg uncertainty principle, we know that the energy levels are not infinitely sharp. So, $\Delta E = \hbar/\Delta t$ or $\Delta \nu = \gamma/2\pi$ where $\gamma = 1/\Delta t$ is the radiative damping constant which gives the natural broadening. From quantum mechanics, we know that the profile is a Lorentz profile, $\gamma = 1/\tau_u + 1/\tau_l = \sum_{k<u} A_{uk} + \sum_{j<l} A_{lj}$. As an example, consider the resonance line (transition to ground state) of Lyα: $\gamma = A_{21} = 3\gamma_{\rm class}\,(g_1/g_2)\,f_{12} = 0.31\,\gamma_{\rm class}$. For the H$\alpha$ transition, $\gamma = 3\,\gamma_{\rm class}\left(\frac{g_1}{g_2}\,f_{12} + \frac{g_2}{g_3}\,f_{23} + \frac{g_1}{g_3}\,f_{13}\right) = 3\,\gamma_{\rm class}\left(\frac{2}{8}\,0.41 + \frac{8}{18}\,0.64 + \frac{2}{18}\,0.07\right) = 1.18\,\gamma_{\rm class}$.

A.4 Pressure broadening

Collisional broadening or pressure broadening results from other particles in the neighborhood. They may be electrons, ions, atoms or molecules. Their charge affects the radiating or extincting atom or ion of interest through the Coulomb interaction and therefore affects the frequency of a bound-bound transition between perturbed levels. These collisional encounters are often termed elastic although the energies are slightly changed momentarily; the term inelastic is reserved for collisions involving bound-bound transitions between different energy levels. Neutral atoms take part to some extent as perturber because they are polarizable, having a net electric field at close quarters. Of these, neutral H I atoms have the largest polarizability due to the bad shielding of the proton by the single electron. They are therefore important spectral line broadeners in cool atmospheres in which hydrogen is not ionized and which contain few free electrons (Gray 1992; Mihalas 1978).

Table A.2: Power index for the semi-classical theory of collisional broadening (Mihalas 1978; Rutten 2003).

p	name	dominant at
2	linear Stark effect	hydrogen-like ions
3	resonance broadening	neutral atoms with each other, H+H
4	quadratic Stark effect	ions
6	van der Waals broadening	metals, H

Pressure broadening is due to collision of radiating atoms with other particles, resulting in phase shift and disturbed oscillations. To find the intensity spectrum, consider the power spectrum of a cut wave train,

$$I_1(\omega) \sim \left| \int_{-t_0/2}^{t_0/2} e^{(\omega-\omega_0)t} \mathrm{d}t \right|^2 = \left[\frac{\sin(\frac{\omega-\omega_0}{2}t)}{\frac{\omega-\omega_0}{2}} \right]^2 .$$

Introducing the propability of collision in time t_0, $W(t_0)\mathrm{d}t_0 = \exp(-t_0/\tau)\mathrm{d}t_0/\tau$ where τ is the average time between two collisions, we have

$$I(\omega) = \int_0^\infty \left[\frac{\sin(\frac{\omega-\omega_0}{2}t)}{\frac{\omega-\omega_0}{2}} \right]^2 \exp(-t_0/\tau)\mathrm{d}t_0/\tau \longrightarrow \varphi(\omega) = \frac{1/\pi\,\tau}{(\omega-\omega_0)^2 + (1/\tau)^2}.$$

So the collisional broadening has a Lorentz profile with $\gamma = 2/\tau$ and $\tau \sim N^{-1}$ (see Mihalas 1978, for an extensive summary). To calculate τ precisely, one has to assume about the phase shift ($\Delta\omega$) which is given by semi-classical theory of Weisskopf-Lindhom (impact theory). It is possible to split various interactions by their schematic dependence on the separation r between the absorbing (photon-extinguishing) atom or ion and the perturber in the form $\Delta\omega = \Delta E/\hbar \equiv C_n\, r^{-n}$ where C_n is the interaction constant and r the distance at the moment of closest encounter (the impact parameter) for the impact approximation and the distance to the next ion in the quasi-static nearest-neighbor approximation. This scheme assumes that the interaction potentials may to first order be described as power laws in r, an approximation which holds to some extent but not perfectly. The power index n defines the name and type of the interaction species in Table A.2. The constant, C_n is calculated by laboratory measurements or calculations.

Appendix B

Differential refraction

The earth atmosphere acts like a prism that separates wavelengths, due to the wavelength dependence of the refractive index of air (Filippenko 1982; Reardon 2006; Beck et al. 2008). It leads to an angular displacement, which may amount up to several arcseconds between two wavelengths in the visible spectrum from 400 to 800 nm. The importance of the atmospheric dispersion increases rapidly with increasing zenith angle and decreasing wavelength.

The amount of the displacement is governed by the zenith distance of the Sun. The direction of the displacement is determined from the orientation of the detector relative to the celestial N–S direction and is perpendicular to the horizon. In other words, it is along the great circle connecting the solar center and zenith: the shorter wavelengths appear higher on the sky.

The refractive index of dry air as a function of λ at the see level (P=760 mmHg[1], $T = 15$°C) is given by (Eldén 1953):

$$n_0(\lambda) = 1. + 10^{-6} \,.\, (64.328 + \frac{29498.1}{146. - \lambda^{-2}} + \frac{255.4}{41. - \lambda^{-2}}). \tag{B.1}$$

This should be corrected for the lower pressure and temperature at the observatory site:

$$n_{cor}(\lambda, P, T) = 1. + [n_0(\lambda, P, T, H) - 1.]. \left(\frac{P[1. + (1.049 - 0.0157\,T)10^{-6}\,P]}{720.883(1. + 0.003661\,T)} \right) \tag{B.2}$$

Additionally, the presence of water vapor, denoted by the humidity H (in mmHg), leads to a decrease of the refractive index (Barrell 1951):

$$n(\lambda, P, T, H) = n_{cor} - 10^{-6} \,.\, \frac{0.0624 - 0.00068\,\lambda^{-2}}{1. + 0.003661\,T}\,H \tag{B.3}$$

The following equation presents the total displacement in arcseconds for the given wavelengths and zenith angles (Smart 1977):

$$\Delta\, R\,(\lambda_1, \lambda_2) = 206265 \times tan(z)\,[n(\lambda_1) - n(\lambda_2)] \tag{B.4}$$

For the VTT, one may assume P=600 mmHg, H=0 mmHg, and $T = 15$°C.

[1] 1 mmHg = 1 Torr = 1.333 mbar = 133.3 Pa

Projection of the dispersion axis into the focal plane: The parallactic angle, β, the angle between the dispersion axis and the celestial N-S axis is given by (Beck et al. 2008):

$$\beta = \arctan\left(\frac{\sin t_{\odot}}{\cos \delta_{\odot}. \tan \phi - \sin \delta_{\odot}. \cos t_{\odot}}\right) \tag{B.5}$$

β incorporates the time-dependent part of the direction of the spatial displacement, which is due to the daily solar revolution on the sky.

Image rotation due to the telescope: A coelostat telescope system (Mills 1985) may introduce an additional image rotation in the focal plane. A displacement of the first mirror by an angle γ from the terrestrial N-S axis leads to a constant image rotation p, given by:

$$p = \text{-} \arcsin\left(\frac{\cos \phi \sin \delta}{\cos \delta_0}\right) + \gamma \tag{B.6}$$

where ϕ is the geographical latitude of the observatory site.

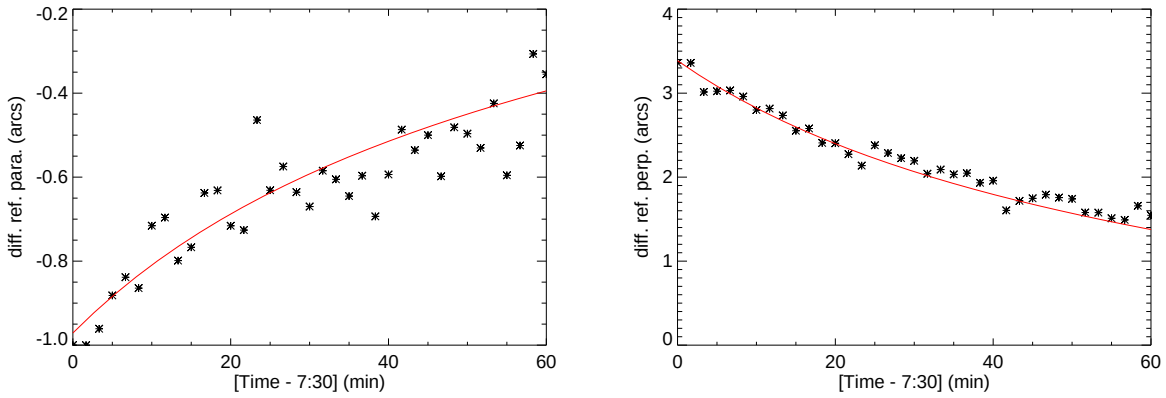

Figure B.1: The two component of the differential refraction, corresponding to the plot of Fig. 2.18. The curves represent the theoretical calculations and asterisks show data points.

Instrument orientation in the focal plane: For a slit-spectrograph, the slit orientation relative to the celestial N-S, α, has to be considered. For a coelostat system, the angles α and p are constant during the day and depend only on the instrument geometry. The angle Ψ between the slit and the dispersion axis is then given by adding all contributions:

$$\Psi = \beta + (p + \alpha)$$

where the parenthesis denotes the contribution due to the telescope and instruments. The dispersion perpendicular, $\triangle R_{\perp}$, and parallel to the slit, $\triangle R_{\parallel}$, are then given by (Beck et al. 2008):

$$\begin{pmatrix} \triangle R_{\perp} \\ \triangle R_{\parallel} \end{pmatrix} = \begin{pmatrix} \sin\Psi \\ \cos\Psi \end{pmatrix} . \triangle R(\lambda_1, \lambda_2) \tag{B.7}$$

The orientation of the fixed POLIS slit ($\alpha \approx 52 \pm 1°$) is seen to be unfortunate: during the main observing times, the displacement is mainly perpendicular to the slit, leading to a time-gap between the co-spatial data of the two POLIS channels. While the displacement perpendicular to the slit between the visible and IR is about 2 arcsec early morning in August, it can be more than 3 arcsec between the red and blue channels. Figure B.1 shows the two components of the differential refraction.

Appendix C

Calibration of POLIS Ca channel

POLIS was designed to facilitate co-temporal and co-spatial measurements of the vector magnetic field in the photosphere and the Ca II H intensity profile (Schmidt et al. 2003; Beck et al. 2005b). We tried to elaborate on the uncertainties in the intensity calibration, because it was critical for the estimates of the various contributions (straylight, non-magnetic heating, etc.) to the observed calcium profiles. Observations are discussed in Sect. C.1. The linearity of the CCD camera for different light levels is explained in Sect. C.2. Then, we investigate instrumental and solar stray light contributions in Sect. C.3. In Sect. C.4, we persent standard error propagation to quantify the noise level and uncertainties in our final calibrated spectra.

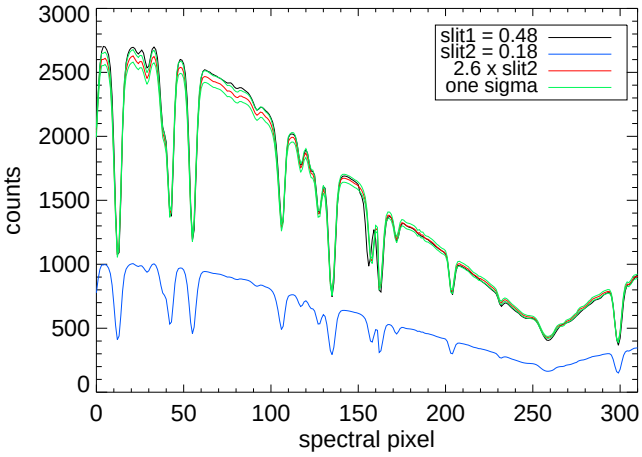

Figure C.1: Comparison between two different slit widths and the same modulation speed. The black and blue profiles correspond to slit widths of 0.48 and 0.18 arcsec, respectively. The red profile is the blue profile multiplied by a constant factor of 2.6. The green profiles show the $\pm 1\sigma$ rms value ($\sim 1\%$) from the mean curve (red). Note that the two profiles were selected from two averaged flat fields, providing two frames with similar illuminations.

C.1 Observations

In order to study linearity of the POLIS calcium Charged Coupled Device (CCD) camera at different light levels, we observed a set of calcium spectra and flat field data with different accumulations and slit widths at disk center. A sunspot was also observed with

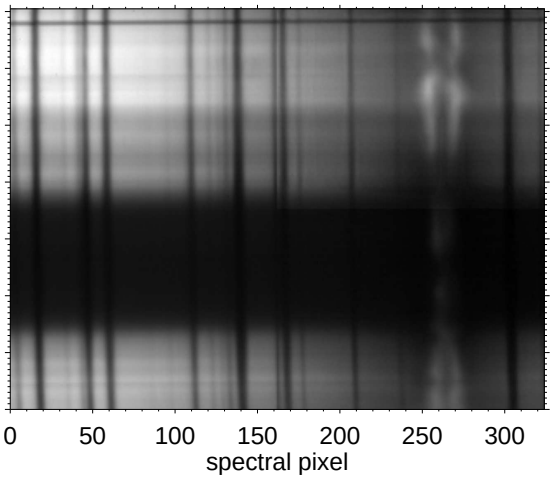

Figure C.2: Dark subtracted spectrum of a big sunspot. The slit passed through the umbra.

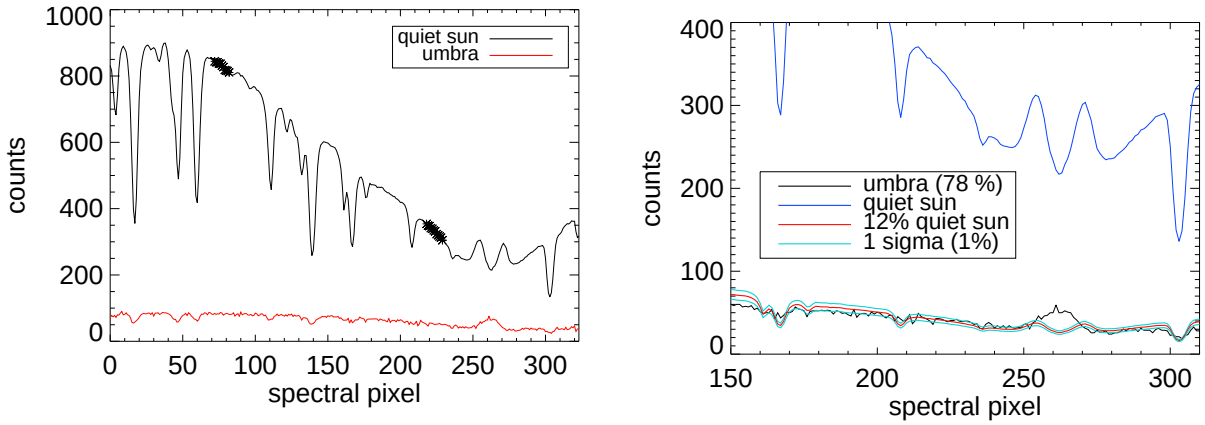

Figure C.3: *Left:* a single Ca II H line profile of the umbra of a sunspot (red) and the quiet Sun (black). Asterisks show spectral bands that were used to estimate the true signal (see Sect. C.3). *Right:* close up view of the quiet Sun and umbral profiles near the calcium line core. The true signal (about 5 % in the wing close to the Ca core according to Wallace et al. 2000) was subtracted from the umbral profile. The red curve shows 12 % of the quiet sun profile. The two cyan curves show an uncertainty interval of one sigma (1 %).

a similar setup and an exposure time of 0.82 s and six accumulations. Besides this, we recorded dark current data using either the adaptive optics or POLIS field stop. We used these two data sets to estimate the solar and instrumental straylight, respectively.

All spectra and profiles used in this Appendix were dark subtracted raw data. No other calibration process like flat fielding was applied. In order to show intrinsic noise in the data, we did not spatially average darks or spectra.

C.2 Linearity

To check the linearity of the calcium camera from profiles by, e.g., comparing the ratio of the core to wing for different exposures, we recorded spectra with different slit width and similar modulation speed (Mullikin et al. 1994). Figure C.1 shows a comparison between two flat field profiles taken on disk center with identical illumination, but different slit widths. The black and blue profiles correspond to a slit width of 0.48 and 0.18 arcsec, respectively. If one multiplies the blue curve with the ratio of the slit widths of 2.67, the resulting curve agrees well with the profile of the broad slit for all wavelengths including the line core. We calculated the ratio of the two profiles with different slit widths as function of wavelength. The rms variation of the ratio was 1%. This can be used as an upper limit for non-linearity effects of the CCD camera.

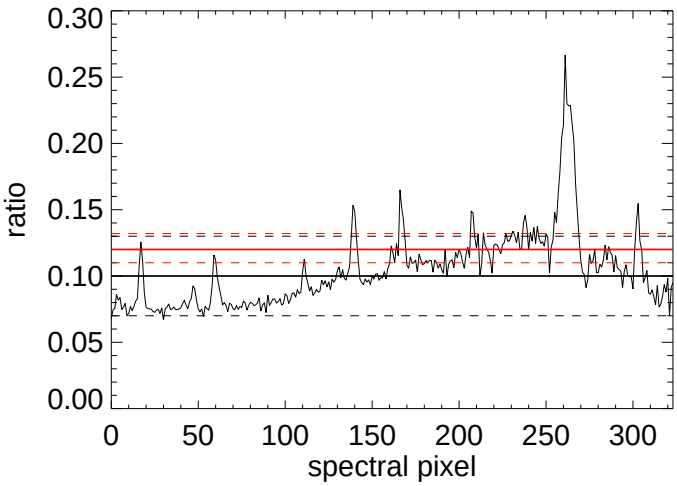

Figure C.4: Ratio of the umbral profile to a quiet Sun profile. If one considers all the spectrum, the ratio will be $10 \pm 3\,\%$ while considering only parts of the wing close to the Ca II H core, the ratio will be $12 \pm 1\,\%$. Note the mismatch between the quiet Sun and umbral profiles at spectral line positions due to different broadenings.

C.3 Stray light

False light: We compared two sets of dark current images of the POLIS red channel: one with a field stop right after the focal plane, and another one with the field stop in front of the camera. In the second case, all light sources inside the observing room were fully blocked. The difference between the two measurements was about $0.9 \pm 0.5\,\%$. This gave an upper limit for the instrumental straylight in the POLIS Ca channel as well, since most of the sources in the observing room would not emit in blue as efficient as red.

Atmospheric and telescopic stray light: The calcium profile in the sunspot umbra is significantly weaker than a normal profile (in continuum bands). However, there is a well known single emission peak in the calcium core (Linsky & Avrett 1970). We thus compared an inner wing band close to the calcium core, but excluding the core itself (asterisks in the left panel of Fig. C.3), in an umbral profile and a normal profile from

outside the spot to derive an upper limit for the solar stray light contribution to observed profiles.

Figure C.2 shows a slit spectrum of the umbra. To keep the sample profiles as uniform as possible, we chose two identical positions along the slit (at about 30 arcsec, Fig. C.2). The spectrum of the quiet Sun and the minimum spectrum of the umbra are shown in Fig. C.3 (left panel).

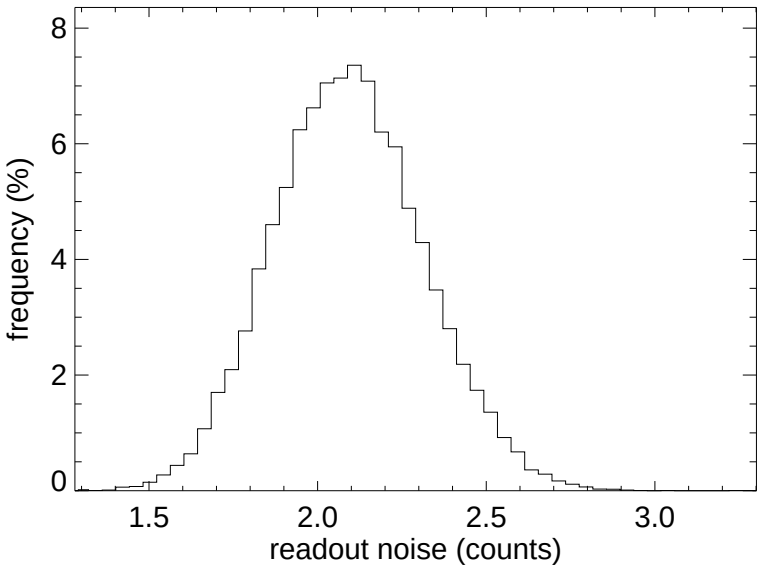

Figure C.5: Distribution of the readout error in a set of 50 dark currents with 8 accumulations.

Wallace et al. (2000) presented a Fourier transform spectral atlas of the umbra. In this atlas, the wing close to the umbral core has an intensity of 5 % in units of the umbral continuum, while the wing close to the Fe I, Ti I, and Ni I lines at about 396.5 nm has an intensity of 38 %. In our umbral profile, this continuum had an intensity of about 80 counts (asterisks, Fig. C.3, left panel), whereas close to the core the profile had about 45 counts. Assuming no stray light in the atlas profile, only 11 counts (~ 22 % of the observed valued) should be measured in the core. Thus, 78% of the observed signal have to be due to straylight. To reproduce 78% of the umbral profile, a straylight contribution of around 10-12 % is needed. Note that if we assume that there is no real calcium signal in the umbra (which is wrong) and take the observed calcium profile of the umbra as pure scattered light, the ratio changes from 12 % to 15 %. Therefore, uncertainties about the scattered light in the atlas profile have minor importance.

A close up view of the spectral region close to the calcium core was shown in Fig. C.3 (right panel). For the reason mentioned above, in the right panel of Fig. C.3, the umbral profile was labeled *umbra (78 %)*. The red curve shows 12 % of the quiet Sun profile. The two cyan curves also show an uncertainty interval of one sigma (1 %). Figure C.4 shows the ratio of the umbra to the quiet Sun profile. The mean and rms of the whole spectrum are 10 ± 3 % while considering only on the wing band close to the calcium core, it was 12 ± 1 %. This value is in agreement with an independent estimate for the amount of

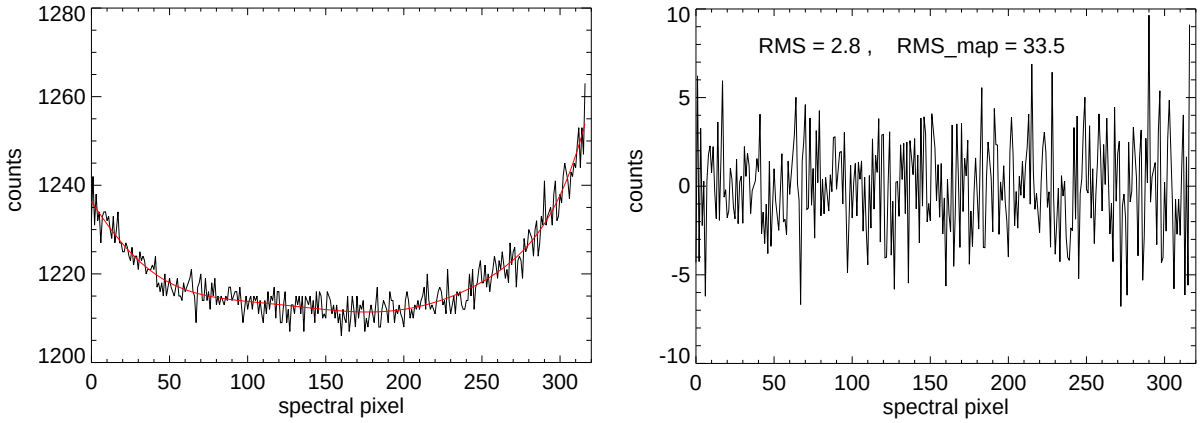

Figure C.6: *L*eft panel: a row in a dark frame with 6 accumulation. The curve is a polynomial fit to subtract systematic shift from the random noise. *R*ight panel: The residual signal after subtraction of the polynomial, which is the real noise. Note to the large difference between the rms of the map (excluding its borders) and the rms of the residuals.

stray light in POLIS which is 15 % (Cabrera Solana et al. 2007). We took this value as an upper limit for the total stray light in the POLIS calcium channel. In Sect. C.3, we found that the instrumental stray light is about 1 %. Hence, most of the obtained stray light originates from the scattered solar light in the telescope and the earth atmosphere.

C.4 Noise

There are three noise sources in a CCD camera (Mullikin et al. 1994):

1. readout noise because of the pre-amplifier,
2. dark current noise which is influenced by the chip temperature, and
3. photon noise due to the quantum nature of light which obeys Poisson statistics.

The readout error of the camera was estimated by a set of 50 consecutive dark frames with similar exposure and accumulations. Here, we compared the number of counts on each pixel in different images. We attribute the standard deviation of the count value mainly to the readout error, and hence, obtain a readout error for each pixel separately. The distribution of the readout errors was shown in Fig. C.5. The readout noise is about $\sigma_{\text{readout}} \sim 2$ counts.

To investigate the thermal noise in the dark current, one has to remove small systematic offsets between CCD columns (probably due to thermal fluctuations of the Analogue to Digital (AD) system) before considering statistical measures, e.g., rms, of a dark profile (a CCD row). As it is shown in Fig. C.6, for a dark frame with six accumulations, the resulting rms (after removing systematics) is far less than the standard deviation of the

whole map including a large scale variation. It provided an estimate for the thermal noise in the camera. So the rms of the dark frame was about $\sigma_{\text{thermal}} \sim 3$ counts.

The total noise in the recorded data, σ_{noise}, consisted of three components:

$$\sigma_{\text{noise}} = \sqrt{\sigma^2_{\text{photon}} + \sigma^2_{\text{thermal}} + \sigma^2_{\text{readout}}} \tag{C.1}$$

where the photon noise originates from the Poisson fluctuations of the number of photons counted. Assuming that n_{photon} is the number of detected photons, the corresponding rms is $\sigma^2_{\text{photon}} = \text{n}_{\text{photon}}$. The calcium core is more influenced by the noise than the other points in the spectrum. Figure C.7 shows a dark subtracted calcium spectrum with six accumulations and a narrow slit (0.18 arcsec). The minimum number of counts in the core was 117, so $\sigma_{\text{photon}} \sim 11$. Therefore, the total noise in the core (Eq. C.1) would be $\sigma_{\text{noise}} \sim 11$. So the worst signal-to-noise ratio at the calcium core position was better than 10. Note that the data described in Chapter 3 were obtained with a wide slit (0.48 arcsec) while the spectrum shown in Fig. C.7 was recorded with a narrow slit (0.18 arcsec), so we had better signal-to-noise ratio in the data.

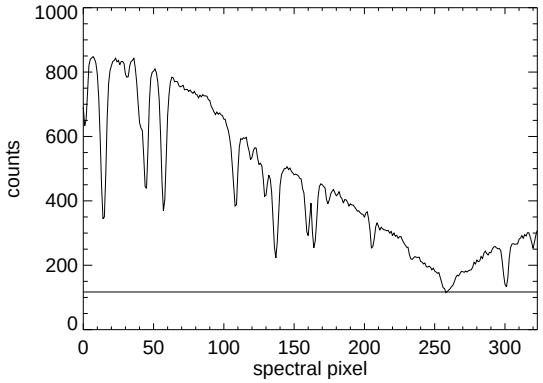

Figure C.7: A sample calcium profile. We use the calcium core minimum counts to estimate the photon noise. In this case, the signal-to-noise ratio at the calcium core is more than 10.

Error propagation: The relative intensity of the core to wing is defined as, $x = \text{I}_{\text{core}}/\text{I}_{\text{wing}}$. To estimate the rms errors, we find the signal-to-noise ratio for the core and wing intensities in some wing bands. Since it is not possible to use the core intensity to obtain the noise due to intrinsic changes, we use the average signal-to-noise ratio of the left and right wings close to the calcium core as the signal-to-noise of the core. So the real signal-to-noise of the core is probably worse than that. The signal-to-noise ratio of the core and wing varies from 35 and 112 for two accumulations to 174 and 216 for twenty accumulations. We use the worse signal-to-noise ratio corresponding to an exposure time of 1.64 s and obtain the following values for the rms errors of the core and wing intensities:

$$\frac{\sigma_c}{\text{I}_{\text{core}}} \sim \frac{1}{34} \sim 3\,\% \tag{C.2}$$

$$\frac{\sigma_w}{\text{I}_{\text{wing}}} \sim \frac{1}{112} \sim 1\,\% \tag{C.3}$$

So, we can obtain the σ_x as follows:

$$\frac{\sigma_x}{\mathrm{x}} = \sqrt{(\frac{\sigma_c}{\mathrm{I_{core}}})^2 + (\frac{\sigma_w}{\mathrm{I_{wing}}})^2} \sim 3\,\%. \tag{C.4}$$

Error sources of the final calibrated data included uncertainties from the flat-field parameter, the straylight and the linearity of the detector. The straylight uncertainty was obtained about 1 % in Sect. C.3. Assuming an upper limit for the uncertainty in the flat-field to be 5 % and some 1 % uncertainty in linearity of the core to wing ratio, *an upper limit* for the uncertainty in the calibrated spectrum will be:

$$\frac{\sigma_r}{r} < 10\,\%.$$

Basic physical properties of the Sun

(Allen 2000)

Physical parameter	Numerical value
radius	$R_\odot = 6.96 \times 10^8$ [m]
mass	$M_\odot = 1.99 \times 10^{30}$ [kg]
average density	$\rho_\odot = 1400$ [kg m^{-3}]
gravity at solar surface	$g_\odot = 274$ [m s^{-2}]
solar luminosity	$L_\odot = 3.8 \times 10^{26}$ [Watt]
chemical composition	70 % H, 28 % He
central temperature	$T_{\rm core} = 20.0 \times 10^6$ [K]
surface temperature	$T_\odot = 5800$ [K]
escape velocity at solar surface	$v = 618$ [km s^{-1}]
synodic rotation period in equator	$P = 27.3$ [day]
siderial rotation period in equator	$P = 25.4$ [day] (equator)
	$P = 35.0$ [day] (at altitude $\pm 70°$)
solar age	$t_\odot = 4.57 \times 10^9$ [years]
mean distance from Earth	1 AU = 149 597 870 [km]
energy flux on the Earth	1.37 [kW m^{-2}]
apparent size	32', 01"
color-index	0.6
absolute magnitude	-26.7
apparent magnitude	4.5

Abbreviations

AC	Azimuth Center
AD	Analogue to Digital
BP	Bright Point
CCD	Charged Coupled Device
DOT	Dutch Open Telescope
EIT	Extreme ultraviolet Imaging Telescope
EUV	Extreme UltraViolet
FWHM	Full Width at Half Maximum
HSRA	Harvard Smithsonian Reference Atmosphere
ITP	International Time Program
KAOS	Kiepenheuer Adaptive Optics System
KE	Kinetic Equilibrium
KIS	Kiepenheuer-Institut für Sonnenphysik
LOS	Line-Of-Sight or Line Of Sight
LTE	Local Thermodynamic Equilibrium
MHD	MagnetoHydroDymanics
NLTE	Non Local Thermodynamic Equilibrium
OP	Opposite Polarity
POLIS	POlarimetric LIttrow Spectrograph
PSF	Point Spread Function
RF	Responce Function
RMS	Root Mean Square
RTE	Radiative Transfer Equation
SIR	Stokes Inversion based on Response functions
SOHO	SOlar and Heliospheric Observatory
SOT	Solar Optical Telescope
SP	Spectro-Polarimeter
SST	Swedish Solar Telescope
SUMER	Solar Ultraviolet Measurements of Emitted Radiation
SVD	Singular Value Decomposition
THEMIS	Tlescope Héliographique pour lÉtude du Magnétisme et des Instabilités Solaires
UV	Ultra Violet
VTT	Vacuum Tower Telescope
ZC	Zero Crossing

Bibliography

Allen, C. W. 2000, "Astrophysical Quantities", ed. Arthur Cox (Springer-Verlag: New York, 4rd edition)

Anderson, L. S. & Athay, R. G. 1989, ApJ, 346, 1010

Aschwanden, M. J. 2004, Physics of the Solar Corona. An Introduction (Praxis)

Auer, L. H. & Heasley, J. N. 1978, A&A, 64, 67

Avrett, E. H. 1985, in Chromospheric Diagnostics and Modelling, NSO/SP Summer Conf., Sunspot, ed. B. W. Lites, 67–127

Avrett, E. H. 2007, in Astronomical Society of the Pacific Conference Series, Vol. 368, The Physics of Chromospheric Plasmas, ed. P. Heinzel, I. Dorotovič, & R. J. Rutten, 81

Avrett, E. H. & Loeser, R. 2008, ApJS, 175, 229

Ayres, T. R. 2002, ApJ, 575, 1104

Ayres, T. R., Testerman, L., & Brault, J. W. 1986, ApJ, 304, 542

Babcock, H. 1953, ApJ, 118, 387

Balasubramaniam, K. S. 2001, ApJ, 557, 366

Barrell, H. 1951, Journal of the Optical Society of America, 41, 295

Beck, C., Bellot Rubio, L. R., & Nagata, S. 2005a, in Chromospheric and Coronal Magnetic Fields, ESA Special Publication, ed. A. L. D. E. Innes & S. A. Solanki, 596

Beck, C., Bellot Rubio, L. R., Schlichenmaier, R., & Sütterlin, P. 2007, A&A, 472, 607

Beck, C., Schlichenmaier, R., Collados, M., Bellot Rubio, L., & Kentischer, T. 2005b, A&A, 443, 1047

Beck, C., Schmidt, W., Bellot Rubio, L. R., et al. 2006, in Astronomical Society of the Pacific Conference Series, Vol. 358, Astronomical Society of the Pacific Conference Series, ed. R. Casini & B. W. Lites, 72

Beck, C., Schmidt, W., Kentischer, T., & Elmore, D. 2005c, A&A, 437, 1159

Beck, C., Schmidt, W., Rezaei, R., & Rammacher, W. 2008, A&A, 479, 213

Beckers, J. M. 1969, Sol. Phys., 10, 262

Bellot Rubio, L. R. 2003, Inversion of Stokes profiles with SIR, (Freiburg: Kiepenheuer Institut für Sonnenphysik)

Bellot Rubio, L. R. & Beck, C. 2005, ApJ, 626, L125

Bellot Rubio, L. R. & Collados, M. 2003, A&A, 406, 357

Bellot Rubio, L. R., Rodríguez Hidalgo, I., Collados, M., Khomenko, E., & Ruiz Cobo, B. 2001, ApJ, 560, 1010

Bellot Rubio, L. R., Ruiz Cobo, B., & Collados, M. 1997, ApJ, 478, L45

Bellot Rubio, L. R., Ruiz Cobo, B., & Collados, M. 2000, ApJ, 535, 489

Bellot Rubio, L. R., Tritschler, A., Kentischer, T., Beck, C., & Del Toro Iniesta, J. C. 2006, Solar Active Regions and 3D Magnetic Structure, 26th meeting of the IAU, Joint Discussion 3, 16-17 August, 2006, Prague, Czech Republic, JD03, #58, 3

Berger, T. E., Rouppe van der Voort, L. H. M., Löfdahl, M. G., et al. 2004, A&A, 428, 613

Berger, T. E. & Title, A. M. 2001, ApJ, 553, 449

Bianda, M., Stenflo, J. O., & Solanki, S. K. 1999, A&A, 350, 1060

Biermann, L. 1948, Zeitschrift fur Astrophysik, 25, 161

Blanco Rodríguez, J., Okunev, O. V., Puschmann, K. G., Kneer, F., & Sánchez-Andrade Nuño, B. 2007, A&A, 474, 251

Böhm-Vitense, E. 1989, "Introduction to Stellar Astrophyics.III Stellar Structure nad Evolution" (Cmbdidge Univ Press, Cambdrige UK)

Bruls, J. H. M. J. & Solanki, S. K. 1993, A&A, 273, 293

Cabrera Solana, D., Bellot Rubio, L. R., Beck, C., & Del Toro Iniesta, J. C. 2007, A&A, 475, 1067

Cabrera Solana, D., Bellot Rubio, L. R., & del Toro Iniesta, J. C. 2005, A&A, 439, 687

Carlsson, M., Hansteen, V. H., de Pontieu, B., et al. 2007, PASJ, 59, 663

Carlsson, M., Judge, P. G., & Wilhelm, K. 1997, ApJ, 486, L63

Carlsson, M. & Stein, R. F. 1994, in Chromospheric Dynamics, ed. M. Carlsson, 47

Carlsson, M. & Stein, R. F. 1997, ApJ, 481, 500

Cattaneo, F., Brummell, N. H., & Cline, K. S. 2006, MNRAS, 365, 727

Cattaneo, F., Emonet, T., & Weiss, N. 2003, ApJ, 588, 1183

Chandrasekhar, S. 1947, ApJ, 105, 424

Chandrasekhar, S. 1950, Radiative Transfer (Clarendon Press, Oxford)

Collados, M. 2001, in ASP Conf. Ser. 236: Advanced Solar Polarimetry – Theory, Observation, and Instrumentation, ed. M. Sigwarth, 255

Collados, M., Martinez Pillet, V., Ruiz Cobo, B., del Toro Iniesta, J. C., & Vazquez, M. 1994, A&A, 291, 622

Condon, E. & Shortley, G. 1964, "The Theory of Atmoic Spectra" (Cambridge University Press)

Cram, L. E. & Damé, L. 1983, ApJ, 272, 355

De Moortel, I., Ireland, J., Hood, A. W., & Walsh, R. W. 2002, A&A, 387, L13

De Pontieu, B., Carlsson, M., Stein, R., et al. 2006, ApJ, 646, 1405

De Pontieu, B., McIntosh, S. W., Carlsson, M., et al. 2007, Science, 318, 1574

de Wijn, A. G., Rutten, R. J., Haverkamp, E. M. W. P., & Sütterlin, P. 2005, A&A, 441, 1183

del Toro Iniesta, J. C. 2003, Introduction to Spectropolarimetry (Cambridge, UK: Cambridge University Press, 2003)

Domínguez Cerdeña, I., Almeida, J. S., & Kneer, F. 2006, ApJ, 646, 1421

Domke, H. 1971, Astrofizika, 7, 39

Drake, S. 1978, Galileo at work: his scientific biography, Chicago: The University of Chicago Press

Eldén, B. 1953, J. Opt. Soc. Am., 43, 399

Ellerman, F. 1917, ApJ, 46, 298

Faurobert, M., Arnaud, J., Vigneau, J., & Frisch, H. 2001, A&A, 378, 627

Fawzy, D., Rammacher, W., Ulmschneider, P., Musielak, Z. E., & Stępień, K. 2002a, A&A, 386,

971
Fawzy, D., Ulmschneider, P., Stępień, K., Musielak, Z. E., & Rammacher, W. 2002b, A&A, 386, 983
Filippenko, A. V. 1982, PASP, 94, 715
Fleck, B., Domingo, V., & Poland, A. I. 1995, Sol. Phys., 162
Fligge, M. & Solanki, S. K. 2001, Astronomical and Astrophysical Transactions, 20, 467
Fontenla, J., White, O. R., Fox, P. A., Avrett, E. H., & Kurucz, R. L. 1999, ApJ, 518, 480
Fontenla, J. M., Avrett, E., Thuillier, G., & Harder, J. 2006, ApJ, 639, 441
Fontenla, J. M., Avrett, E. H., & Loeser, R. 1993, ApJ, 406, 319
Fontenla, J. M., Balasubramaniam, K. S., & Harder, J. 2007, in Astronomical Society of the Pacific Conference Series, Vol. 368, The Physics of Chromospheric Plasma, ed. P. Heinzel, I. Dorotovič, & R. J. Rutten, 499
Fossum, A. & Carlsson, M. 2005, Nature, 435, 919
Foukal, P. 1990, Solar astrophysics (New York, Wiley-Interscience, 492 p.)
Gingerich, O. 1993, The Eye of Heaven, New York: American Institute of Physics
Gingerich, O., Noyes, R. W., Kalkofen, W., & Cuny, Y. 1971, Sol. Phys., 18, 347
Giovanelli, R. G. 1946, Nature, 158, 81
Gray, D. F. 1992, The Observation and Analysis of Stellar Photospheres (Cambridge University Press.)
Grossman-Doerth, U., Kneer, F., & von Uexküll, M. 1974, Sol. Phys., 37, 85
Grossmann-Doerth, U., Keller, C. U., & Schuessler, M. 1996a, A&A, 315, 610
Grossmann-Doerth, U., Keller, C. U., & Schüssler, M. 1996b, A&A, 315, 610
Grossmann-Doerth, U., Schuessler, M., & Steiner, O. 1998, A&A, 337, 928
Grossmann-Doerth, U., Schüssler, M., Sigwarth, M., & Steiner, O. 2000, A&A, 357, 351
Grossmann-Doerth, U., Schüssler, M., & Solanki, S. K. 1988, A&A, 206, L37
Grossmann-Doerth, U., Schüssler, M., & Solanki, S. K. 1989, A&A, 221, 338
Guillermier, P. & Koutchmy, S. 1999, Total Eclipses, Sciences, Observations, Myths & Legends (Springer-Praxis series in Astronomy, Springer-Verlag)
Hagenaar, H. J. 2001, ApJ, 555, 448
Hale, G. 1908, ApJ, 28, 315
Hale, G. & Ellerman, F. 1903, ApJ, 19, 41
Hammer, R. 1987, LNP Vol. 292: Solar and Stellar Physics, 292, 77
Hammer, R., Musielak, Z. E., & Routh, S. 2007, Astr. Nach., 328, 704
Hammer, R. & Ulmschneider, P. 2007, in American Institute of Physics Conference Series, Vol. 919, Kodaikanal Winter School on Solar Physics, AIPC Series, ed. S. S. Hasan & D. Banerjee, 138–172
Hansteen, V. H., De Pontieu, B., Rouppe van der Voort, L., van Noort, M., & Carlsson, M. 2006, ApJ, 647, L73
Harvey, J. W. 1973, Sol. Phys., 28, 9
Harvey, K. L. & White, O. R. 1999, ApJ, 515, 812
Heasley, J. N. 1975, Sol. Phys., 44, 275
Hirschfeld, A. 2001, Parallax, Freeman
Hirzberger, J. & Wiehr, E. 2005, A&A, 438, 1059

Holweger, H. & Müller, E. A. 1974, Sol. Phys., 39, 19
Ichimoto, K., Lites, B., Elmore, D., et al. 2008, Sol. Phys., 249, 233
Illing, R. M. E., Landman, D. A., & Mickey, D. L. 1975, A&A, 41, 183
Jackson, J. D. 1999, Classical electrodynamics (New York: Wiley, 3rd ed.)
Jefferies, S. M., McIntosh, S. W., Armstrong, J. D., et al. 2006, ApJ, 648, L151
Jing, J., Chae, J., & Wang, H. 2008, ApJ, 672, L73
Judge, P. G. & Peter, H. 1998, Space Sci. Rev., 85, 187
Kalkofen, W., Ulmschneider, P., & Avrett, E. H. 1999, ApJ, 521, L141
Keller, C. U., Deubner, F.-L., Egger, U., Fleck, B., & Povel, H. P. 1994, A&A, 286, 626
Keller, C. U., Schüssler, M., Vögler, A., & Zakharov, V. 2004, ApJ, 607, L59
Keppens, R. & Martinez Pillet, V. 1996, A&A, 316, 229
Khomenko, E. & Collados, M. 2007, ApJ, 659, 1726
Khomenko, E. V., Collados, M., Solanki, S. K., Lagg, A., & Trujillo Bueno, J. 2003, A&A, 408, 1115
Khomenko, E. V., Martínez González, M. J., Collados, M., et al. 2005a, A&A, 436, L27
Khomenko, E. V., Shelyag, S., Solanki, S. K., & Vögler, A. 2005b, A&A, 442, 1059
Kiepenheuer, K. 1953, ApJ, 117, 447
Kittel, C. 1980, Thermal Physics (Freeman, San Francisco)
Kosugi, T., Matsuzaki, K., Sakao, T., et al. 2007, Sol. Phys., 243, 3
Kronig, R. d. L. 1925, Z. Physik., 31, 885
Kubat, J. & Karlicky, M. 1986, Bulletin of the Astronomical Institutes of Czechoslovakia, 37, 155
Kurucz, R. L., Furenlid, I., Brault, J., & Testerman, L. 1984, Solar flux atlas from 296 to 1300 nm (National Solar Observatory Atlas, Sunspot, New Mexico)
Lamb, H. 1908, in Series A, Vol. 72, Proceedings of the Royal Society of London., 122–141
Lamb, H. 1911, in Series A, Vol. 84, Proceedings of the Royal Society of London., 551–572
Landi degl'Innocenti, E. 1999, in Canary Icelands Summer School: Astrophysical Polarization, ed. S. L. Keil & S. V. Avakyan, 1–53
Landi Deglinnocenti, E. & Landi Deglinnocenti, M. 1981, Nuovo Cimento B Serie, 62, 1
Landi degl'Innocenti, E. & Landolfi, M. 1983, Sol. Phys., 87, 221
Landi degl'Innocenti, E. & Landolfi, M. 2004, Polarization in Spectral Lines (Astrophysics and Space Science Library, Kluwer Academic Publishers)
Landolfi, M. & Landi degl'Innocenti, E. 1996, Sol. Phys., 164, 191
Langangen, Ø., Carlsson, M., Rouppe van der Voort, L., & Stein, R. F. 2007, ApJ, 655, 615
Leka, K. D. & Steiner, O. 2001, ApJ, 552, 354
Li, H., Sakurai, T., Ichimito, K., et al. 2007, PASJ, 59, 643
Linsky, J. L. & Avrett, E. H. 1970, PASP, 82, 169
Lites, B., Casini, R., Garcia, J., & Socas-Navarro, H. 2007a, Memorie della Societa Astronomica Italiana, 78, 148
Lites, B., Socas-Navarro, H., Kubo, M., et al. 2007b, PASJ, 59, 571
Lites, B. W. 2002, ApJ, 573, 431
Lites, B. W., Kubo, M., Socas-Navarro, H., et al. 2008, ApJ, 672, 1237
Lites, B. W., Rutten, R. J., & Berger, T. E. 1999, ApJ, 517, 1013

Lites, B. W., Rutten, R. J., & Kalkofen, W. 1993, ApJ, 414, 345
Lites, B. W., Scharmer, G. B., Berger, T. E., & Title, A. M. 2004, Sol. Phys., 221, 65
Lites, B. W., Skumanich, A., & Martinez Pillet, V. 1998, A&A, 333, 1053
Litvinenko, Y. E. 1999, ApJ, 515, 435
López Ariste, A., Martínez González, M. J., & Ramírez Vélez, J. C. 2007, A&A, 464, 351
Martínez González, M. J., Collados, M., & Ruiz Cobo, B. 2006, A&A, 456, 1159
Martínez Pillet, V., Lites, B. W., & Skumanich, A. 1997, ApJ, 474, 810
Martinez Pillet, V., Lites, B. W., & Skumanich, A. 1997, ApJ, 474, 810
Meadows, A. 1970, Early Solar Physics, Pergamon Press
Mihalas, D. 1978, Stellar Atmospheres (San Francisco, W. H. Freeman and Co.)
Mikurda, K. & von der Lühe, O. 2006, Sol. Phys., 235, 31
Mills, A. A. 1985, Journal of the British Astronomical Association, 95, 89
Mullikin, J. C., van Vliet, L. J., Netten, H., et al. 1994, in Proc. SPIE Vol. 2173, Image Acquisition and Scientific Imaging Systems, ed. H. C. Titus & A. Waks, 73–84
Nagata, S., Tsuneta, S., Suematsu, Y., et al. 2008, ApJ, 677, L145
Narain, U. & Ulmschneider, P. 1996, Space Science Reviews, 75, 453
Neckel, H. 1999, Sol. Phys., 184, 421
Oranje, B. J. 1983, A&A, 124, 43
Orozco Suárez, D., Bellot Rubio, L. R., & del Toro Iniesta, J. C. 2007, ApJ, 662, L31
Orozco Suárez, D., Bellot Rubio, L. R., del Toro Iniesta, J. C., & Tsuneta, S. 2008, A&A, 481, L33
Ossendrijver, M. 2003, A&ARev, 11, 287
Paletou, F., López Ariste, A., Bommier, V., & Semel, M. 2001, A&A, 375, L39
Parker, E. N. 1958, ApJ, 128, 669
Parker, E. N. 1979, Cosmical Magnetic Fields: Their Origin and Thier Activity (Oxford University Press, NewYork)
Parker, E. N. 1994, Spontaneous current sheets in magnetic fields : with applications to stellar x-rays (New York : Oxford University Press,)
Pierce, A. K. & Slaughter, C. D. 1977, Sol. Phys., 51, 25
Press, W. H., Flannery, B. P., & Teukolsky, S. A. 1986, Numerical recipes. The art of scientific computing (Cambridge: University Press, 1986)
Priest, E. & Forbes, T. 2000, Magnetic Reconnection (Cambridge University Press)
Priest, E. R., Heyvaerts, J. F., & Title, A. M. 2002, ApJ, 576, 533
Rachkovsky, D. N. 1962, Izv. Krymsk. Astrofiz. Obs., 28, 259
Rammacher, W. 2005, in ESA Special Publication, Vol. 596, Chromospheric and Coronal Magnetic Fields, ed. D. E. Innes, A. Lagg, & S. K. Solanki, 60
Rammacher, W. & Cuntz, M. 2005, A&A, 438, 721
Reardon, K. P. 2006, Sol. Phys., 239, 503
Reif, F. 1965, Fundamentals of Satistical and Thermal Physics (McGraw-Hill Book Company)
Rezaei, R., Bruls, J. H. M. J., Schmidt, W., et al. 2008a, A&A, 484, 503
Rezaei, R., Schlichenmaier, R., Beck, C., & Bellot Rubio, L. R. 2006a, A&A, 454, 975
Rezaei, R., Schlichenmaier, R., Beck, C. A. R., Bruls, J. H. M. J., & Schmidt, W. 2007a, A&A, 466, 1131

Rezaei, R., Schlichenmaier, R., Beck, C. A. R., & Schmidt, W. 2006b, in Modern Solar Facilities - Advanced Solar Science, Proceedings of a Workshop held at Göttingen September 27-29, ed. F. Kneer, K. G. Puschmann, & A. D. Wittmann, 169–173

Rezaei, R., Schlichenmaier, R., & Schmidt. 2008b, in Sun and Heliosphere, DPG 2008, Freiburg, 16

Rezaei, R., Schlichenmaier, R., Schmidt, W., & Beck, C. 2007b, in Solar Polarization Workshop, Sep 17-21, Locarno, Ascona, ASPC series, ed. S. Berdyugina, N. Nagendra, & R. Ramelli, in press.

Rezaei, R., Schlichenmaier, R., Schmidt, W., & Steiner, O. 2007c, A&A, 469, L9

Rezaei, R., Steiner, O., Wedemeyer-Böhm, S., Schlichenmaier, R., & Lites, B. W. 2007d, Astr. Nach., 328, 706

Rezaei, R., Steiner, O., Wedemeyer-Böhm, S., et al. 2007e, A&A, 476, L33

Rouppe van der Voort, L. H. M., Hansteen, V. H., Carlsson, M., et al. 2005, A&A, 435, 327

Ruiz Cobo, B. & del Toro Iniesta, J. C. 1992, ApJ, 398, 375

Ruiz Cobo, B. & del Toro Iniesta, J. C. 1994, A&A, 283, 129

Rutten, R. J. 1998, in Solar Composition and Its Evolution – From Core to Corona, ed. C. Fröhlich, M. C. E. Huber, S. K. Solanki, & R. von Steiger, 269

Rutten, R. J. 1999, in ASP Conf. Ser. 184: Third Advances in Solar Physics Euroconference: Magnetic Fields and Oscillations, ed. B. Schmieder, A. Hofmann, & J. Staude, 181–200

Rutten, R. J. 2003, Radiative Transfer in Stellar Atmosphere (Sterrekundig Instutuut Utrecht, Institute of Theoretical Astrophysics, Oslo)

Rutten, R. J. & Uitenbroek, H. 1991, Sol. Phys., 134, 15

Saar, S. H. 1996, in IAU Symp. 176: Stellar Surface Structure, ed. K. G. Strassmeier & J. L. Linsky, 237

Sakurai, J. J. 1985, Modern Quantum Mechanics (Addison-Wesley)

Sánchez Almeida, J., Collados, M., & del Toro Iniesta, J. C. 1989, A&A, 222, 311

Sánchez Almeida, J., Domínguez Cerdeña, I., & Kneer, F. 2003a, ApJ, 597, L177

Sánchez Almeida, J., Emonet, T., & Cattaneo, F. 2003b, ApJ, 585, 536

Schaffenberger, W., Wedemeyer-Böhm, S., Steiner, O., & Freytag, B. 2005, in ESA Special Publication, Vol. 596, ESA Special Publication, ed. D. E. Innes, A. Lagg, & S. A. Solanki

Schaffenberger, W., Wedemeyer-Böhm, S., Steiner, O., & Freytag, B. 2006, in Astronomical Society of the Pacific Conference Series, Vol. 354, Solar MHD Theory and Observations: A High Spatial Resolution Perspective, ed. J. Leibacher, R. F. Stein, & H. Uitenbroek, 345

Schatzman, E. L., Praderie, F., & King, A. R. 1993, The Stars (Springer-Verlag Berlin Heidelberg)

Schmidt, W., Beck, C., Kentischer, T., Elmore, D., & Lites, B. 2003, Astr. Nach., 324, 300

Schrijver, C. 1995, A&A Rev., 6, 181

Schrijver, C. J. 1987, A&A, 172, 111

Schrijver, C. J., Cote, J., Zwaan, C., & Saar, S. H. 1989, ApJ, 337, 964

Schrijver, C. J., Shine, R. A., Hagenaar, H. J., et al. 1996, ApJ, 468, 921

Schrijver, C. J., Title, A. M., van Ballegooijen, A. A., Hagenaar, H. J., & Shine, R. A. 1997, ApJ, 487, 424

Schrijver, C. J. & Zwaan, C. 2000, Solar and Stellar Magnetic Activity (Cambridge University Press)

Schrijver, C. J., T. A. M. v. A. A. H. H. J. & Shine, R. A. 1997, ApJ, 487, 424
Schüssler, M. 1990, in IAU Symposium, Vol. 138, Solar Photosphere: Structure, Convection, and Magnetic Fields, ed. J. O. Stenflo, 161–179
Schüssler, M., Shelyag, S., Berdyugina, S., Vögler, A., & Solanki, S. K. 2003, ApJ, 597, L173
Scott, P. C., Asplund, M., Grevesse, N., & Sauval, A. J. 2006, A&A, 456, 675
Seares, F. H. 1913, ApJ, 38, 99
Shelyag, S., Schüssler, M., Solanki, S. K., & Voegler, A. 2007, A&A, 467
Shimizu, T., Nagata, S., Tsuneta, S., et al. 2007, Sol. Phys., 154
Shine, R. A. & Linsky, J. L. 1974, Sol. Phys., 39, 49
Shu, F. H. 1981, "The Physical Universe: An Introduction to Astronomy" (University Science Books, California)
Shu, F. H. 1991, "The Physics of Astrophysics (I)" (University Science Books, California)
Sigwarth, M. 2000, Reviews of Modern Astronomy, 13, 45
Sigwarth, M. 2001, ApJ, 563, 1031
Sigwarth, M., Balasubramaniam, K. S., Knölker, M., & Schmidt, W. 1999a, A&A, 349, 941
Sigwarth, M., Balasubramaniam, K. S., Knölker, M., & Schmidt, W. 1999b, A&A, 349, 941
Skumanich, A., Smythe, C., & Frazier, E. N. 1975, ApJ, 200, 747
Smart, W. M. 1977, Textbook on spherical astronomy (Cambridge: University Press, 6th ed., edited by Green, R.M.)
Socas-Navarro, H., Martínez Pillet, V., Elmore, D., et al. 2006, Sol. Phys., 235, 75
Solanki, S. K. 1989, A&A, 224, 225
Solanki, S. K. 1993, Space Science Reviews, 63, 1
Solanki, S. K. 1999, in ASP Conf. Ser. 158: Solar and Stellar Activity: Similarities and Differences, 109
Solanki, S. K., Inhester, B., & Schüssler, M. 2006, Reports of Progress in Physics, 69, 563
Solanki, S. K. & Pahlke, K. D. 1988, A&A, 201, 143
Solanki, S. K. & Steiner, O. 1990, A&A, 234, 519
Solanki, S. K., Steiner, O., & Uitenbroek, H. 1991, A&A, 250, 220
Solanki, S. K. & Stenflo, J. O. 1984, A&A, 140, 185
Solanki, S. K., Zufferey, D., Lin, H., Rueedi, I., & Kuhn, J. R. 1996, A&A, 310, L33
Spruit, H. C. 1976, Sol. Phys., 50, 269
Spruit, H. C. 1979, Sol. Phys., 61, 363
Steiner, O. 1999, in ASP Conf. Ser. 184: Third Advances in Solar Physics Euroconference: Magnetic Fields and Oscillations, ed. B. Schmieder, A. Hofmann, & J. Staude, 38–54
Steiner, O. 2000, Sol. Phys., 196, 245
Steiner, O. 2003a, A&A, 406, 1083
Steiner, O. 2003b, in NATO Advanced Research Workshop: Turbulence, waves, and instabilities in the solar plasma, ed. R. Erdelyi & K. Petrovay, 181–200
Steiner, O. 2005a, A&A, 430, 691
Steiner, O. 2005b, in ESA SP-600: The Dynamic Sun: Challenges for Theory and Observations
Steiner, O. 2007, in American Institute of Physics Conference Series, Vol. 919, Kodaikanal Winter School on Solar Physics, AIPC Series, ed. S. S. Hasan & D. Banerjee, 74–121
Steiner, O., Grossmann-Doerth, U., Knoelker, M., & Schuessler, M. 1998, ApJ, 495, 468

Steiner, O., Hauschildt, P. H., & Bruls, J. 2001, A&A, 372, L13

Steiner, O., Hauschildt, P. H., & Bruls, J. 2003, Astr. Nach., 324, 398

Steiner, O., Rezaei, R., Schaffenberger, W., & Wedemeyer-Böhm, S. 2008, ApJ, 680, L85

Stenflo, J. O. 1994, Solar Magnetic Fields: Polarized Radiation Diagnostics (Astrophysics and Space Science Library, Kluwer Academic Publishers)

Stenflo, J. O., Solanki, S., Harvey, J. W., & Brault, J. W. 1984, A&A, 131, 333

Stix, M. 2004, The Sun : An Introduction (2nd ed., Astronomy and Astrophysics library: Springer)

Sturrock, P. A. 1966, Nature, 211, 695

Suematsu, Y. 1990, in LNP Vol. 367: Progress of Seismology of the Sun and Stars, ed. Y. Osaki & H. Shibahashi, 211

Suematsu, Y., Katsukawa, Y., Ichimoto, K., et al. 2007, in American Astronomical Society Meeting Abstracts, Vol. 210, American Astronomical Society Meeting Abstracts, 94.11

Suematsu, Y., Tsuneta, S., Ichimoto, K., et al. 2007, Sol. Phys., submitted

Symon, K. R. 1971, "Mechanics" (Addison-Wesley, Massachusetts, 3rd edition)

Takeuchi, A. & Shibata, K. 2001, ApJ, 546, L73

Tarbell, T. D. 2006, in AAS/Solar Physics Division Meeting, Vol. 37, 36

Tritschler, A., Schmidt, W., Uitenbroek, H., & Wedemeyer-Böhm, S. 2007, A&A, 462, 303

Trujillo Bueno, J., Shchukina, N., & Asensio Ramos, A. 2004, Nature, 430, 326

Tsuneta, S., Ichimoto, K., Katsukawa, Y., et al. 2008, Sol. Phys., 249, 167

Uitenbroek, H. 1989, A&A, 213, 360

Uitenbroek, H. 2001, ApJ, 557, 389

Uitenbroek, H. 2002, ApJ, 565, 1312

Ulmschneider, P. & Musielak, Z. 2003, in Astronomical Society of the Pacific Conference Series, Vol. 286, Current Theoretical Models and Future High Resolution Solar Observations: Preparing for ATST, ed. A. A. Pevtsov & H. Uitenbroek, 363–376

Unno, W. 1956, Publ. Astron. Soc. Japan, 8, 108

Vaughan, A. H., Preston, G. W., & Wilson, O. 1978, PASP, 90, 267

Vernazza, J. E., Avrett, E. H., & Loeser, R. 1981, ApJS, 45, 635

Voigt, W. 1913, Physikal. Z., 14, 377

von der Lühe, O., Soltau, D., Berkefeld, T., & Schelenz, T. 2003, in Innovative Telescopes and Instrumentation for Solar Astrophysics. Proceedings of the SPIE, Volume 4853, ed. S. L. Keil & S. V. Avakyan, 187–193

Wallace, L., Hinkle, K., & Livingston, W. 2000, An atlas of sunspot umbral spectra in the visible, from 15,000 to 25,500 cm(-1) (3920 to 6664 [Å]) (National Optical Astronomy Observatories)

Weber, E. J. & Davis, L. 1967, ApJ, 148, 217

Wedemeyer-Böhm, S. 2008, A&A, 487, 399

Wedemeyer-Böhm, S., Freytag, B., Steffen, M., Ludwig, H.-G., & Holweger, H. 2004, A&A, 414, 1121

Wedemeyer-Böhm, S., Kamp, I., Bruls, J., & Freytag, B. 2005, A&A, 438, 1043

Wedemeyer-Böhm, S., Steiner, O., Bruls, J., & Rammacher, W. 2007, in Astronomical Society of the Pacific Conference Series, Vol. 368, The Physics of Chromospheric Plasmas, ed. P. Heinzel, I. Dorotovič, & R. J. Rutten, 93

Weiss, N. O. 1966, Proc. R. Soc. Lond. **A**., 293, 310
Westendorp Plaza, C., del Toro Iniesta, J. C., Ruiz Cobo, B., et al. 1998, ApJ, 494, 453
Wilson, C. 1989, The Newtonian achievement in Astronomy, in The General History of Astronomy, vol. 2A, eds. R.Taton and C. Wilson, Cambridge University Press, pps. 234-274
Withbroe, G. L. & Noyes, R. W. 1977, ARA&A, 15, 363
Wittman, A. 1974, Sol. Phys., 35, 11
Wöger, F. 2006, PhD thesis, Freiburg University
Wöger, F., Wedemeyer-Böhm, S., Schmidt, W., & von der Lühe, O. 2006, A&A, 459, L9
Young, C. 1897, The Sun (revised ed.), Appleton and Co., chap. 8
Zeeman, P. 1897, Phil. Mag., 43, 226
Zirin, H. 1988, Astrophysics of the Sun (Cambridge University Press)
Zirker, J. 1995, Total Eclipses of the Sun (Princeton University Press)
Zwaan, C. 1987, ARA&A, 25, 83

Index